

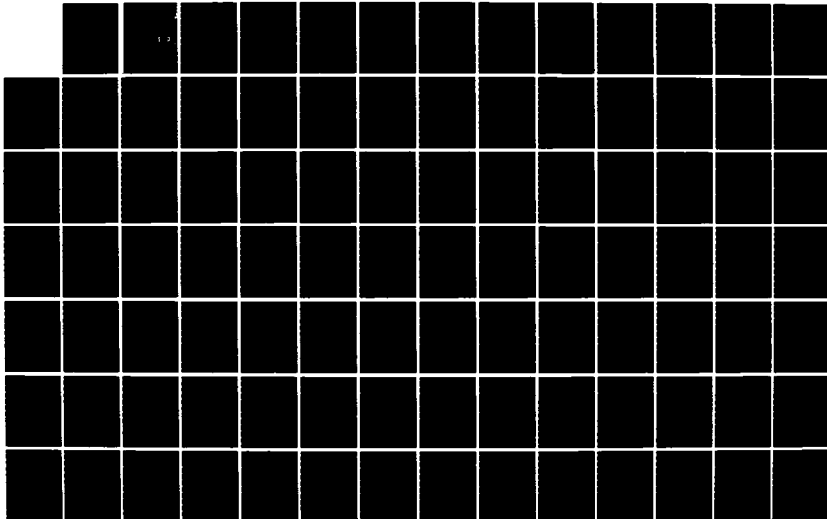
AD-A163 268

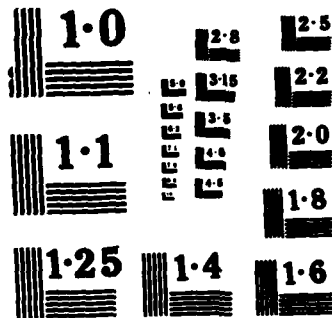
DAMAGE PREDICTION OF PROJECTILE PENETRATION PROCESS  
BASED ON ENERGY DISSIP. (U) LEHIGH UNIV BETHLEHEM PA  
INST OF FRACTURE AND SOLID MECHANICS. G C SIM ET AL.  
AUG 85 AMMRC-TR-85-26 DAAG46-83-K-0158 F/G 19/4

1/2

UNCLASSIFIED

NL





NATIONAL BUREAU OF STANDARDS  
MICROCOPY RESOLUTION TEST CHART

AD-A163 268



AD



AMMRC TR 85-26

DAMAGE PREDICTION OF PROJECTILE PENETRATION PROCESS  
BASED ON ENERGY DISSIPATION RATE

August 1985

G. C. SIH and D. H. SONG  
Institute of Fracture and Solid Mechanics  
Lehigh University  
Bethlehem, Pennsylvania 18015

DTIC  
ELECTE  
JAN 23 1986  
S D  
D

FINAL REPORT

Contract No. DAAG46-83-K-0158

Approved for public release; distribution unlimited.

DTIC FILE COPY

Prepared for

ARMY MATERIALS AND MECHANICS RESEARCH CENTER  
Watertown, Massachusetts 02172-0001

86 1 22 087

UNCLASSIFIED

SECURITY CLASSIFICATION OF THIS PAGE (When Data Entered)

REPORT DOCUMENTATION PAGE		READ INSTRUCTIONS BEFORE COMPLETING FORM
1. REPORT NUMBER ANMRC TR 85-26	2. GOVT ACCESSION NO. AD A163	3. RECIPIENT'S CATALOG NUMBER 268
4. TITLE (and Subtitle) DAMAGE PREDICTION OF PROJECTILE PENETRATION PROCESS BASED ON ENERGY DISSIPATION RATE	5. TYPE OF REPORT & PERIOD COVERED Final Report - 1 April 1983 to 30 September 1984	
	6. PERFORMING ORG. REPORT NUMBER	
7. AUTHOR(s) G. C. Sih and D. H. Song	8. CONTRACT OR GRANT NUMBER(s) DAAG46-83-K-0158	
9. PERFORMING ORGANIZATION NAME AND ADDRESS Institute of Fracture and Solid Mechanics Lehigh University Bethlehem, Pennsylvania 18015	10. PROGRAM ELEMENT, PROJECT, TASK AREA & WORK UNIT NUMBERS D/A Project: 8X363304D215 AMCMS Code: 693000.2156	
11. CONTROLLING OFFICE NAME AND ADDRESS Army Materials and Mechanics Research Center ATTN: ANMRC-K Watertown, Massachusetts 02172-0001	12. REPORT DATE August 1985	
	13. NUMBER OF PAGES 153	
14. MONITORING AGENCY NAME & ADDRESS (if different from Controlling Office)	15. SECURITY CLASS. (of this report)  Unclassified	
	15a. DECLASSIFICATION/DOWNGRADING SCHEDULE	
16. DISTRIBUTION STATEMENT (of this Report)  Approved for public release; distribution unlimited.		
17. DISTRIBUTION STATEMENT (of the abstract entered in Block 20, if different from Report)		
18. SUPPLEMENTARY NOTES		
19. KEY WORDS (Continue on reverse side if necessary and identify by block number)  Dynamics                                      Penetration                                      Two-Dimensional Impact shock                                      Fracture (mechanics)                                      Finite element analysis Damage assessment                                      Strain energy density		
20. ABSTRACT (Continue on reverse side if necessary and identify by block number)  (SEE REVERSE)  A		

*This study overcomes previous difficulties in such mathematical descriptions by applying a concept which assumes...*

Block No. 20

*The projectile penetration*

ABSTRACT

The process of projectile penetration covers a wide range of failure modes depending on the impact velocity, configuration and material of the projectile and target. Such behavior has not been adequately described in the classical continuum mechanics of assuming that the constitutive relations in each material element are known a priori. This difficulty has been overcome in this work by application of a new concept assuming that material damage occurs nonhomogeneously throughout the target and can be uniquely associated with the rate at which energy is dissipated in a unit volume of material. Introduced as a corollary of the strain energy density theory are the quantities  $dV/dA$  and  $dW/dV$  which represent, respectively, the rate of change of volume with surface area and the strain energy density function. ~~They~~ together determine the energy used to damage a differential area  $dA$  in the projectile penetration process. The orientations of the damage planes form the failure path.

A numerical procedure is developed for modeling the material damage process during projectile penetration. The progressive damage pattern for each time increment is exhibited where the elements fail nonhomogeneously. For blunt projectiles impacting relatively hard targets, the conditions for plugging failure are met soon after impact with very little flow of material in the radial direction. This mode of failure is investigated by invoking different assumptions in the state of the failed elements. The present model can also treat the phase transformation of solid where shear bands are formed in regions of highly localized energy states.

DAMAGE PREDICTION OF PROJECTILE PENETRATION PROCESS  
BASED ON ENERGY DISSIPATION RATE

by

G. C. Sih and D. H. Song  
Institute of Fracture and Solid Mechanics  
Lehigh University  
Bethlehem, Pennsylvania 18015

November, 1984

Final Report

Contract No. DAAG46-83-K-0158

Prepared for:

Army Materials and Mechanics Research Center  
Watertown, Massachusetts 02172

Accession For	
NTIS CRA&I	<input checked="" type="checkbox"/>
DTIC TAB	<input type="checkbox"/>
Unannounced	<input type="checkbox"/>
Justification .....	
By .....	
Distribution /	
Availability Codes	
Dist	Avail and/or Special
A-1	1



## TABLE OF CONTENTS

	<u>PAGE</u>
FOREWORD	
ABSTRACT	1
INTRODUCTION	2
COROLLARY OF STRAIN ENERGY DENSITY THEORY	4
Length of Homogeneity	5
A Theory of Material Damage	7
FINITE ELEMENT FORMULATION	11
Displacements and Strains	12
Stresses on Damage Plane	17
Nodal Forces	19
Equation of Motion	22
Failure Consideration	24
COMPUTER ALGORITHM	26
IMPACT OF CYLINDRICAL PROJECTILE ON PLATE TARGET: MODEL I AND II	30
Projectile-Target System	34
Material Properties	35
Model I	38
Model II	84
NONHOMOGENEOUS ENERGY DENSITY DISSIPATION RATE	130
REMARKS ON REFINEMENT OF ADED CODE	147
Energy Dissipation Rates	147
Finite Element Size	148
Fragmentations	148

TABLE OF CONTENTS - (CONTINUED)

	<u>PAGE</u>
Fracture Initiation	149
Nonhomogeneous Damping	149
Time Increment or Step	149
Three-Dimensions	150
REFERENCES	151

## FOREWORD

This report contains the complete description of the Axisymmetric Dynamic Energy Density (ADED) Code which was developed by the Institute of Fracture and Solid Mechanics at Lehigh University under Contract No. DAAG46-83-K-0158 supported by the Army Materials and Mechanics Research Center (AMMRC). Special acknowledgements are due to the Project Manager, Mr. J. F. Dignam and Technical Monitor, Dr. S.-C. Chou from AMMRC. Their input and encouragement have been most motivating and made the completion of this work possible. The authors also wish to acknowledge the many helpful discussions by Dr. J. G. Michopoulos of the Institute of Fracture and Solid Mechanics during the early stage of this work.

The damage concept in the ADED program differs fundamentally from all existing codes dealing with penetration mechanics in that the theory of plasticity is no longer employed for describing the permanent deformation of material. Instead, the continuous range of weakened states material elements from the undamaged to the completely damaged states are described by the rates at which energy is dissipated per unit area, the orientation of which can vary for each time step from element to element. The full range of uniaxial strain rates data covering the impact penetration process are consistently translated and used to predict multi-axial stress state behavior in elements that had at one time damaged and/or failed when subjected to compressive stress states can also be distinguished.

The results on plug formation show that ADED Code is fundamentally sound

and can predict all the experimentally observed features of projectile penetration damage based on uniaxial data alone. The quantitative accuracy depends on the completeness of the material data bank and the finite element mesh size. These refinements and modifications can be easily incorporated into the ADED Code. There is no doubt that the program can be further streamlined. Nevertheless, it was considered essential to make this preliminary work available as early as possible to those who have had a long standing interest on this subject.

DAMAGE PREDICTION OF PROJECTILE PENETRATION PROCESS  
BASED ON ENERGY DISSIPATION RATE

by

G. C. Sih and D. H. Song  
Institute of Fracture and Solid Mechanics  
Lehigh University  
Bethlehem, Pennsylvania 18015 USA

ABSTRACT

The process of projectile penetration covers a wide range of failure modes depending on the impact velocity, configuration and material of the projectile and target. Such behavior has not been adequately described by the classical continuum mechanics of assuming that the constitutive relations in each material element are known a priori. This difficulty has been overcome in this work by application of a new concept assuming that material damage occurs nonhomogeneously throughout the target and can be uniquely associated with the rate at which energy is dissipated in a unit volume of material. Introduced as a corollary of the strain energy density theory are the quantities  $dV/dA$  and  $dW/dV$  which represent, respectively, the rate of change of volume with surface area and the strain energy density function. They, together, determine the energy used to damage a differential area  $dA$  in the projectile penetration process. The orientations of the damage planes form the failure path.

A numerical procedure is developed for modeling the material damage process during projectile penetration. The progressive damage pattern for each time increment is exhibited where the elements fail nonhomogeneously. For blunt projectiles impacting relatively hard targets, the conditions for plugging failure are met soon after impact with very little flow of material in the radial direction. This mode

of failure is investigated by invoking different assumptions in the state of the failed elements. The present model can also treat the phase transformation of solid where shear bands are formed in regions of highly localized energy states.

## INTRODUCTION

Penetration mechanics has been a subject of continuing interest because of its importance in military application for developing faster projectiles and stronger armor. The early works in this area are mostly empirical that involve the experimental correlations of such parameters as impact velocity, projectile mass, target thickness, penetration depth, etc. The objective has been to come forth with some understanding on the trade-off between the pertinent variables that govern the scaling of models. These approaches, however, are becoming less and less suitable when applied to explain modern-day technology. They do not lend themselves to any physical insights of the mechanics of penetration and can be costly as the tests involve too many variables. The advent of the modern computer has offered many new and previously untried avenues to research in penetration mechanics.

During the past two decades, the U.S. has expended considerable efforts toward the formulation of sophisticated computer programs [1-3] to explain the dynamic response of materials and the projectile-target failure phenomena. There is, however, considerable diversity in these works, particularly in the application of failure criteria and constitutive relations that involve *a priori* assumption on material behavior and/or location of failure path. Lacking in particular are

(1) *a unique failure criterion that can consistently explain the complete material damage process involving the transformation of solid to liquid and/or gas, and*

(2) *the translation of measured material properties from simple tests to multiaxial stress states or nonhomogeneous energy states in the penetration process.*

The majority of the present-day computer codes in the U.S. have failed to comply with the necessary requirements just stated and hence are limited in their predictive capability. They are usually developed to reproduce the experimentally observed phenomenon of projectile motion and/or target failure and involve many empirical parameters that are problem-specific. This is indicative of the fundamental difficulties associated with the application of continuum mechanics for explaining failure that involves a wide range of energy dissipation rates that occur in the projectile penetration process. Some of these shortcomings are discussed in [4].

Phenomenological investigations of the so-called\* "adiabatic shear bands" have been observed [5] in explosively fragmented shells, impacted plates, projectiles, etc., and studied metallographically in [6]. The highly localized shear strain rate was estimated to be of the order of  $10^5$  to  $10^7$   $\text{sec}^{-1}$  in steel such that phase transformation of the metal can occur. More recently, the same phenomenon has been observed in highly but slowly compressed metal bar specimens [7-9] where ample time was available for heat transfer to take place. White shear bands, however, still appeared in regions of localized deformation. It is, therefore, important to distinguish the transfer of heat at the local from that at the global scale level. A quantitative analysis of the white shear band problem has been carried out in [10] by accounting for the rate at which energy is dissipated to damage the material during loading. It was shown that the excess energy in addition to yield and frac-

---

\* The term adiabatic was invoked to describe the process of impact occurring so quickly that little or no time is left for heat transfer to take place between the system and its surrounding.

ture of the 4340 steel cylinder in compression contributes to intense local heating that can lead to phase transformation.

The main objective of the present work is to provide a methodology that can analyze the complete projectile impact damage process. Incorporated into the numerical scheme is the strain energy density criterion [4,11-13] that is valid to general loading conditions, material types and structure configurations. The initial effort is to develop the algorithm for carrying an analytical description of the damage process leaving out the details of shear band formation and material in the hydrodynamic state. To reiterate, the basic approach is able to describe all failure modes depending on the energy dissipation rates. This includes the transformation of solid to liquid and/or gas.

#### COROLLARY OF STRAIN ENERGY DENSITY THEORY

The selection of failure criterion for describing impact damage has been problematic. A common procedure is to compare experimental data with theoretical predictions based on different assumptions. This approach, however, is not adequate because the differences between the results cannot be clearly identified with physics. The merits of any failure criterion should be judged by its versatility and usefulness in explaining a wide range of physical phenomena and is free from self-contradictions\*. There is also the fundamental problem of translating the nonlinear uniaxial data to elements in a structure whose stress or energy states vary from one location to another. At present, the only widely used theory for describing

---

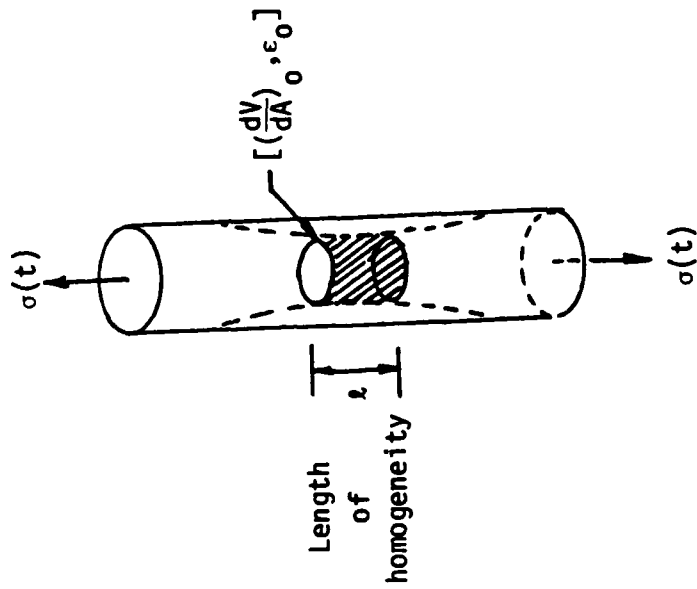
\*The maximum normal stress criterion, for example, contradicts itself when applied to the running crack problem where the maximum stress component acts parallel to the crack plane rather than normal to it as required in the original assumption.

nonlinear material behavior is that of plasticity where yielding\* is considered to be the mechanism of progressive damage before fracture. Difficulties in scaling the grid patterns also arise when applying numerical methods such as finite differences and finite elements. The continuum mechanics theories are developed by assuming that the rate of change of volume with surface area for each element tends to zero, i.e.,  $dV/dA \rightarrow 0$ . Such a condition, of course, cannot be physically realized in the numerical analysis and significant errors can result in situations where  $dV/dA$  undergoes large gradients due to inappropriate selection of mesh size distribution. Even more significant is the role that  $dV/dA$  plays in uniaxial testing which will be discussed subsequently.

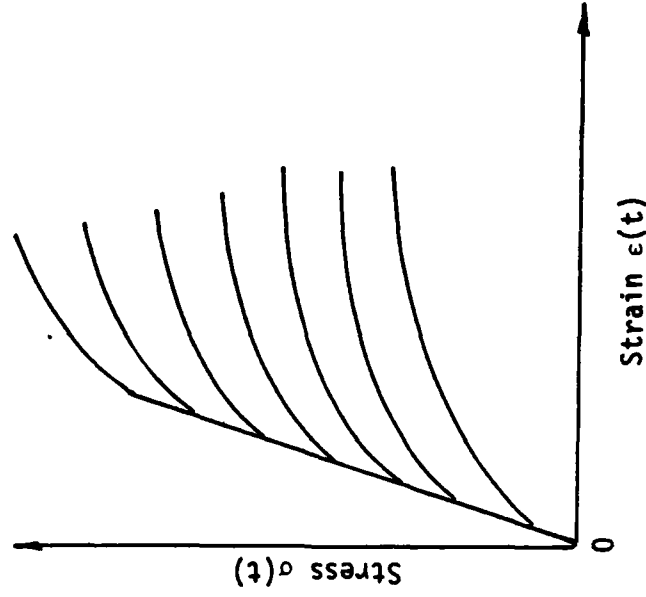
*Length of Homogeneity.* In the mechanical testing of uniaxial specimens, it is necessary to define the resolution of measurements in terms of at least a length parameter, say  $\lambda$  in Figure 1(a), that describes the degree of uniformity or homogeneity of the stress or energy state. For a linear response of the uniaxial stress and strain, the parameter  $dV/dA$  remains constant while  $dV/dA$  changes in the case of nonlinear behavior. The rate of change of  $dV/dA$  with time is indicative of progressive material damage. For a given material or microstructure, loading rate and/or specimen size may be altered to construct a data bank consisting of a family of curves, Figure 1(b). Each point on these curves can be uniquely identified by defining  $dV/dA$  and  $\epsilon$  instead of  $\sigma$  and  $\epsilon$ . Since  $dV/dA$  is a geometrically determinable quantity that can be easily computed or measured for an uniaxial specimen and transferred to elements in a complex stress state, it can be used to preserve the

---

\*The assumption of the uniaxial stress and strain curve to coincide with the effective stress and effective strain curve is inadequate for situations where dilatation also contributes to failure such as elements near the crack tip.



(a) Uniaxial specimen



(b) Stress and strain response

Figure 1. Uniaxial data bank for different combination of loading rate and/or specimen size.

plane of homogeneity\* in the uniaxial test to the plane on which damage is predicted to take place. That is to establish a relation between  $[(dV/dA)_0, \epsilon_0]$  and  $[(dV/dA)_i, \epsilon_i]$ . Let  $\alpha$  be the angle between these two planes, then

$$\left(\frac{dV}{dA}\right)_i = \left(\frac{dV}{dA}\right)_0 \cos\alpha \quad (1)$$

in which  $(dV/dA)_i$  refers to homogeneity associated with  $i$ th plane and  $(dV/dA)_0$  with  $\alpha=0$  coinciding with the damage plane in the uniaxial test. There remains the problem of translating the uniaxial strain quantity  $\epsilon$  to the multiaxial strain state even though the stress quantity  $\sigma$  is no longer directly involved in representing the uniaxial data. This involves the application of a corollary of the strain energy density theory that leads directly to a new damage theory in continuum mechanics that includes plasticity, viscoplasticity, etc., as special cases.

*A Theory of Material Damage.* The strain energy density criterion in its original form [11-13] assumes that the strain energy density function,  $dW/dV$ , varies from one location to another. The fluctuation gives rise to peaks and valleys which in mathematical terms are the stationary values of  $dW/dV$ . The basic postulate is that *progressive material damage can be uniquely associated with the rate at which energy is dissipated in a unit volume of material.* In other words, failure modes at different scale levels are assumed to be uniquely related to thresholds of  $dW/dV$  which are experimentally measurable. In the uniaxial tests,  $dW/dV$  represents the area under the true stress and true strain curve depending on the temperature and moisture level:

---

\* Homogeneity can change from element to element in a solid as the interaction of material with loading is nonuniformly distributed.

$$\frac{dW}{dV} = \int_0^{\epsilon_{ij}} \sigma_{ij} d\epsilon_{ij} + f(\Delta T, \Delta C) \quad (2)$$

with  $\Delta T$  and  $\Delta C$  being changes in temperature and moisture concentration\*. The stress and strain components are denoted by  $\sigma_{ij}$  and  $\epsilon_{ij}$ , respectively.

In order to transfer the homogeneity of the damage plane in the uniaxial test to the prospective plane of failure of an element in multiaxial stress state, it is necessary to introduce a corollary of the strain energy density theory. It may be stated as follows:

*The failure of an element is assumed to occur on the  $i$ th plane by matching  $(dW/dA)_i$  with measurable uniaxial data.*

For an element,  $(dW/dA)_i$  can be written as

$$\left(\frac{dW}{dA}\right)_i = \left(\frac{dV}{dA}\right)_i \left(\frac{dW}{dV}\right) \quad (3)$$

in which  $dW/dV$  is a scalar and  $(dV/dA)_i$  is proportional to the slope of the stress and strain curve. Since equation (3) must be unique for a given element, the  $i$ th direction can be determined from the condition

$$\left(\frac{dV}{dA}\right)_i = \text{const.}, \quad i = \xi, \eta \quad (4)$$

In two dimensions, equation (4) or

---

\* Equation (2) shows that energy can be stored in a material even when the stresses are zero. Hence, any failure criteria based on stress quantities alone are necessarily limited in application.

$$\left(\frac{dV}{dA}\right)_{\xi} = \left(\frac{dV}{dA}\right)_{\eta} \quad (5)$$

yields the angle  $\alpha$  between  $(\xi, \eta)$  and  $(x, y)$ . The reference damage plane is assumed to coincide with  $(x, y)$ . If the material is isotropic and homogeneous\*, equation (5) reduces to

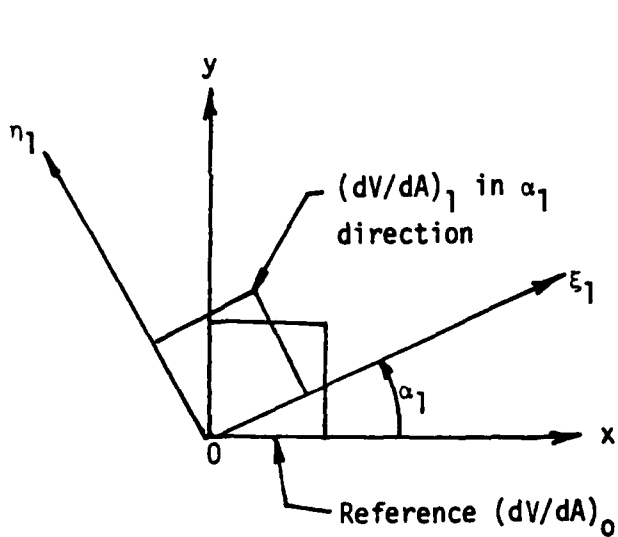
$$\epsilon_{\xi} = \epsilon_{\eta} \quad (6)$$

These are not the principal strains but those acting on the plane with the same  $dV/dA$  value as that in the uniaxial test. In view of equations (5) and (6), homogeneity of the multiaxial stress or energy state can be described by  $[(dV/dA)_{\xi}, \epsilon_{\xi}]$  or  $[(dV/dA)_{\eta}, \epsilon_{\eta}]$  and related to the uniaxial data  $[(dV/dA)_{\epsilon_0}, \epsilon_0]$ .

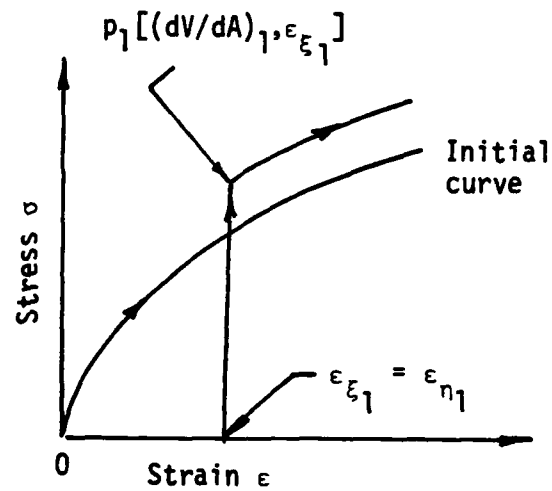
A theory of material damage follows immediately. As the uniaxial data bank provides known values of  $(dV/dA)_i$  and  $dW/dV$  for each energy state, the actual stress and strain path of each element can be derived as the system is loaded incrementally. The procedure for constructing the stress and strain history of a typical element is illustrated schematically in Figures 2 and 3.

An initial stress and strain of a given element is assumed for the first load increment. Equation (6) is then applied to find  $\alpha_1$ ,  $(dV/dA)_1$ , and  $\epsilon_{\xi_1} = \epsilon_{\eta_1}$ . The predicted damage state makes an angle  $\alpha_1$  with the reference state, Figure 2(a). This locates the point "p<sub>1</sub>" in the data bank with coordinates  $[(dV/dA)_1, \epsilon_{\xi_1}]$  as shown in Figure 2(b). The next increment of loading gives  $\alpha_2$ ,  $(dV/dA)_2$  and  $\epsilon_{\xi_2} = \epsilon_{\eta_2}$ , and hence the point "p<sub>2</sub>" is obtained, Figures 3(a) and (b). A series of

\* Expression similar to equation (6) may be deduced for anisotropic and nonhomogeneous materials in which case the relation between  $\epsilon_{\xi}$  and  $\epsilon_{\eta}$  will involve material constants.

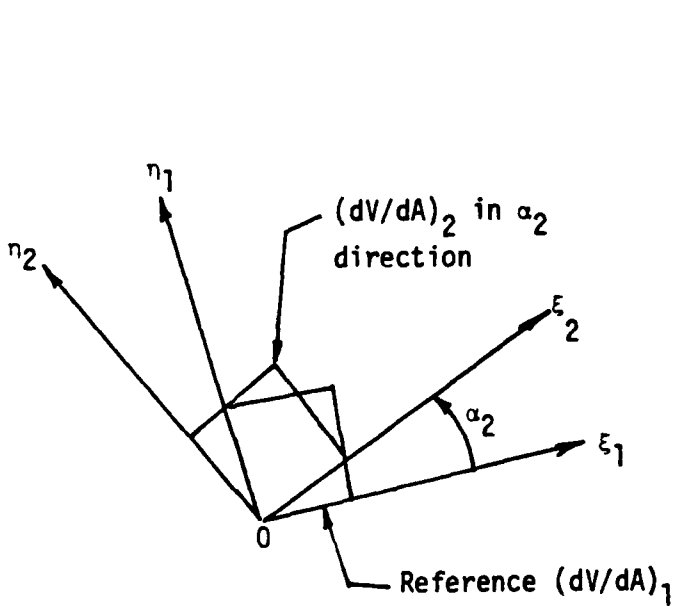


(a) Direction of homogeneity  $\alpha_1$

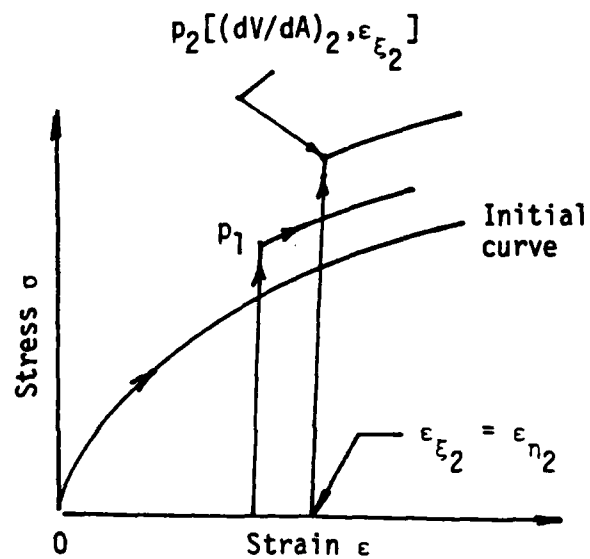


(b) Location of point  $p_1$

Figure 2. Searching of point  $p_1$  in data bank for the first load increment.



(a) Direction of homogeneity  $\alpha_2$



(b) Location of point  $p_2$

Figure 3. Searching of point  $p_2$  in data bank for the second load increment.

points  $p_1$ ,  $p_2$ , etc., are found until the complete stress and strain history is derived. Unloading can also be accomplished incrementally in the same way. Each element will follow its own path of loading or unloading. The energy dissipated in damaging each element can be assessed with accuracy.

Preliminary results have been obtained for structural members undergoing static, dynamic and fatigue loadings. They indeed exhibit the trend anticipated on physical grounds. In the case of a slowly growing crack in a stretched plate [14], the equivalent uniaxial stress and strain response in elements near the crack tip experiencing more dilatation is quite different from those away from the crack where the plasticity solution gave reasonable results. At the immediate vicinity of the crack tip, large deviations are expected since plasticity accounts only for distortion. Moreover, the damage theory predicts a much sharper rise in the stress components as the crack tip is approached. The gradient changes for each increment of crack growth.

#### FINITE ELEMENT FORMULATION

The finite element method will be used to divide the projectile-target system into a network of triangular elements such that each element possesses three nodes identified by a convenient coordinate system. In the case of axisymmetry where the projectile has a circular cross-section, the  $(r, \theta, z)$  system will be adopted. Since the result does not vary with  $\theta$ , it suffices to consider the plane  $r$  and  $z$  as shown in Figure 4. A typical triangular element with nodes  $i$ ,  $j$  and  $k$  is referred to in a counterclockwise direction. A composite matrix can thus be formed for the projectile-target system that relates the displacements of the nodal points of each element to the external forces in the dynamic structure. Once the displacement field is known, the incremental strain can then be evaluated from the displacement incre-

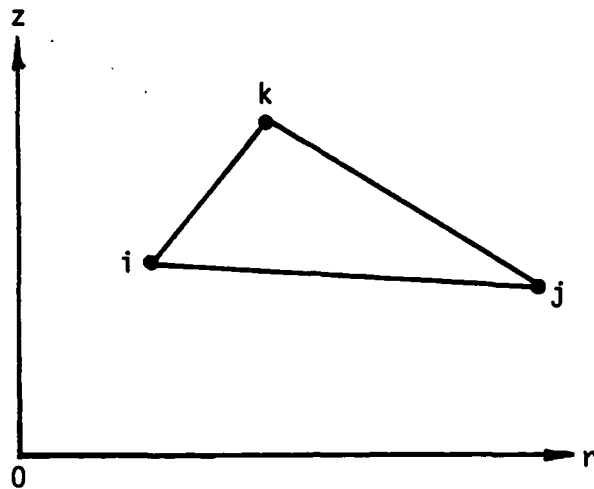


Figure 4. A typical triangular element in rz-plane.

ment. At this point, the procedure deviates from the classical approach where the stresses are obtained from the strains via a pre-assigned constitutive relation. The newly proposed damage model utilizes the uniaxial data stored in the bank covering a wide range of strain rates that may differ from element to element for each increment of loading or projectile advancement. Based on the damage criterion given by equation (3), the equivalent uniaxial stress and strain history for each element can be derived.

*Displacements and Strains.* For problems with axial symmetry, the displacement vector, say  $\underline{u}$ , depends only on the variables  $r$  and  $z$  as shown in Figure 4. Let  $u_r$  and  $u_z$  be the displacement components in the  $r$ - and  $z$ -direction of  $\underline{u}$  associated with an element:

$$\{\underline{u}\} = \begin{Bmatrix} u_r \\ u_z \end{Bmatrix} \quad (7)$$

The displacement vectors of the nodal points  $i, j, k$  denoted by  $\underline{u}^i, \underline{u}^j$  and  $\underline{u}^k$  will each have their corresponding components in the  $r$ - and  $z$ -direction as follows:

$$\{\underline{u}^i\} = \begin{Bmatrix} u_r^i \\ u_z^i \end{Bmatrix}, \{\underline{u}^j\} = \begin{Bmatrix} u_r^j \\ u_z^j \end{Bmatrix}, \{\underline{u}^k\} = \begin{Bmatrix} u_r^k \\ u_z^k \end{Bmatrix} \quad (8)$$

For the triangular element, the displacement varies linearly with  $r$  and  $z$ , i.e.,

$$\{\underline{u}(r,z)\} = \{\underline{\alpha}_1\} + \{\underline{\alpha}_2\}r + \{\underline{\alpha}_3\}z \quad (9)$$

in which  $\{\underline{\alpha}_1\}, \{\underline{\alpha}_2\}$  and  $\{\underline{\alpha}_3\}$  are column vectors that can be expressed in terms of  $\{\underline{u}^i\}, \{\underline{u}^j\}$  and  $\{\underline{u}^k\}$ , i.e.,

$$\{\underline{u}(r,z)\} = \frac{1}{2D} \sum_{e=i,j,k} (a_e + b_e r + c_e z) \{\underline{u}^e\} \quad (10)$$

such that

$$a_i = r_j z_k - r_k z_j, \quad b_i = z_j - z_k, \quad c_i = r_k - r_j \quad (11)$$

The other expressions  $a_j, b_j$ , etc., can be obtained by cyclic permutation of the indices  $i, j$  and  $k$ . The quantity  $D$  stands for the area of the element  $i, j$  and  $k$  and is given by

$$D = \frac{1}{2} \det \begin{vmatrix} 1 & r_i & z_i \\ 1 & r_j & z_j \\ 1 & r_k & z_k \end{vmatrix} \quad (12)$$

The current strain  $\underline{\epsilon}$  at time  $t$  will be calculated from the incremental strain  $\Delta \underline{\epsilon}$  at  $\Delta t$  as follows:

$$\{\underline{\epsilon}\}_t = \{\underline{\epsilon}\}_{t-\Delta t} + \{\Delta \underline{\epsilon}\}_{\Delta t} \quad (13)$$

where  $\{\underline{\epsilon}\}_{t-\Delta t}$  is the strain vector at time  $t-\Delta t$ . The components of  $\underline{\epsilon}$  are

$$\{\underline{\epsilon}\} = \begin{Bmatrix} \epsilon_r \\ \epsilon_z \\ \epsilon_\theta \\ \gamma_{rz} \end{Bmatrix} \quad (14)$$

Starting with a zero state of initial strain, i.e.,  $\{\underline{\epsilon}\}_0 = 0$ , the strain increment  $\Delta \underline{\epsilon}$  can be calculated from the displacement increment  $\Delta \underline{u}$  as given by

$$\{\Delta \underline{\epsilon}\} = \begin{Bmatrix} \Delta \epsilon_r \\ \Delta \epsilon_z \\ \Delta \epsilon_\theta \\ \Delta \gamma_{rz} \end{Bmatrix} = \begin{Bmatrix} \frac{\partial(\Delta u_r)}{\partial r} \\ \frac{\partial(\Delta u_z)}{\partial z} \\ \frac{\Delta u_r}{r} \\ \frac{\partial(\Delta u_r)}{\partial z} + \frac{\delta(\Delta u_z)}{\partial r} \end{Bmatrix} \quad (15)$$

Making use of the relations in equation (10), it follows that

$$\{\Delta\epsilon\} = \frac{1}{2D} \left\{ \begin{array}{l} \sum_{e=i,j,k} b_e (\Delta u_r)^e \\ \sum_{e=i,j,k} c_e (\Delta u_z)^e \\ \sum_{e=i,j,k} \left( \frac{a_e}{r} + b_e + c_e \frac{z}{r} \right) (\Delta u_r)^e \\ \sum_{e=i,j,k} [c_e (\Delta u_r)^e + b_e (\Delta u_z)^e] \end{array} \right\} \quad (16)$$

The above matrix expression may be written as

$$\{\Delta\epsilon\} = [B_i, B_j, B_k] \left\{ \begin{array}{l} \{\Delta u^i\} \\ \{\Delta u^j\} \\ \{\Delta u^k\} \end{array} \right\} \quad (17)$$

provided that  $[B_e]$  ( $e = i, j, k$ ) is the following  $4 \times 2$  matrix:

$$[B_e] = \frac{1}{2D} \begin{vmatrix} b_e & , & 0 \\ 0 & , & c_e \\ \frac{a_e}{r} + b_e + c_e \frac{z}{r} & , & 0 \\ c_e & , & b_e \end{vmatrix} \quad (18)$$

Because of the dependency of  $[B_e]$  on  $r$  and  $z$ , the strains in the element are no longer constant as in the problem of plane extension. Referring  $\bar{B}_e$  to the centroid of the element located at

$$\bar{r} = \frac{r_i + r_j + r_k}{3}, \quad \bar{z} = \frac{z_i + z_j + z_k}{3} \quad (19)$$

equation (17) becomes

$$\{\Delta \underline{\epsilon}\} = [\bar{B}_i, \bar{B}_j, \bar{B}_k] \begin{Bmatrix} \{\Delta \underline{u}^i\} \\ \{\Delta \underline{u}^j\} \\ \{\Delta \underline{u}^k\} \end{Bmatrix} \quad (20)$$

Equation (20) may be expressed simply as

$$\{\Delta \underline{\epsilon}\} = [\bar{B}] \{\Delta \underline{u}^e\} \quad (21)$$

in which

$$[\bar{B}] = [\bar{B}_i, \bar{B}_j, \bar{B}_k] \quad (22)$$

is a 4x6 matrix. With reference to  $[\bar{B}]$ , equation (21) yields constant strain in the element. In equation (21),  $\underline{u}^e$  is given by

$$\{\underline{u}^e\} = \begin{Bmatrix} \{\underline{u}^i\} \\ \{\underline{u}^j\} \\ \{\underline{u}^k\} \end{Bmatrix} \quad (23)$$

*Stresses on Damage Plane.* The nonhomogeneity caused by the variation of  $dV/dA$  throughout the projectile-target system can strongly affect the translation of uniaxial data to the multi-axial stress state. Equations (5) and (6) reveal that the normal strain components control this effect. Their stress and strain behavior must be derived in accordance with the degree of nonlinearity or material damage at each point for each time step. More specifically, the location of the damage plane determined by the angle  $\alpha$  in the  $rz$ -plane must be found from equation (6) for a material that is initially homogeneous and isotropic.

The stress tensor  $\underline{\sigma}$  contains only four components:

$$\{\underline{\sigma}\} = \begin{Bmatrix} \sigma_r \\ \sigma_z \\ \sigma_\theta \\ \tau_{rz} \end{Bmatrix} \quad (24)$$

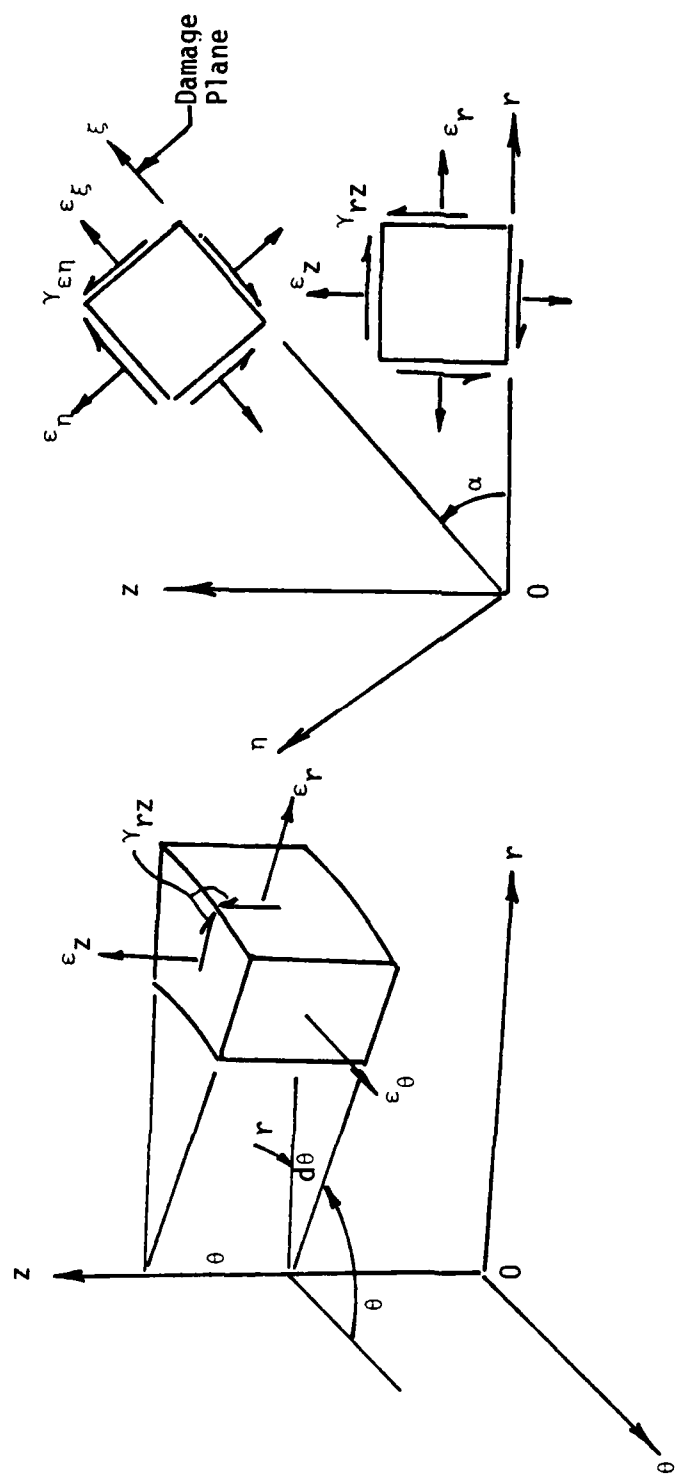
They correspond to the strain components in Figure 5(a). Because of axial symmetry, changes in the  $\theta$ -direction are constrained and only the normal strains  $\epsilon_r$  and  $\epsilon_z$  are involved in the adjustment for variation in  $dV/dA$ . Referring to Figure 5(b), the change of volume with respect to surface area in the  $\xi$  and  $\eta$  direction can be written as\*

$$\left(\frac{dV}{dA}\right)_\xi = \frac{(\epsilon_\xi + \epsilon_\eta)\cos\alpha + \epsilon_\theta}{(\epsilon_\eta \cos\alpha + \epsilon_\theta)\cos\alpha} \quad (25)$$

and

$$\left(\frac{dV}{dA}\right)_\eta = \frac{(\epsilon_\xi + \epsilon_\eta)\cos\alpha + \epsilon_\theta}{(\epsilon_\xi \cos\alpha + \epsilon_\theta)\cos\alpha} \quad (26)$$

\*For axisymmetry,  $(dV/dA)_\theta = C(r,z)$  and  $\epsilon_\theta$  in equations (25) and (26) can be eliminated and expressed in terms of  $C(r,z)$ . The classical plane strain condition can be realized by letting  $C \rightarrow 1$ .



(a) Axial Symmetric Strain State

(b) Strain State on Damage Plane

Figure 5. Schematic of strain state and damage plane.

Here,  $(dV/dA)_\xi$  or  $(dV/dA)_\eta$  is related to  $(dV/dA)_i$  in equation (1) through  $\cos\alpha$ . As a result of the corollary of the strain energy density theory, equation (5) when applied to equations (25) and (26) leads to the conclusion given in equation (6) or the condition  $\epsilon_\xi = \epsilon_\eta$ . This determines the orientation of the damage plane through  $\alpha$  such that the appropriate strain rate from the uniaxial data can be correctly transferred to each element in the projectile-target system. Note that the shear strain component  $\gamma_{rz}$  does not appear in equations (25) nor (26). It is therefore related to  $\tau_{rz}$  in the usual manner through the shear modulus  $G$ .

Once  $[(dV/dA)_{\xi, \epsilon_\xi}]$  or  $[(dV/dA)_{\eta, \epsilon_\eta}]$  are determined for each element and each time step,  $\sigma_\xi$  and  $\sigma_\eta$  can be found from the material data bank such as that illustrated schematically in Figure 1(b). Mathematically speaking,  $\sigma_\xi$  or  $\sigma_\eta$  can be obtained from the relation

$$\sigma_\xi \text{ or } \sigma_\eta = \begin{cases} E(\epsilon_\xi \text{ or } \epsilon_\eta), & \epsilon_\xi \text{ or } \epsilon_\eta \leq \epsilon_y \\ E(\epsilon_\xi \text{ or } \epsilon_\eta) - \beta\sigma_y \left[ \left( \frac{\epsilon_\xi \text{ or } \epsilon_\eta}{\epsilon_y} \right)^\gamma - 1 \right], & \epsilon_\xi \text{ or } \epsilon_\eta > \epsilon_y \end{cases} \quad (27)$$

where  $E$ ,  $\sigma_y$  and  $\epsilon_y$  are respectively the Young's modulus, yield strength and strain at yield. The parameters  $\beta$  and  $\gamma$  can be found numerically after the stress and strain for a given element has been traced for many time steps. The stress component  $\sigma_\theta$  is related to  $\epsilon_\theta$  by an expression similar to that given by equation (27). The stresses in the triangular elements are constant as a consequence of constant strains or equation (21).

*Nodal Forces.* Once the stresses within each element are found, they can be used to determine the forces acting on each node which are equilibrated with the boundary

tractions. The corresponding nodal displacements can then be obtained by lumping the mass of the element at the nodes. To this end, the principle of virtual work will be employed. Applied will be the condition that *if the nodes are in equilibrium, the total virtual work done by the forces acting through any arbitrary virtual nodal displacements that are consistent with the constraints must be zero.*

Let the nodal forces be denoted in matrix form as

$$\{F^e\} = \begin{Bmatrix} \{F^i\} \\ \{F^j\} \\ \{F^k\} \end{Bmatrix} \quad (28)$$

For an arbitrary nodal virtual displacement  $\delta \underline{u}^e$ , the principle of virtual work may be applied to yield

$$\{\delta \underline{u}^e\}^T \{F^e\} + \int_V [\{\delta \underline{\epsilon}\}^T \{\underline{\sigma}\} - \{\delta \underline{u}\}^T \{\underline{f}\}] dV - \int_A \{\delta \underline{u}\}^T \{\underline{T}\}^n dA = 0 \quad (29)$$

in which  $\underline{f}$  and  $\underline{T}^n$  are respectively the body force and traction vector. The quantity  $\delta \underline{\epsilon}$  is the virtual strain corresponding to the virtual displacement  $\delta \underline{u}$ . In the absence of body force and boundary tractions, equation (29) reduces to

$$\{\delta \underline{u}^e\}^T \{F^e\} = - \int_V \{\delta \underline{\epsilon}\}^T \{\underline{\sigma}\} dV \quad (30)$$

With the aid of equation (21), it follows that

$$\{\delta \underline{u}^e\}^T \{F^e\} = - \int_V \{\delta \underline{u}^e\}^T [\underline{B}]^T \{\underline{\sigma}\} dV \quad (31)$$

Since  $\{\delta u^e\}^T$  is arbitrary and is independent of the volume integral, equation (30) becomes

$$\{F^e\} = - \int_V [B]^T \{\sigma\} dV \quad (32)$$

For the  $\ell$ th node, the force vector may be written as

$$\{F^\ell\} = - \int_V [B^\ell]^T \{\sigma\} dV \quad (33)$$

in which  $[B^\ell]^T$  is given by

$$[B^\ell]^T = \frac{1}{2D} \begin{vmatrix} b_e & 0 & \frac{a_e + b_e \bar{r} + c_e \bar{z}}{\bar{r}} & c_e \\ 0 & c_e & 0 & b_e \end{vmatrix} \quad (34)$$

The quantities  $D$ ,  $a_e$ , etc., are the same as those defined earlier. The volume integration in equation (33) may be carried out by recalling that the stresses are constant within each volume element and applying equation (24) the nodal forces components  $F_r^i$ ,  $F_z^i$ , etc., are found. With  $2\pi\bar{r}A$  being the volume of an element, the expressions for  $F_r^i$  and  $F_z^i$  are

$$F_r^i = - \pi\bar{r}[(z_j - z_k)\sigma_r + (r_k - r_j)\tau_{rz}] - \frac{2\pi}{3} A\sigma_\theta \quad (35)$$

$$F_z^i = - \pi\bar{r}[(r_k - r_j)\sigma_z + (z_j - z_k)\tau_{rz}]$$

where  $F_\theta^i = 0$ . The forces on the other nodes such as  $F_r^j$ ,  $F_z^j$ , etc., can be obtained by cyclic permutation of the indices.

Equation of Motion. By distributing the mass of the element evenly at the three nodal points and applying the nodal forces in equation (35), the acceleration at the nodes may be obtained:

$$\{\ddot{u}^e\}_t = \frac{\{F^e\}_t}{M^e} \quad (36)$$

where  $M^e$  stands for the lumped mass at the eth node. The velocity vector can thus be found by integrating equation (36). Assuming that the acceleration is constant for a small time increment  $\Delta t$ , then

$$\{\dot{u}^e\}_{t^+} = \{\dot{u}^e\}_{t^-} + \{\ddot{u}^e\}_t \overline{\Delta t} \quad (37)$$

Referring to Figure 6,  $\{\dot{u}^e\}_{t^+}$  and  $\{\dot{u}^e\}_{t^-}$  are the velocities just after and before the current time  $t$  and  $\overline{\Delta t}$  stands for the average time increment about  $t$ , i.e.,

$$\overline{\Delta t} = \frac{(\Delta t)_{t^-} + (\Delta t)_{t^+}}{2} \quad (38)$$

At incipient impact  $t=0$ ,  $\{\dot{u}^e\}_{t^-}$  are the initial velocities of those nodes in the projectile which come in contact with the target such that  $\{\ddot{u}^e\}_t \equiv 0$  for  $(\Delta t)_{t^-}$ . Assuming that the velocities are constant over the time increment  $\Delta t$ , equation (37) can be integrated to yield the nodal displacements

$$\{u^e\}_{t+\Delta t} = \{u^e\}_t + \{\dot{u}^e\}_{t^+} (\Delta t)_{t^+} \quad (39)$$

where

$$\{\Delta u^e\} = \{\dot{u}^e\}_{t^+} (\Delta t)_{t^+} \quad (40)$$

is, in fact, the incremental displacement. The nodal coordinates are then obtained from the displacements:

$$\{x^e\}_{t+\Delta t} = \{x\}_t + \{u^e\}_{t+\Delta t} \quad (41)$$

To summarize, the nodal velocities are calculated at the mid-point of the time interval which represents the average velocities during the time increment  $\Delta t$ . The nodal displacements and accelerations are defined at the beginning or the end of the time increment. Refer to Figure 6 for a pictorial representation of their definitions. Use is made of the "sliding-surface" technique developed in [15] at the contact surface of projectile and target.

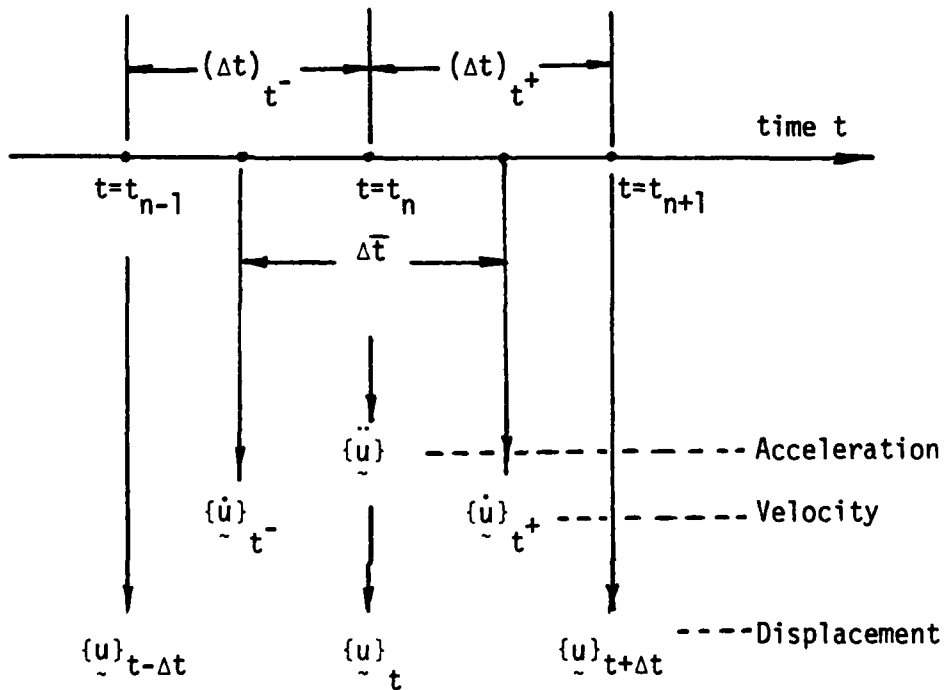


Figure 6. Interpretation of displacement, velocity and acceleration at different time.

*Failure Consideration.* By application of the conditions given in equations (5) and (6), the orientation of the damage plane defined by the angle  $\alpha$  in Figure 5(b) is first obtained. The quantities  $(dV/dA)_\xi$  or  $(dV/dA)_\eta$  in equations (25) or (26) must then be related to  $(dV/dA)_o$  obtained from the uniaxial data, say in Figures 1. This is accomplished by application of equation (1) such that  $(dV/dA)_i$  in equation (3) stands for  $(dV/dA)_\xi/\cos\alpha$  or  $(dV/dA)_\eta/\cos\alpha$ . At a particular state, say p, on the true stress and true strain curve in Figure 7,  $dV/dA$  being proportional to the slope can be expressed by a length parameter, say  $h_p$ . The element is partially damaged as the unloading path pq will not coincide with the loading path oy which is a straight line, the reversible path. The shaded area oypq is the energy dissipated per unit volume that is not recoverable. According to equation (3), the damage is

$$\left(\frac{dW}{dA}\right)_{\xi \text{ or } \eta} = h_p \left(\frac{dW}{dV}\right)_p \quad (42)$$

such that

$$h_y \left(\frac{dW}{dV}\right)_y < \left(\frac{dW}{dA}\right)_{\xi \text{ or } \eta} \leq h_c \left(\frac{dW}{dV}\right)_c \quad (43)$$

The quantities  $h_y$  and  $h_c$  are related to the slopes of the true stress and true strain curve at y and c in Figure 7 and  $(dW/dV)_y$  and  $(dW/dV)_c$  correspond to the areas oyy' and oycc', respectively. An element is assumed to have failed when

$$\left(\frac{dW}{dA}\right)_{\xi \text{ or } \eta} > h_c \left(\frac{dW}{dV}\right)_c \quad (44)$$

This condition should be carefully distinguished from that in equations (42) or (43). In the present analysis, the progressive damage of all elements is moni-

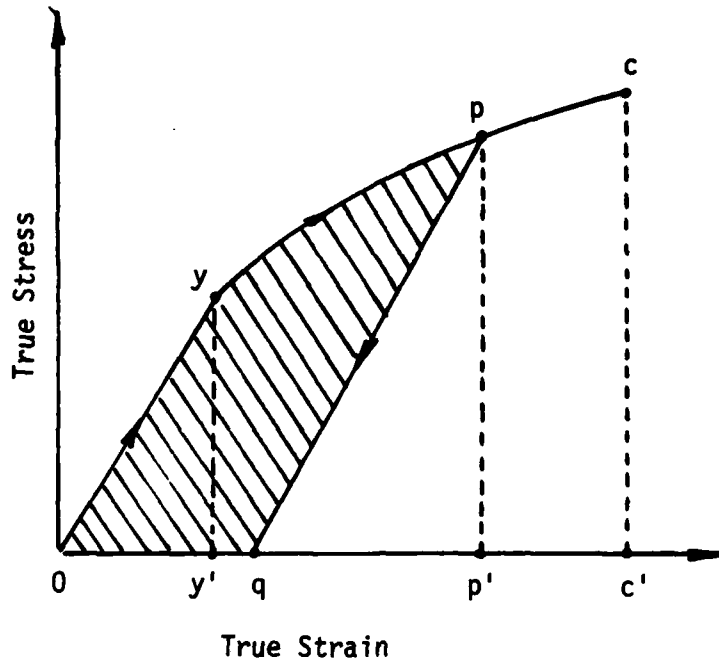


Figure 7. True stress versus true strain.

tored at all time. Those reaching the condition in equation (44) are considered to be failed and the elements will be removed completely from the finite element grid pattern with appropriate adjustment made on the stress state due to changes in geometric configuration and/or the initiation of cavities or cracks in directions dictated by the strain energy density theory.

For the projectile-target problem, the failed elements can still be entrapped in the system and interact with the others as the damage process continues\*. In the absence of strain rate data on the projectile and target material, two sets of true stress and true strain will be constructed analytically in accordance with the generally accepted trade-off relationship between yield strength and fracture toughness. These two cases will be referred to as Model I and II.

\*The solid may transform to liquid and/or gas at high impact velocity such that the rates of energy dissipation can no longer be adequately described by the area under the true stress and true strain curve. The Hugoniot relation expressing the hydrodynamic effects of material may come into play. This will be discussed subsequently.

Model I - The projectile and target material are assumed to possess a relatively *low fracture toughness* for the range of strain rates considered.

Model II - The projectile and target material are assumed to have a relatively *high fracture toughness* for the range of strain rates considered.

The corresponding yield stresses or stresses at which permanent deformation occurs are kept about the same in both models. The time leading to plugging failure will be predicted and compared so that the sensitivity of experimental strain rate data on progressive failure can be demonstrated and better understood.

#### COMPUTER ALGORITHM

The computer algorithm consists of three main portions. They are referred to as INITI, SEDDM and SPLOT. Table 1 shows the flow chart for INITI that deals with the initial input data on material properties, grid generation for the projectile-target system and the relevant parameters that are required for carrying out the failure analysis. The chart in Table 2 gives an overall view of SEDDM that incorporates the strain energy density theory for evaluating the damage and failure of all elements. Sliding nodes are introduced at the interface where projectile comes into contact with the target in order to ensure displacement compatibility and to avoid overlapping or interpenetration of material points. The damage and failure pattern for each time increment can be exhibited graphically via the SPLOT routine shown in Table 3. Contours of constant  $\alpha$  can also be plotted to determine the path of plugging for each time increment  $\Delta t$  which is chosen according to the interaction of stress waves with the finite element. If  $\delta_{\min}$  denotes the minimum dimension of the triangular element, then  $\Delta t$  should be smaller than the time required for the stress wave to travel across  $\delta_{\min}$ , i.e.,

$$\Delta t < \text{Min} \left( \frac{\delta_{\min}}{c} \right) \quad (45)$$

Table 1. Flow Chart of INITI: Preprocessing

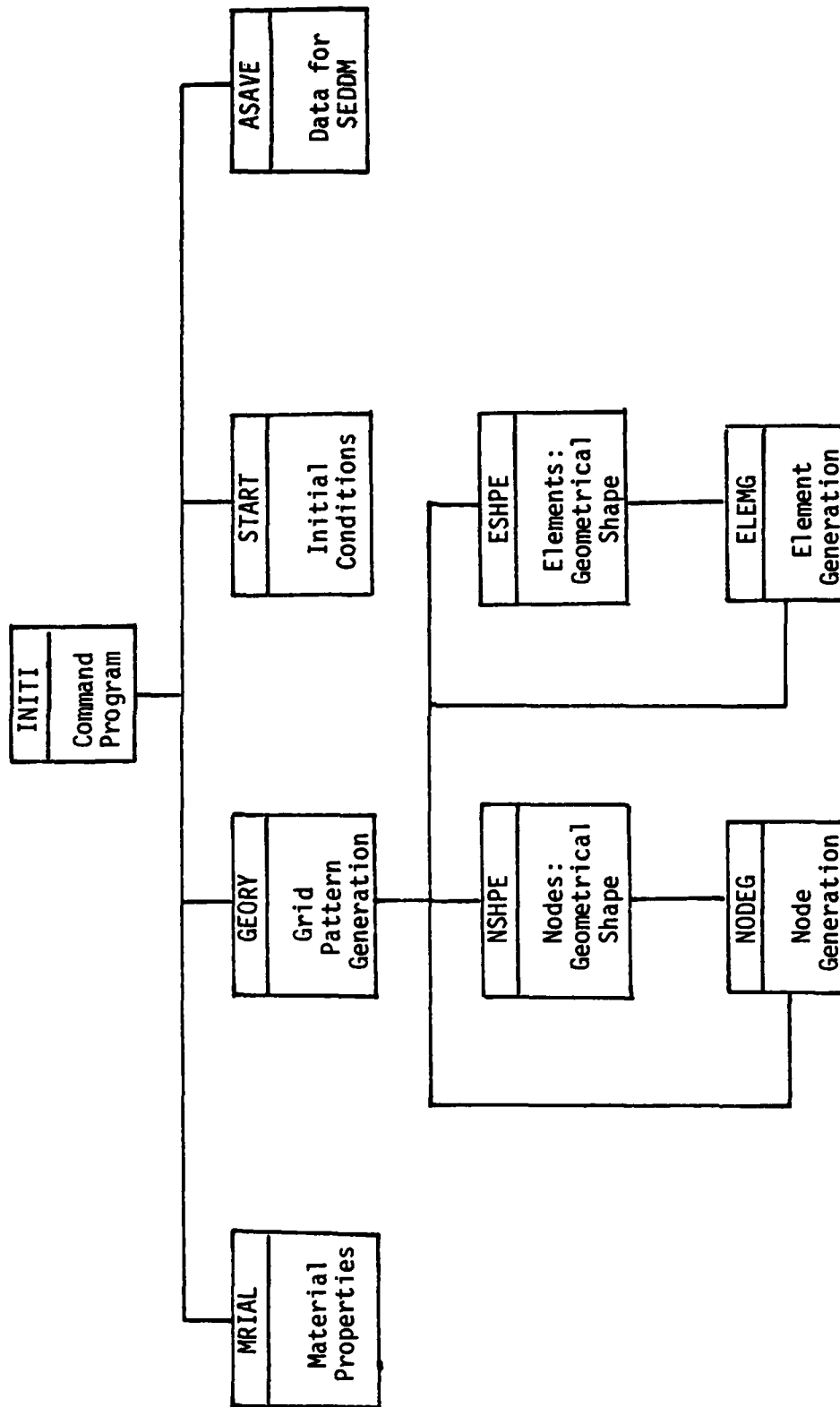


Table 2. Flow Chart for SEDDM: Failure Analysis

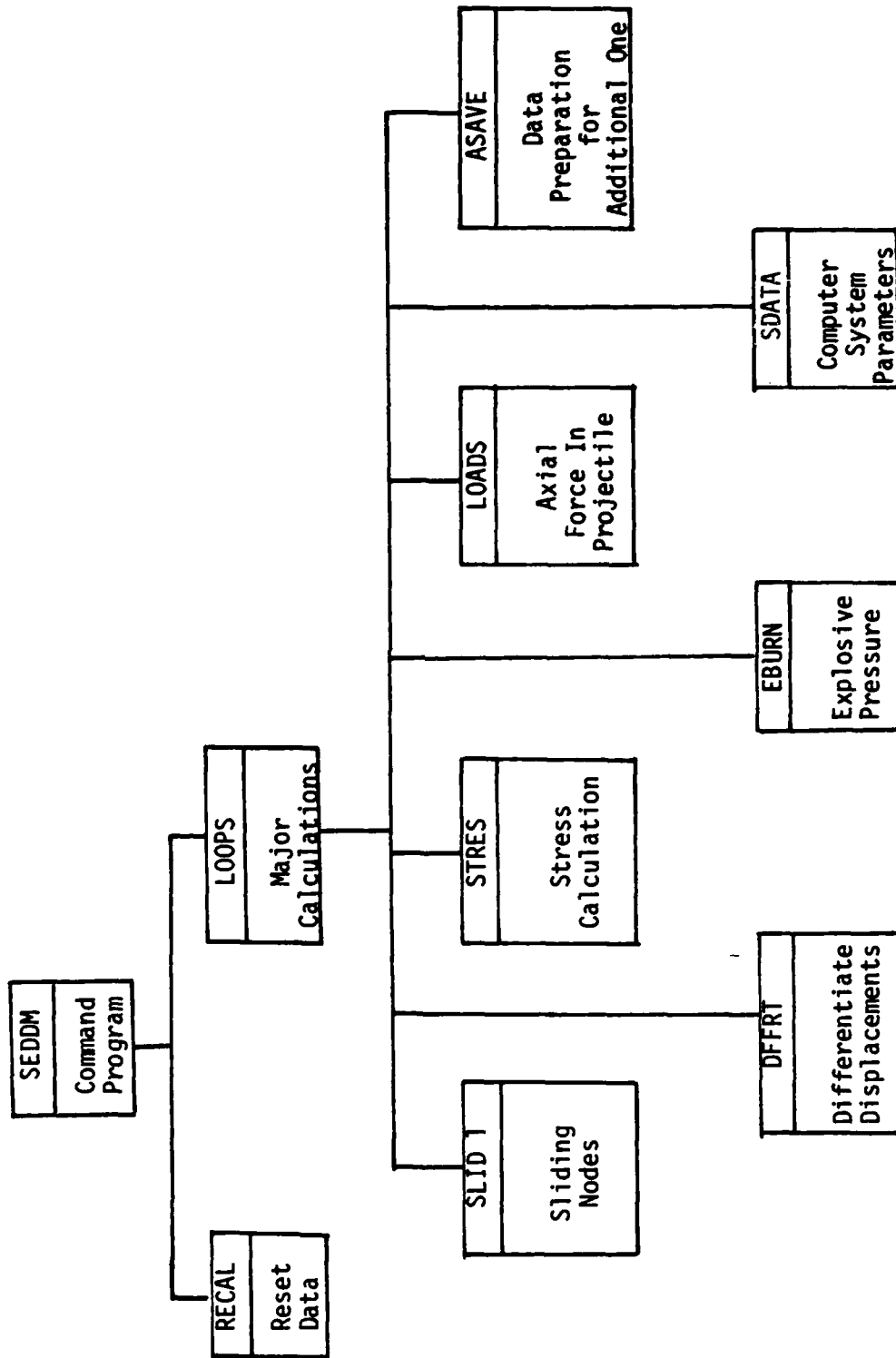
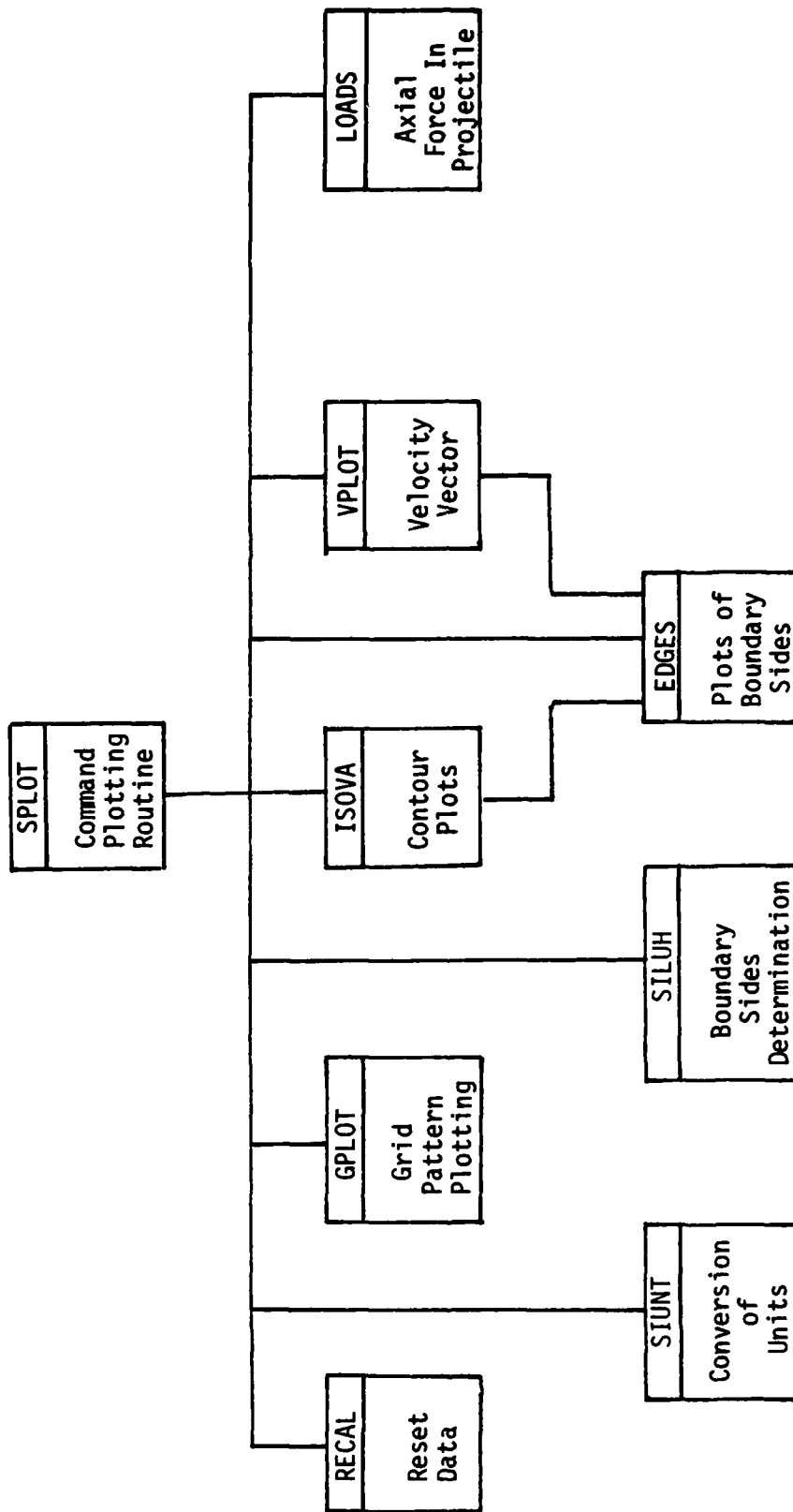


Table 3. Flow Chart of SPLOT: Postprocessing



The accuracy of the predictions can be improved by making the element size smaller and by increasing the total number of elements. This adds complexity to the solution as the computer program for analyzing the progressive damage of the projectile and target already involves many steps where the stresses, displacements, and energy densities must be repeated many times for each element and each time step. Refer to Tables 4, 5 and 6 for a more detailed account of the computing procedures involved in INITI, SEDDM and SPLOT. The description of the deck cards can be found in [16].

#### IMPACT OF CYLINDRICAL PROJECTILE ON PLATE TARGET: MODEL I AND II

The impact of a cylindrically-shaped projectile on a finite thickness plate will be analyzed by application of the axisymmetric dynamic code that incorporates the strain energy density material damage criterion as presented earlier. This program shall be henceforth referred to as the "Axisymmetric Dynamic Energy Density (ADED) Code". The impact velocity will be increased incrementally for a metal projectile hitting a metal target until perforation occurs. A salient feature of ADED is that material properties covering strain rates from  $10^{-4}\text{sec}^{-1}$  to  $10^6\text{sec}^{-1}$  are provided in the computer data bank.

This covers the full range of energy dissipation rates that produce failure by permanent deformation, spallation and/or fracture in the form of plugging. No a priori assumptions are made on the mode of failure. Unlike all the other codes\*

---

\*The most serious limitations in all these codes result from the application of the von Mises yield criterion and the assumption that the uniaxial stress and strain data coincide with the effective stress and effective strain used in the theory of plasticity. Moreover, they cannot consistently account for the variations in strain rate effects from element to element.

Table 4. Block Diagram for Computing Procedures of INITI

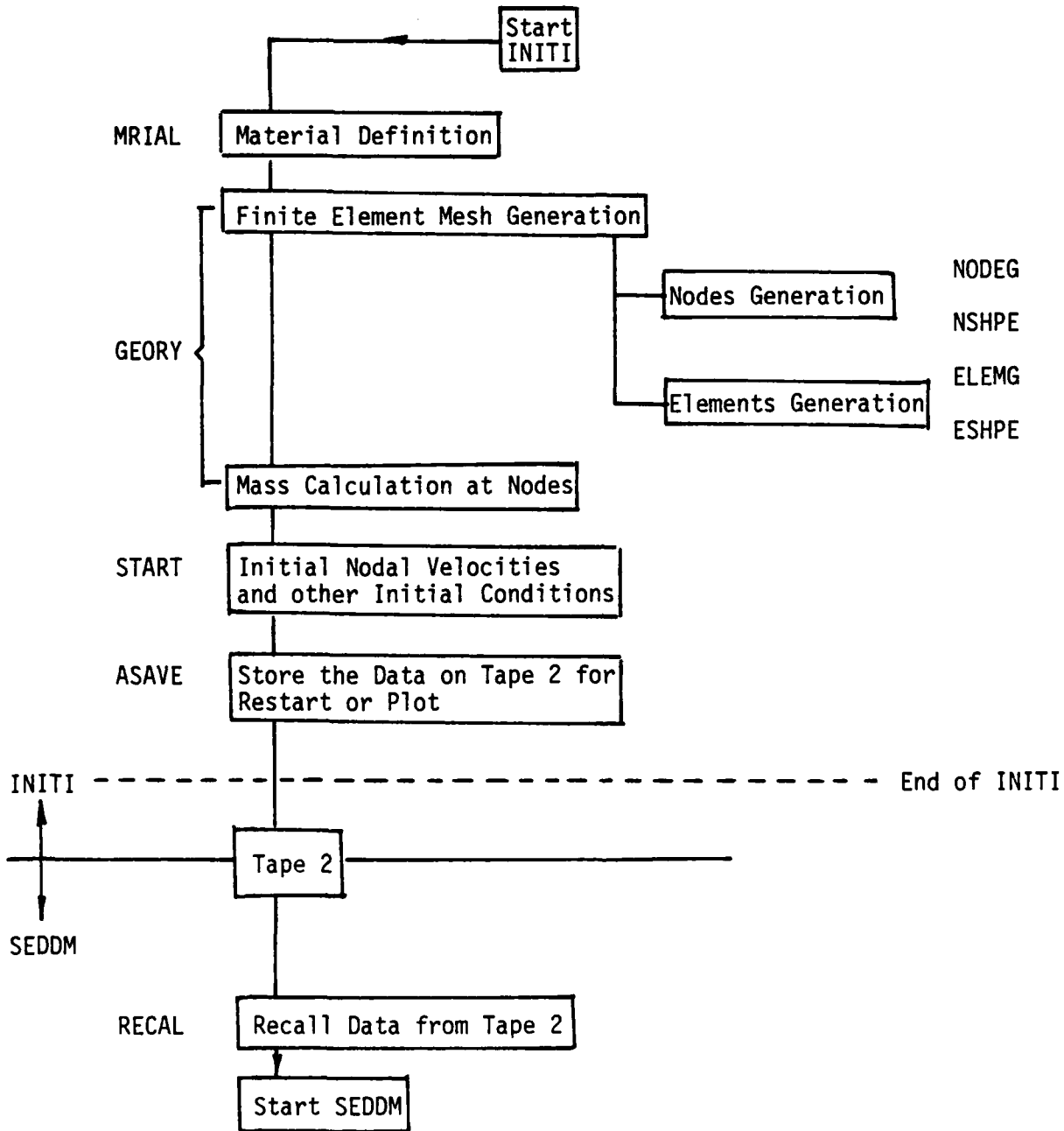


Table 5. Block Diagram for Computing Procedure of SEDDM

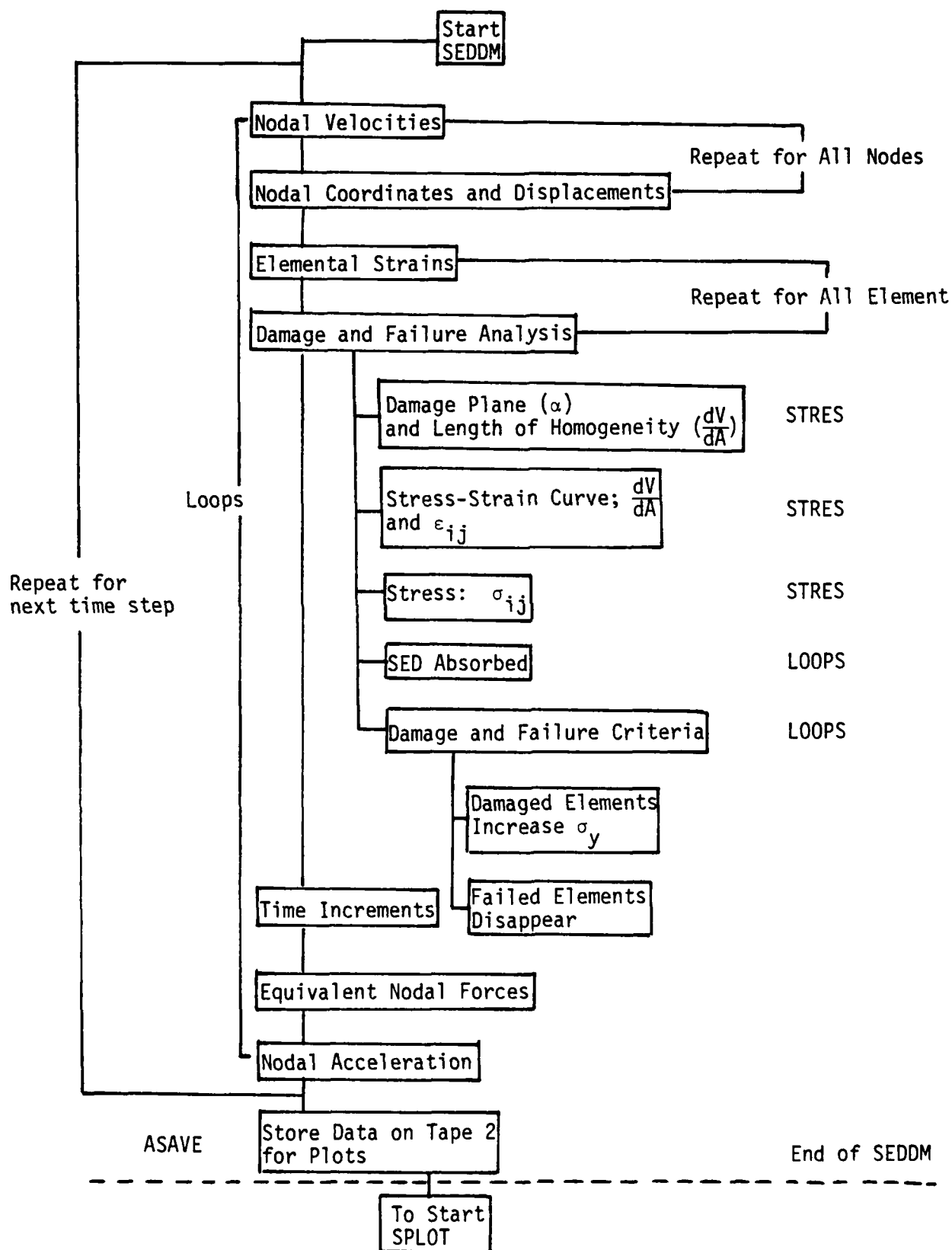
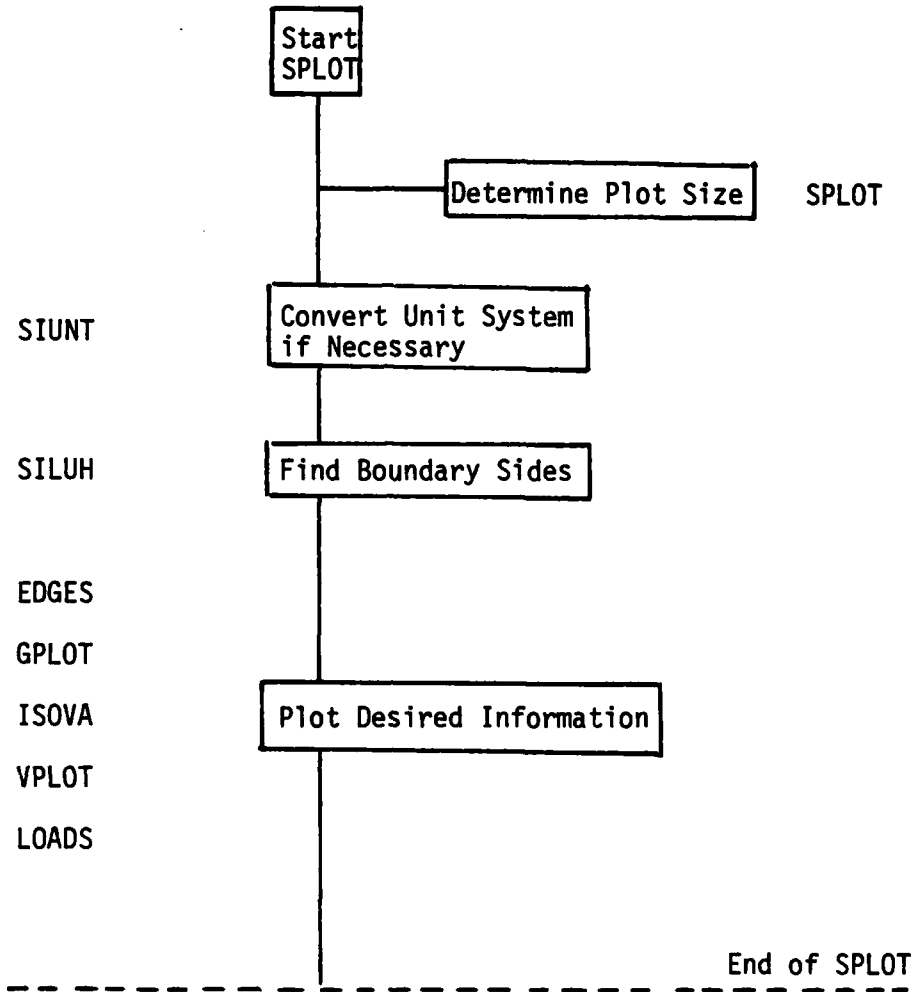


Table 6. Block Diagram for Computing Procedure of SPLOT



[1-3], ADED possesses the additional ability to simulate relative damage of all elements. This allows the projectile and target material to have a continuous range of weakened states from the undamaged to the completely failed state. Refer to [16] for a description of the ADED Code where the card deck is explained in detail.

*Projectile-Target System.* Consider the projectile-target system illustrated in Figure 8 where both the projectile and target are made of 4340 steel with a Rockwell Hardness number of 52. Referring to Figure 8, the geometry is such that  $L_p/D_p = 2.0$ ,  $h_t = D_p$  and  $D_t = 10D_p$ . These proportions coincide with the example problem in [9]. The finite element grid pattern is shown in Figure 9 where 160 and 455 elements are used to model the projectile and target, respectively.

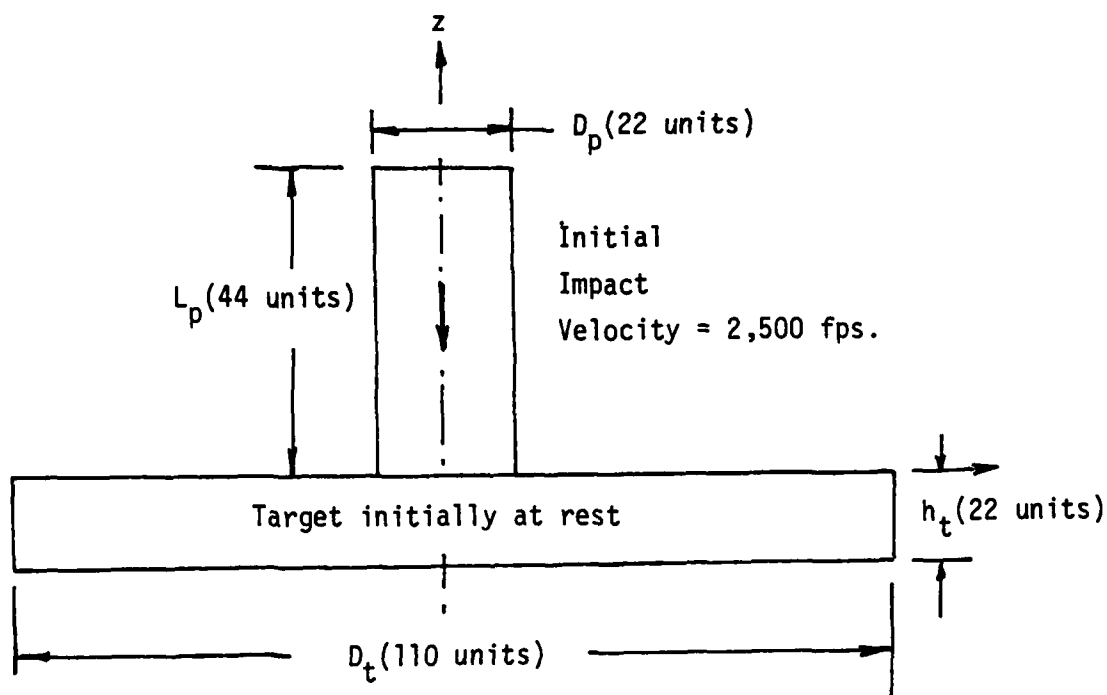


Figure 8. Schematic of projectile-target System: Axially symmetric impact.

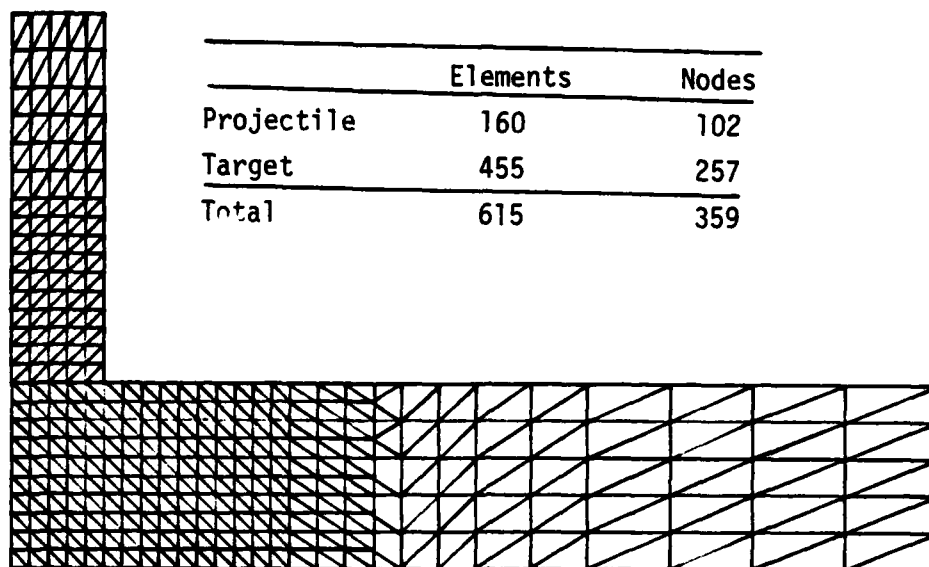


Figure 9. Finite element grid pattern:  
One-Half Symmetry.

*Material Properties.* The material data bank in the ADED Code consists of eleven (11) nonlinear stress and strain curves modeled by the relation

$$\sigma = E\epsilon - \beta\sigma_y \left[ \left( \frac{\epsilon}{\epsilon_y} \right)^\gamma - 1 \right], \quad \sigma > \sigma_y \quad (46)$$

with  $\beta = 0.7879$ ,  $\gamma = 1.053$  and  $E = 30 \times 10^6$  psi. The yield strength  $\sigma_y$  and corresponding final strain  $\epsilon_f$  are given in Figure 10. The curves labelled 1,2,--,10 correspond, respectively, to strain rates of  $10^{-4}$ ,  $10^{-3}$ ,---,  $10^6$  sec $^{-1}$ . The ADED Code traces out the stress and strain history for each element and continuous damage is monitored according to the strain energy density criterion, using equations (42) and (44). Refer to Figure 11 for the relation between the yield strength  $\sigma_y$  and critical strain energy density function  $(dW/dV)_c$  of 4340 steel.

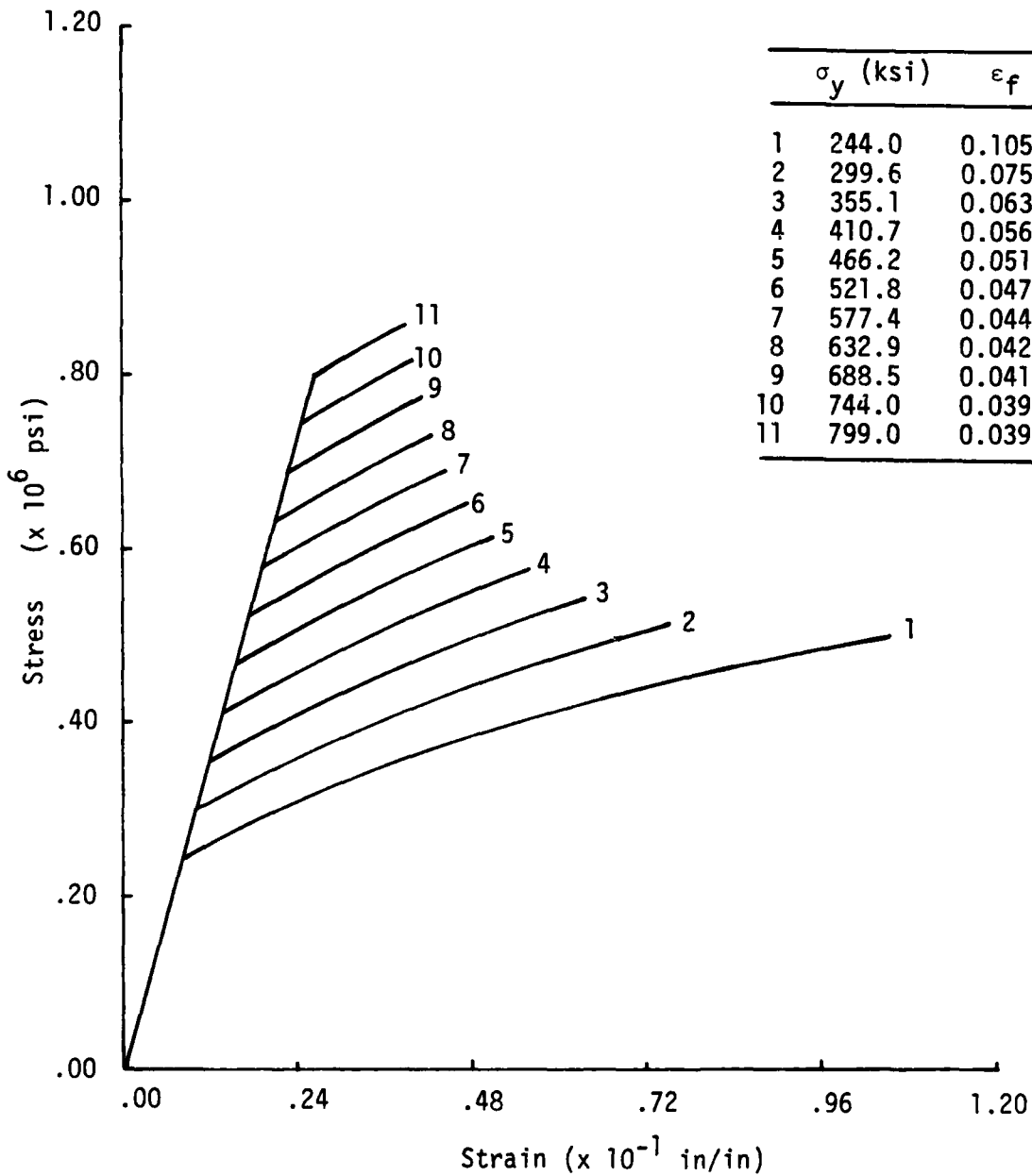


Figure 10. True stress and true strain curve in ADED data bank for Model I.

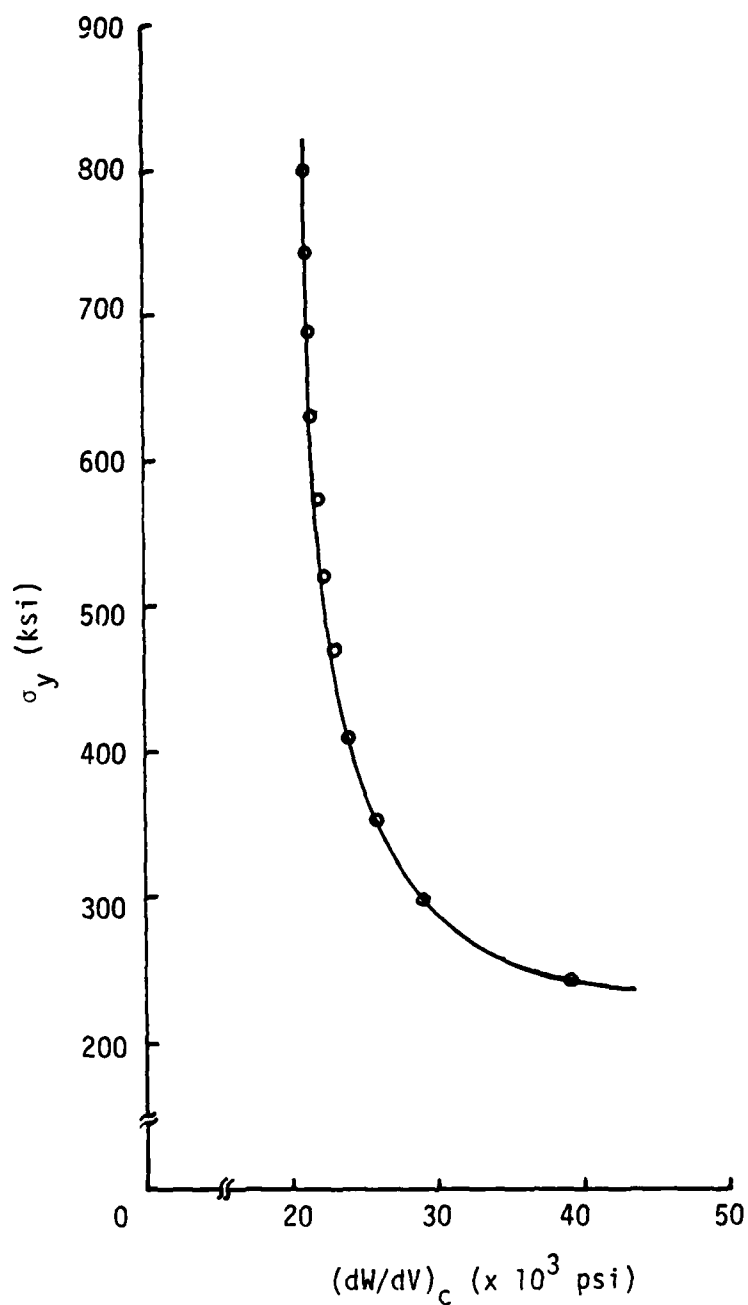


Figure 11. Relation between yield strength and critical strain energy density function for hardened 4340 steel (Model I).

*Model I.* In this model, the failed elements are considered to be fractured as they reach or surpass the condition in equation (44) and are removed completely from the analysis. Figures 12 and 13 show the numbering system for the nodal points and elements. The results will be described in a series of time steps labelled 1,2, etc. and presented only for those time steps that exhibit significant damage and/or failure. The details of the computer program are given in [16] together with additional numerical results.

Figure 14 illustrates the projectile-target damage pattern after  $0.03053\mu\text{sec}$  of impact. The corner element No. 160 on the projectile has already failed and been removed from the output. Two regions are identified. The dotted elements nearest to the contact are stressed while the remaining areas are unstressed as the waves have not propagated that far. At  $t = 0.04641\mu\text{sec}$ , Figure 15, the two adjacent rows of elements with numbers 151, 152,---,159 and 201, 202,---209 that were in contact have failed except for the corner elements No. 210. More elements are now being stressed and the effect of wave propagation can be clearly seen in Figure 16 after  $0.07715\mu\text{sec}$ . The elements are seen to fail quickly after impact because of the high strain rates and relatively low fracture toughness of the target.

The values of  $\alpha$  locating the damage plane as defined in Figure 5(b) are given in Table 7 for elements near the contact as  $\alpha$  increases from 0 to  $0.4855\mu\text{sec}$ . The direction of the damage plane for elements No. 151, 152,---,160 at initial contact did not change appreciably up to failure. For elements No. 210 and 211  $\alpha$  increased slightly i.e., the axes  $\xi$  and  $\eta$  approach towards  $x$  and  $y$  as failure is

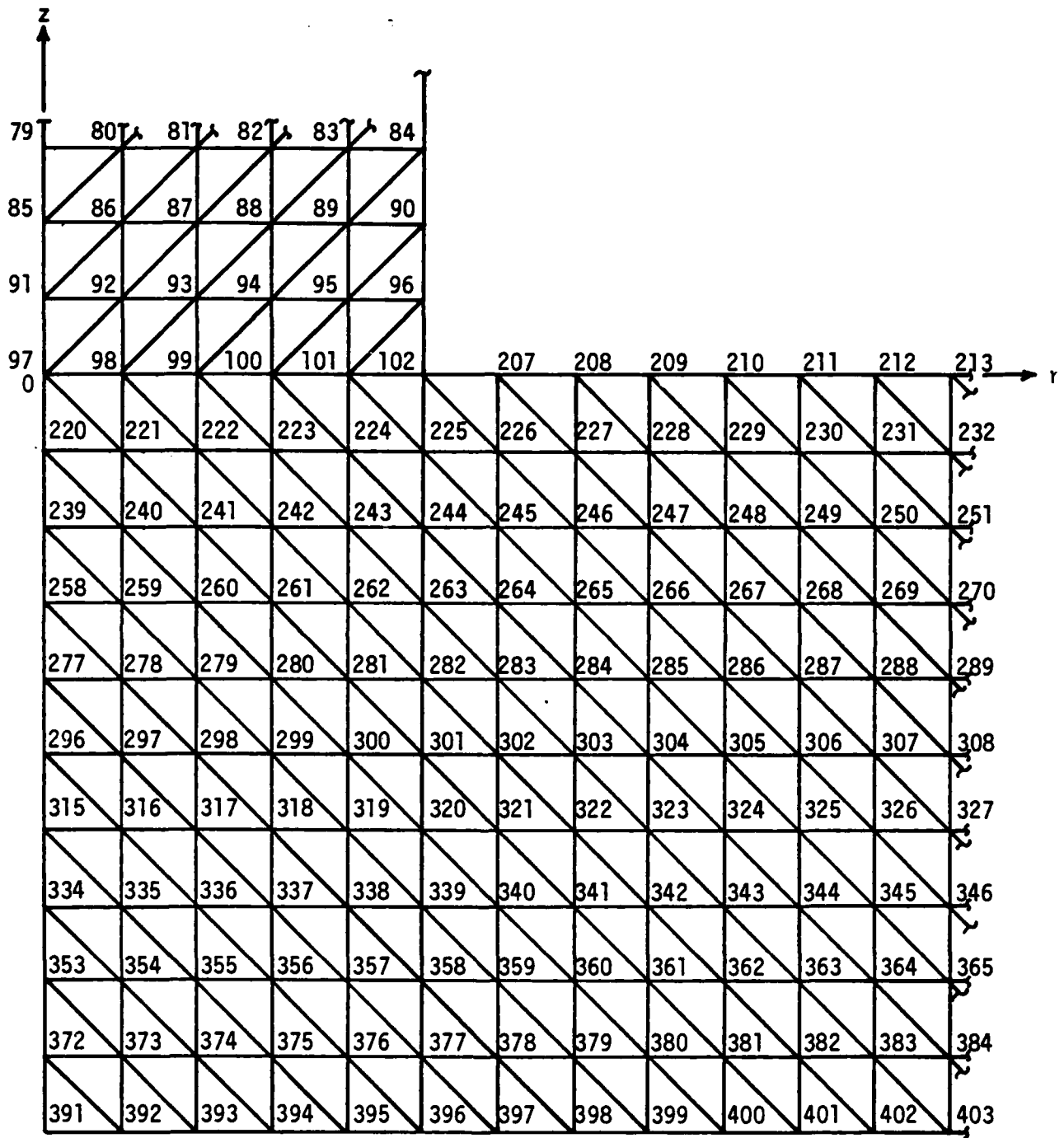


Figure 12. Numbering system of nodal points.



Time = 0.03053 $\mu$ sec.

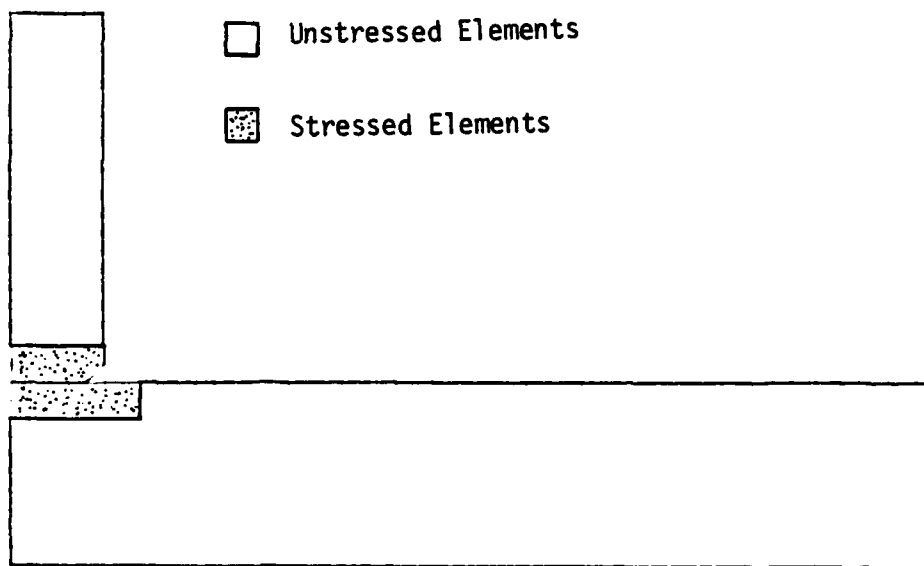


Figure 14. Projectile-target damage pattern after 0.03053 $\mu$ sec (Model I).

Time = 0.04641 $\mu$ sec.

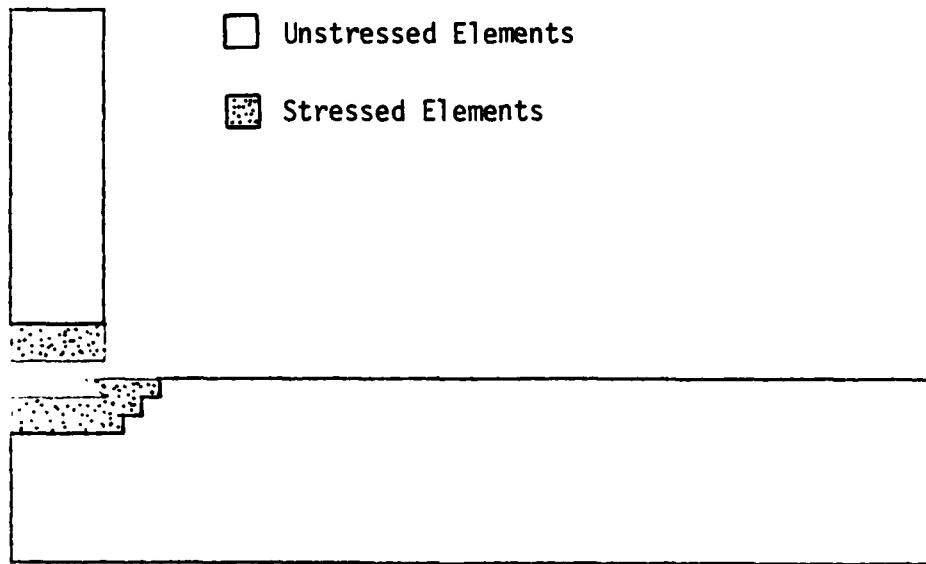


Figure 15. Projectile-target damage pattern after 0.04641 $\mu$ sec (Model I).

Time = 0.07715 $\mu$ sec.

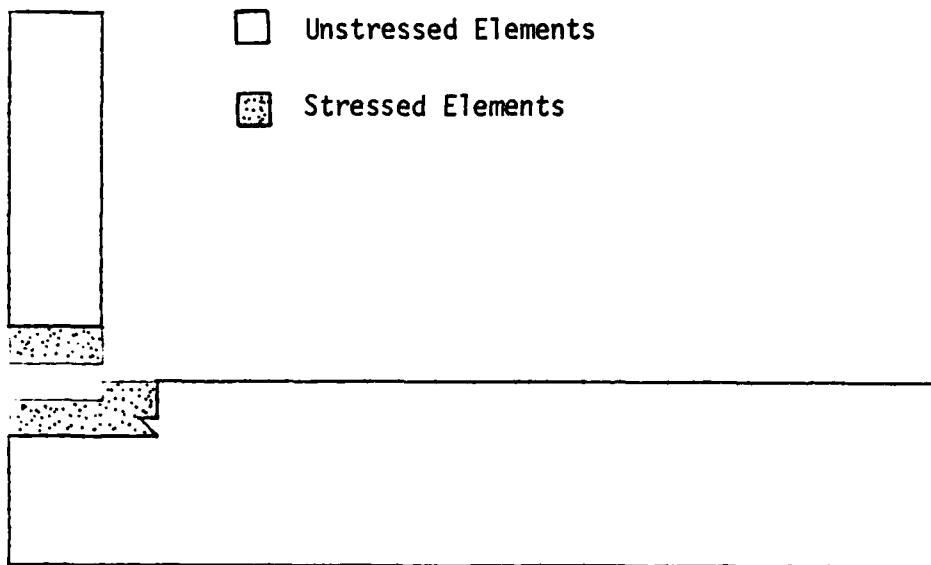


Figure 16. Projectile-target damage pattern after 0.07715 $\mu$ sec (Model I).

Table 7. Angle  $\alpha$  of Damaged Plane for  
Element Near Contact for Model I.

Time ( $\mu$ sec)	Element No.					
	160	151	152 to 156	210	211	248
0.0050	-35.33°	-45.00°	-45.00°	-20.16°	-45.00°	-
0.0105	-35.34°	-44.99°	-45.00°	-20.19°	-44.97°	0.61°
0.0166	-35.35°	-44.98°	-45.00°	-20.25°	-44.91°	0.65°
0.0232	-35.37°	-44.96°	-44.99°	-20.34°	-44.80°	0.62°
0.0305	-35.41°	-44.92°	-44.99°	-20.48°	-44.65°	0.58°
0.0331	<u>-35.42°</u>	-44.91°	-44.99°	-20.51°	-44.62°	0.61°
0.0464	(failed)	<u>-44.81°</u>	<u>-44.99°</u>	-20.22°	-44.28°	-2.25°
0.0611		(failed)	(failed)	-19.50°	-43.90°	-2.62°
0.0772				<u>-18.17°</u>	-43.40°	-0.19°
0.0949				(failed)	<u>-42.71°</u>	1.13°
0.1144					(failed)	0.87°
0.1358						0.65°
0.1594						-1.14°
0.1853						-3.88°
0.2138						-8.18°
0.2452						-15.26°
0.2798						-26.73°
0.3177						-41.41°
0.3595						36.22°
0.4015						26.30°
0.4435						22.60°
0.4855						<u>17.40°</u> (failed)

approached. Oscillation in the orientation of the damage plane can be observed in elements No. 248 before it failed. Table 8 gives the values of the equivalent uniaxial stress and strain in the  $\epsilon$ - and  $\eta$ -direction.

Table 8. Equivalent Uniaxial Stress and Strain in Elements Near Contact on Damaged Plane for Model I.

Time ( $\mu$ sec)	Element No.					
	160		151		210	
	$\epsilon = \epsilon_{\xi} = \epsilon_{\eta}$ ( $\mu$ in/in)	$\sigma = \sigma_{\xi} = \sigma_{\eta}$ ksi	$\epsilon = \epsilon_{\xi} = \epsilon_{\eta}$ ( $\mu$ in/in)	$\sigma = \sigma_{\xi} = \sigma_{\eta}$ ksi	$\epsilon = \epsilon_{\xi} = \epsilon_{\eta}$ ( $\mu$ in/in)	$\sigma = \sigma_{\xi} = \sigma_{\eta}$ ksi
0.0050	-2641	-79.2	-1710	-57.3	-784	-23.5
0.0105	-5553	-166.6	-3596	-107.9	-1647	-49.4
0.0166	-8756	-262.7	-5673	-170.2	-2596	-77.9
0.0232	-12260	-367.8	-7955	-238.7	-3642	-109.3
0.0305	-16070	-482.2	-10460	-313.7	-4790	-143.7
0.0331	(failed)		-11360	-340.8	-5199	-156.0
0.0464			(failed)		-7145	-214.3
0.0611					-9040	-271.2
0.0772					-10630	-317.0
					(failed)	

The corresponding stress and strain components referred to the r- and z-axis can be obtained by Mohr circle transformation. Exhibited graphically in Figure 17 is the dynamic stress  $\sigma_{\xi}$  or  $\sigma_{\eta}$  as a function of time. The normal stresses in element No. 160 rise more sharply with time and it fails first. Elements No. 151 and 152 in the projectile and elements No. 210 and 211 in the target failed subsequently. The corresponding stresses did not rise as sharply with time. Nonlinear variation is not observed as the elements failed very quickly on account of low fracture toughness. These results reflect the difference in

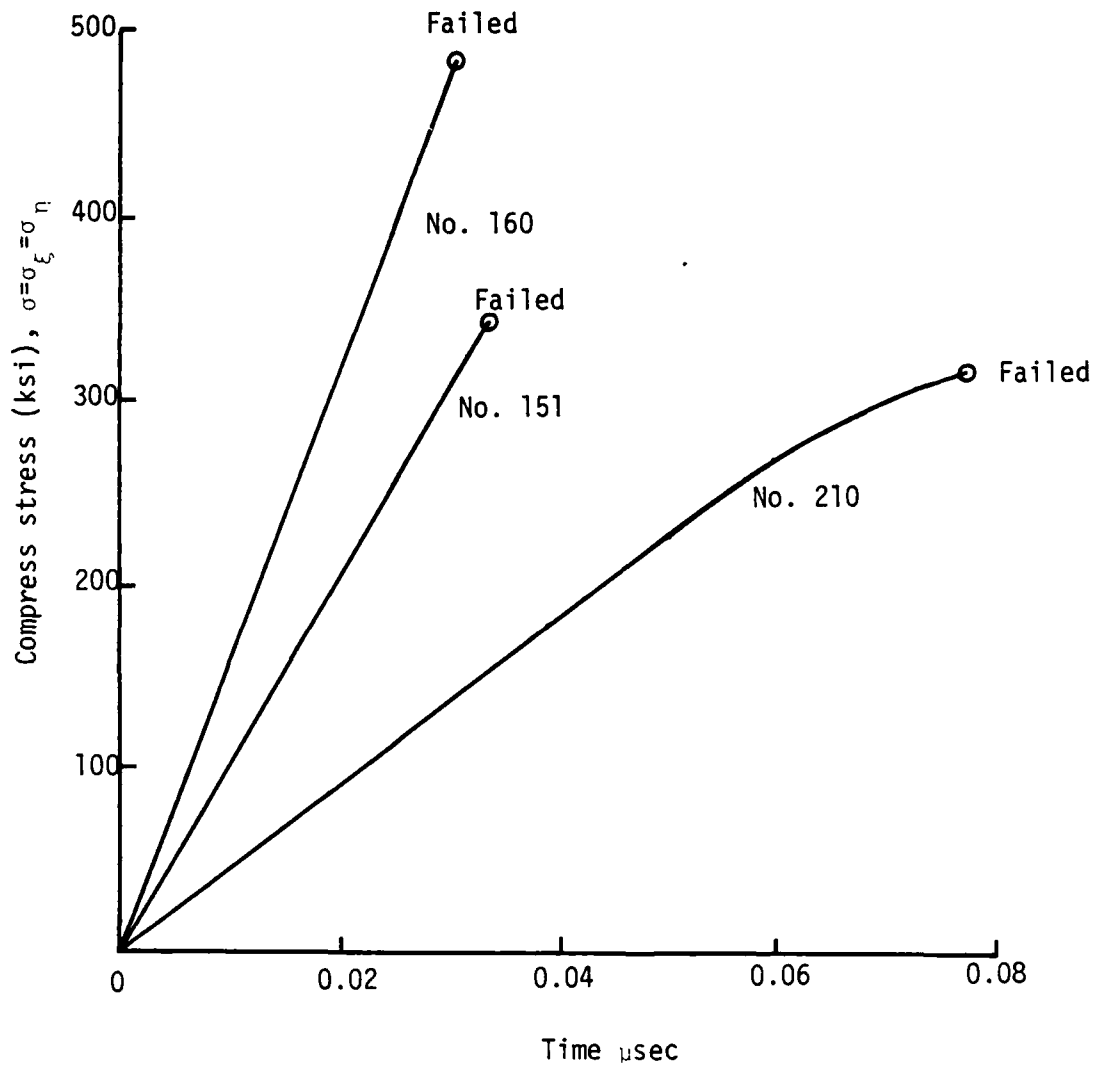


Figure 17. Equivalent uniaxial stress-time curve for elements failed at contact in Model I.

Time = 0.09487 $\mu$ sec

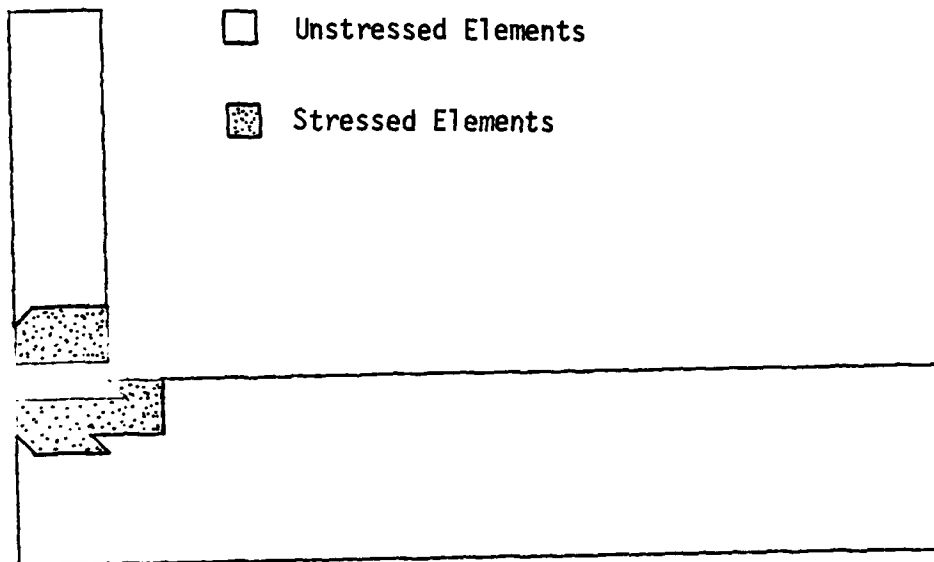


Figure 18. Projectile target damage pattern after 0.09487 $\mu$ sec (Model I).

Time = 0.44352 $\mu$ sec.

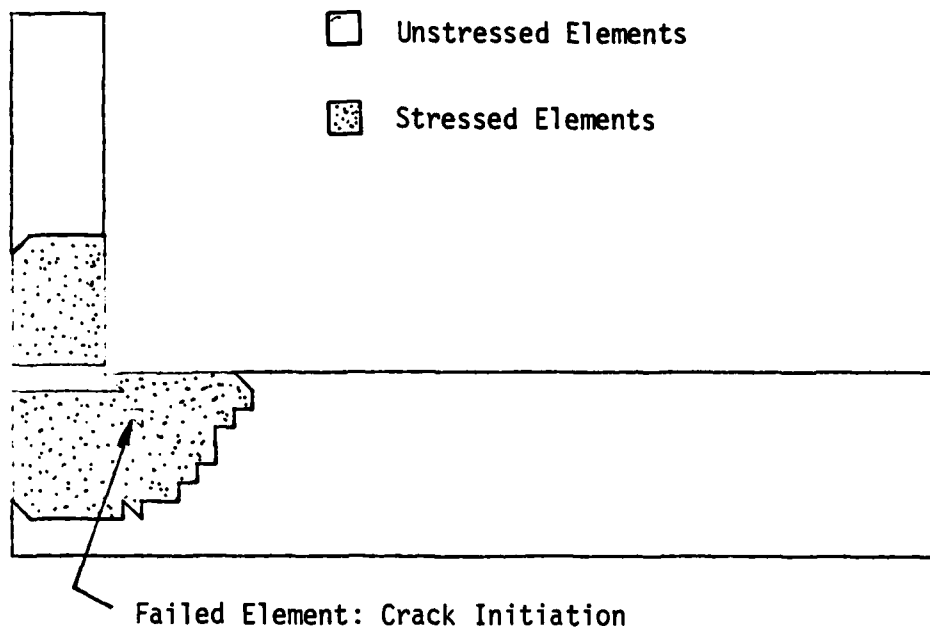


Figure 19. Projectile-target damage pattern after 0.44352 $\mu$ sec (Model I).

Angle of Damage Plane at  
 $t = 0.44352\mu\text{sec}.$

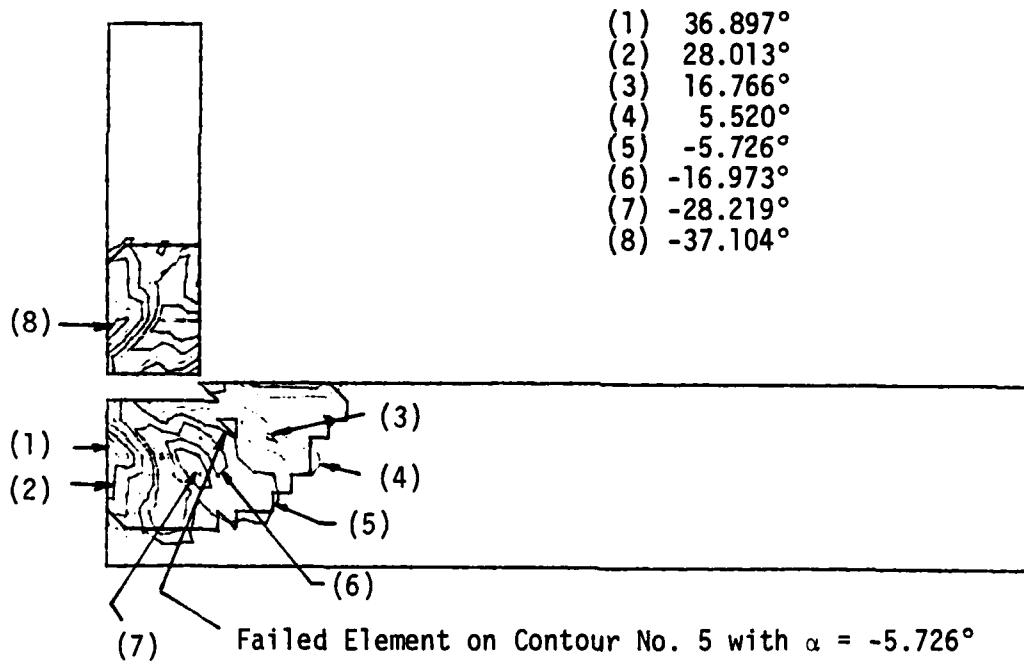


Figure 20. Contours of constant damage plane orientation after  $0.44352\mu\text{sec}$  (Model I).

Table 9. Values of  $dV/dA$  (in) for Some  
Typical Elements Near Contact Area  
(Model I)

Time ( $\mu$ sec)	Element No.					
	160	151	152 to 156	210	211	248
0.0050	2.451	2.828	2.828	2.131	2.828	-
0.0105	2.452	2.828	2.828	2.131	2.827	0.142
0.0166	2.452	2.827	2.828	2.132	2.824	0.104
0.0232	2.453	2.825	2.827	2.134	2.820	0.033
0.0305	2.454	2.823	2.825	2.136	2.813	0.079
0.0331	<u>2.454</u>	<u>2.822</u>	2.825	2.137	2.812	0.074
0.0464	(failed)	(failed)	<u>2.826</u>	2.132	2.800	1.074
0.0611			(failed)	2.122	2.784	1.267
0.0772				<u>2.105</u>	2.763	3.742
0.0949				(failed)	<u>2.734</u>	2.519
0.1144					(failed)	2.464
0.1358						2.490
0.1594						2.531
0.1853						2.555
0.2138						2.552
0.2452						2.563
0.2798						2.705
0.3177						3.168
0.3595						2.934
0.4015						2.709
0.4435						2.599
0.4855						<u>2.497</u>
						(failed)

the stress and strain response of elements owing to different strain rates. This accounts for the nonuniform rate of energy dissipation from element to element and the sequence of the material damage and/or failure process.

As the projectile further advances up to  $t = 0.09487\mu\text{sec}$ , Figure 18 shows that element No. 211 being under element No. 212 has now failed. The waves have also propagated further towards the back side of the target. In Figure 19 at  $t = 0.44352\mu\text{sec}$  the interior element No. 286 is seen to fail as a result of  $dV/dA$  reaching 95.04 in which is much higher than the three neighboring elements with common adjacent sides. They are elements No. 249, 285 and 287 as shown in Figure 13 with the respective  $dV/dA$  values of 2.384 in, 2.379 in and 2.248 in. Refer to Table 9 for some typical values of  $dV/dA$  referring to elements near the contact that have failed. It is of interest to note that the value of  $dW/dV = 941.22$  psi in the unfailed element No. 249 is higher than  $dW/dV = 359.78$  psi in element No. 286 which has failed. This is due to the high strain rate effect as  $dV/dA$  is proportional to the slope of the true stress and true strain curve. The  $dW/dA$  criterion, therefore, includes both deformation rate through  $dV/dA$  and energy dissipation rate via  $dW/dV$ . Hence, failure can occur at locations where  $dW/dV$  may be low but  $dV/dA$  can be high.

Figure 20 plots contours of the damage plane orientation with constant  $\alpha$ . The failed element No. 286 in Figure 20 corresponds to contour No. 5 with  $\alpha = 05.726^\circ$ . This implies that the  $\xi$  and  $\eta$  axes almost coincide with the  $x$  and  $y$  axes along which uniaxial data are taken. It is essential to recognize that the direction of the damage plane within an element need not coincide exactly with the path of fracture\* or plug formation. That

---

\* It is common experience that the path of a macrocrack is usually assumed to follow the general formation of the randomly oriented microcracks. The zig-zag details are microscopic in scale. Their influence on the change in direction of the macrocrack is small and can be neglected in any macroscopic analysis.

Time = 0.48546 $\mu$ sec

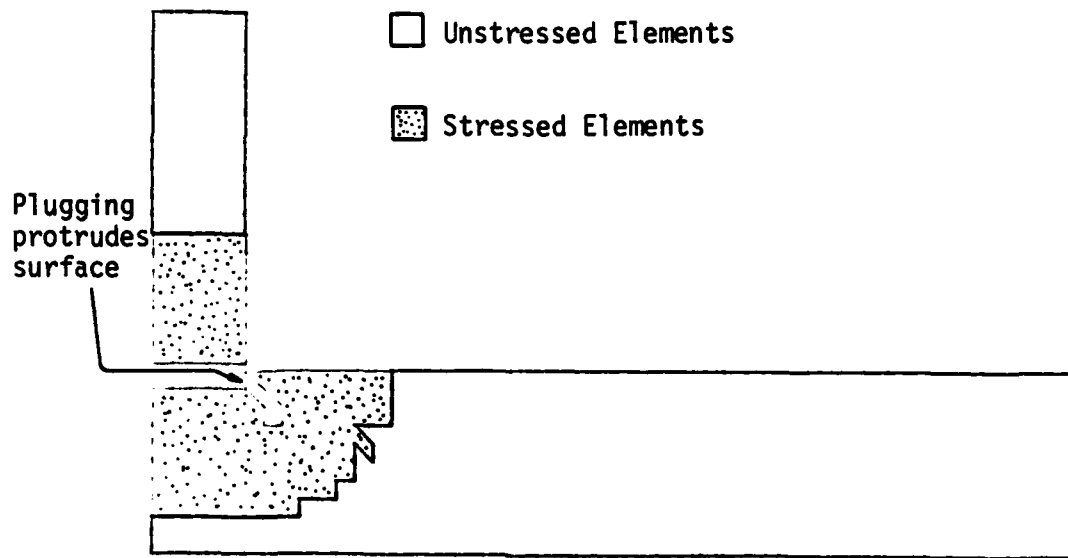


Figure 21. Projectile-target damage pattern after 0.48546 $\mu$ sec (Model I).

Orientation of Damage Plane at  
 $t = 0.48546\mu\text{sec}$ .

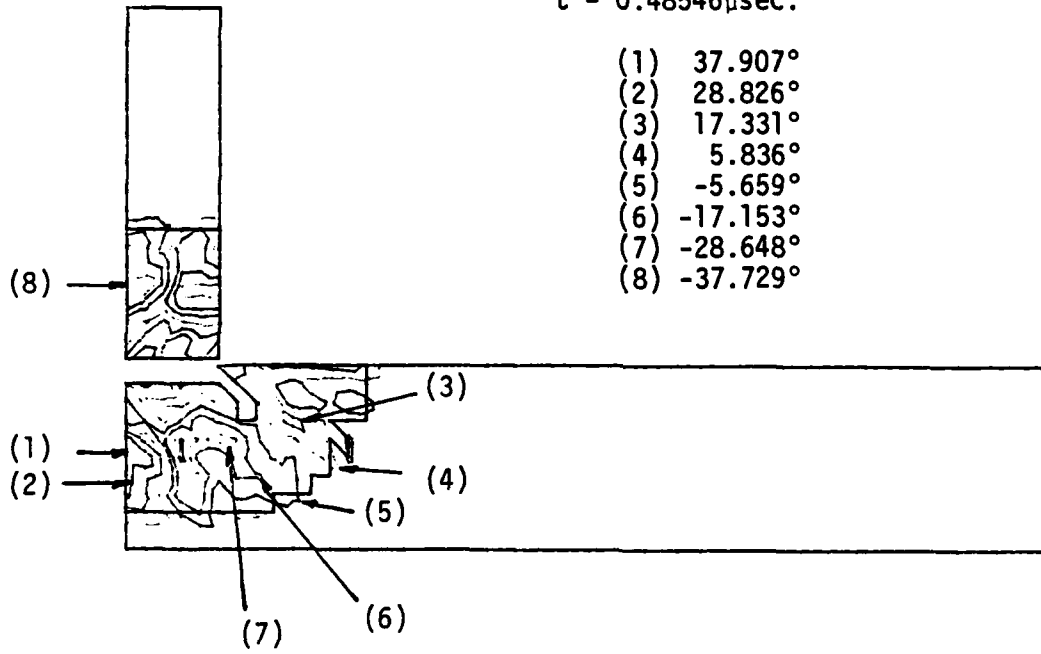


Figure 22. Constant  $\alpha$  contour after  $0.48546\mu\text{sec}$   
(Model I).

is the local failure plane and global fracture path do not necessarily coincide. It is the loci of the failed elements that form the path of fracture. Since the shape of the triangular element is chosen arbitrarily, it cannot be used for the shape of the cavity or crack. The condition as stated in equation (44) corresponds to failure say permanent deformation\* prior to fracture. A small cavity or crack\*\* is thus assumed to be formed at element No. 286. As mentioned earlier, the orientation of this small crack does not have to coincide with the path of fracture which is assumed to follow the contour with constant  $\alpha$  that is oriented almost vertically through elements No. 285 and 322 and sideways in the direction of elements No. 248 and 249. The stress state in these neighboring elements are therefore intensified by approximately twenty (20) times in accordance with the well known factor  $2a/b$  where  $a/b$  is the geometric aspect ratio of a narrow elliptical cavity or crack. Once an internal cavity or crack is formed, fracture continues to occur quickly. As stress waves continue to propagate in the projectile and target, Figure 21 shows that the elements No. 248, 249 and 285 are failed at  $t = 0.48546\mu\text{sec}$ . The fracture path protrudes the front side of the target plate. The projectile has momentarily lost contact with the target. Since damage and failure is constantly changing process, the orientation of the damage plane for each element also changes accordingly.

---

\* The common notion of yielding is no longer applicable in the newly proposed damage model although the quantity yield strength is still being used. It is more appropriate to refer to damage by permanent deformation as the concept of yield surface is not needed.

\*\* A crack is defined to be an elongated cavity with a major to minor axis ratio of ten, say  $2a/b = 10$ . The longest and smallest dimension should differ at least by one order of magnitude.

Time = 0.52734 $\mu$ sec

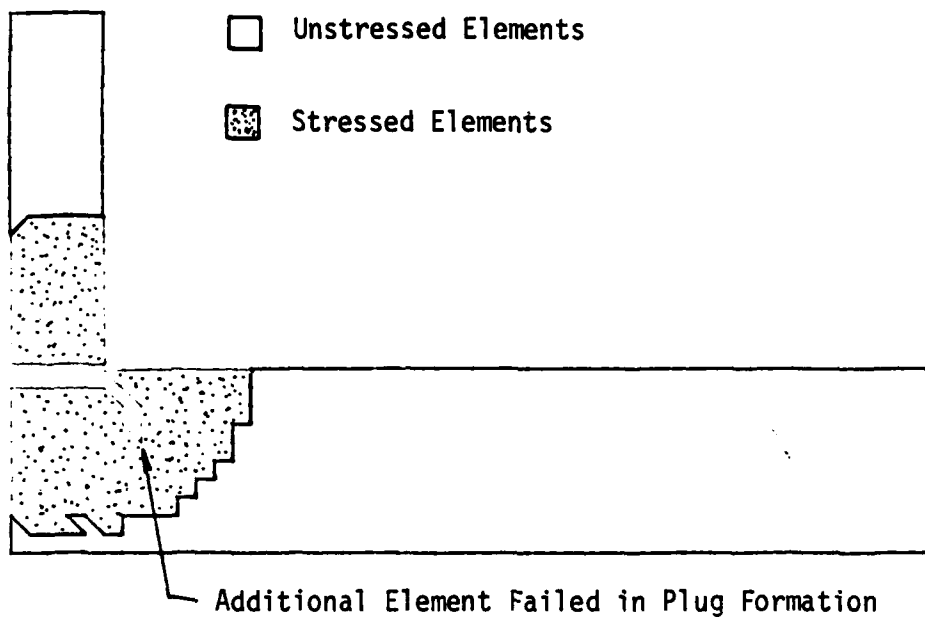


Figure 23. Projectile-target damage pattern after 0.52734 $\mu$ sec (Model I).

Damage Orientation Plane at  
 $t = 0.52734 \mu\text{sec}$ .

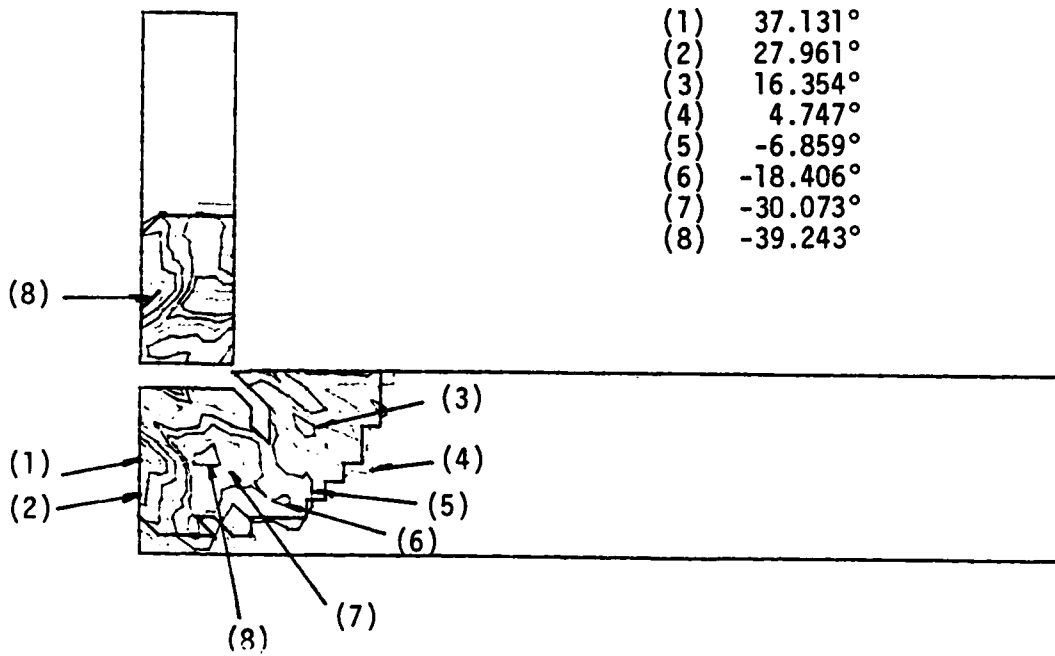


Figure 24. Constant  $\alpha$  contour after  $0.52734 \mu\text{sec}$   
(Model I).

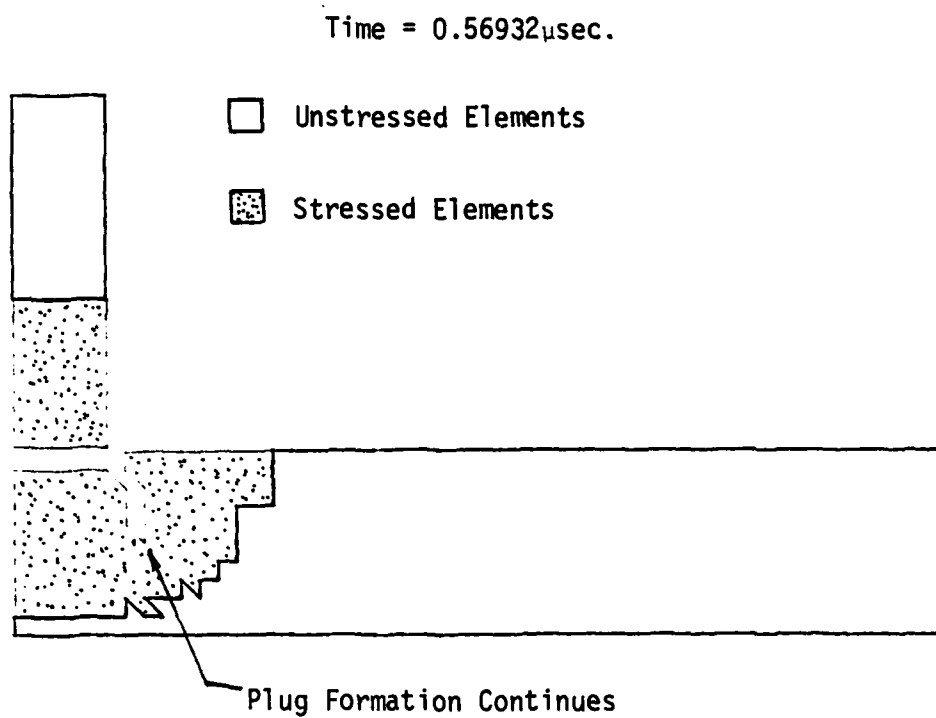


Figure 25. Projectile-target damage pattern after 0.56932 $\mu$ sec (Model I).

Orientation of Damage Plane at  
 $t = 0.56932 \mu\text{sec}$ .

- (1)  $38.671^\circ$
- (2)  $29.343^\circ$
- (3)  $17.535^\circ$
- (4)  $5.727^\circ$
- (5)  $-6.080^\circ$
- (6)  $-17.888^\circ$
- (7)  $-29.696^\circ$
- (8)  $-39.024^\circ$

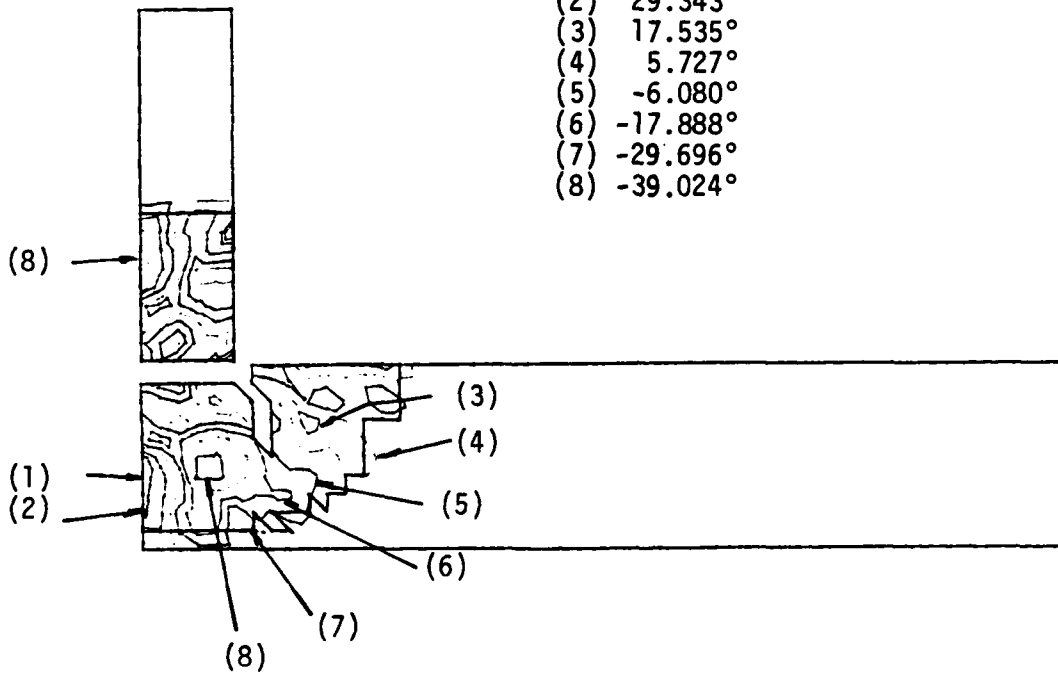


Figure 26. Constant  $\alpha$  contours after  $0.56932 \mu\text{sec}$   
(Model I).

Time = 0.61136 $\mu$ sec.

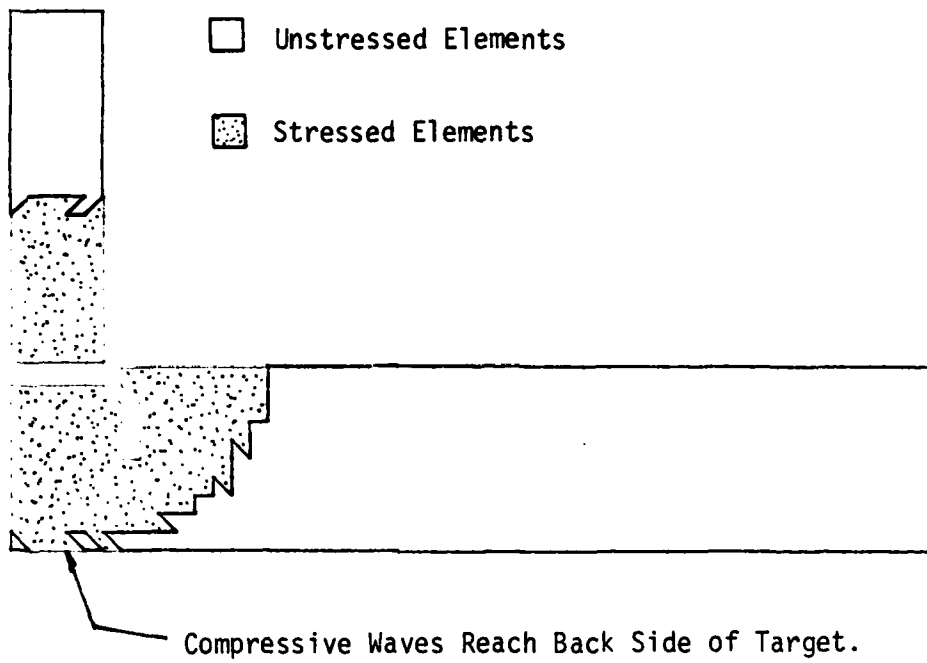


Figure 27. Projectile-target damage pattern after 0.61136 $\mu$ sec (Model I).

Orientation of Damage Plane at  
 $t = 0.61136 \mu\text{sec}$ .

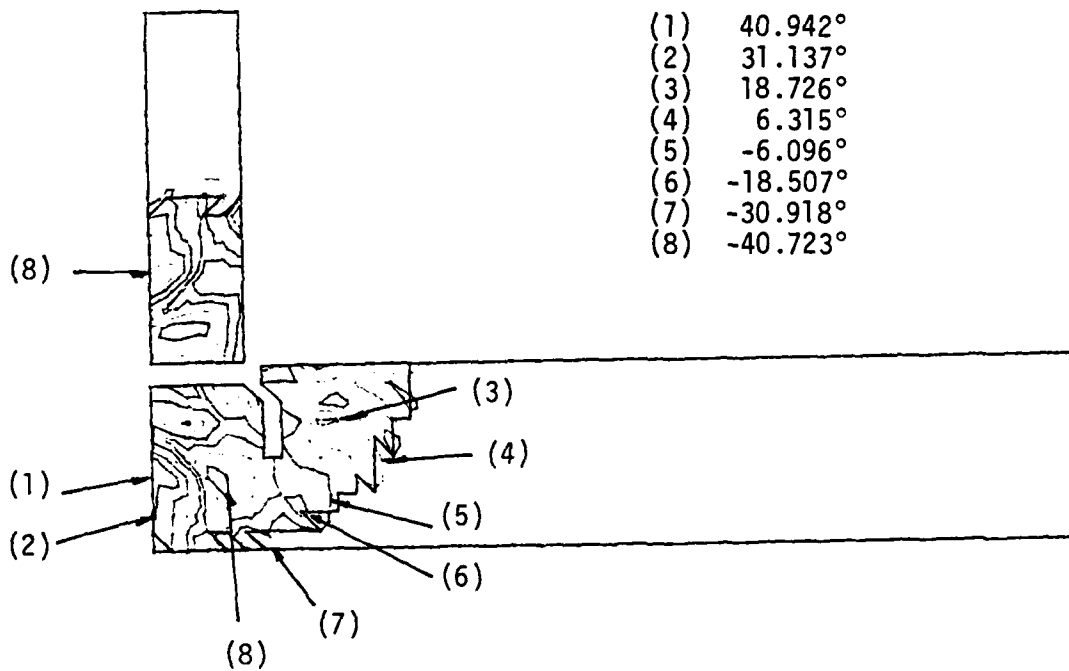


Figure 28. Constant  $\alpha$  contour after  $0.61136 \mu\text{sec}$   
(Model I).

The contours of constant  $\alpha$  in Figure 22 are seen to have altered as compared with those shown in Figure 20 of the previous time step with  $t = 0.44332\mu\text{sec}$ . The newly failed element No. 285 is now aligned along contour with  $\alpha = -5.66^\circ$ . Without further stress intensification, element No. 322 fails on the next time step with  $t = 0.52734\mu\text{sec}$ , Figure 23. Fracture is seen to extend directly in the negative z-direction. Shown in Figure 24 are the constant  $\alpha$  contours around the fracture path. This suggests the further intensification of elements No. 321 and 358 extending towards the back side of the target. The result is shown in Figure 25 where both elements No. 321 and 358 have failed together with the corner element No. 210. The corresponding constant  $\alpha$  contours are shown in Figure 26. Element No. 357 failed at  $0.61136\mu\text{sec}$  at which time the fracture path is exactly one-half way through the target plate. The compressive wave front has finally reached the back side of the plate and reflection begins. The elements with damage planes of  $\alpha \approx -18.51^\circ$  is almost directly under the fracture path, Figure 28. Element 394 remained intensified and failed at  $t = 0.6114\mu\text{sec}$ . As the target continues to fracture, the stresses in elements No. 393 and 430 are intensified and failed when  $t = 0.69586\mu\text{sec}$ . This is shown in Figure 29 together with the constant  $\alpha$  contours in Figure 30. As the plug is being formed elements No. 429 and 466 are further stress intensified. They failed at  $t = 0.73808\mu\text{sec}$  which is illustrated in Figure 31. Figure 32 gives the corresponding contours of constant  $\alpha$ . This process continues by failing the next two elements, No. 465 and 502 in Figure 33. The constant  $\alpha$  contour in this case is given in Figure 34. The failure of elements No. 465 and 502 occurred at  $t = 0.94774\mu\text{sec}$ . as plugging extends further, Figure 35. There is a deviation of the constant  $\alpha$  contour from the path of plugging. This

Time = 0.69586 $\mu$ sec.

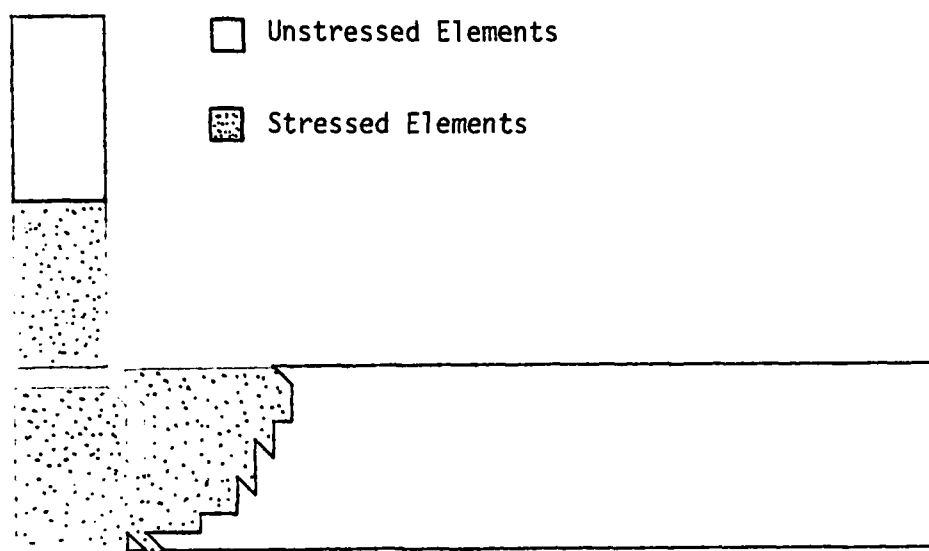


Figure 29. Projectile-target damage pattern after 0.69586 $\mu$ sec (Model I).

Orientation of Damage Plane at  
 $t = 0.69585\mu\text{sec}$ .

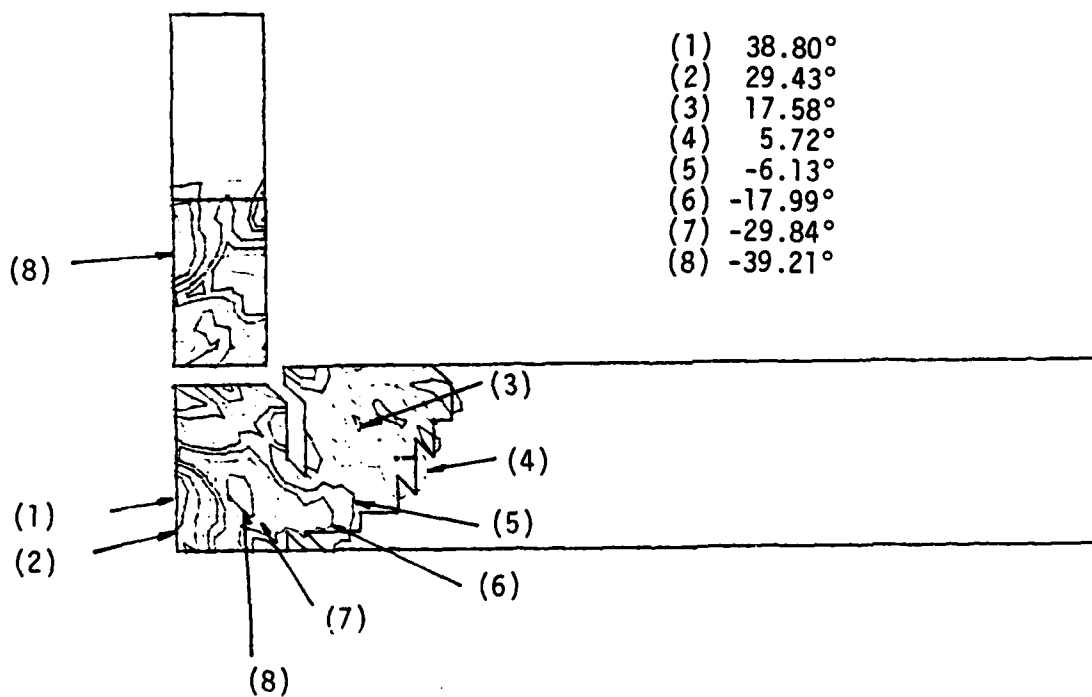


Figure 30. Constant  $\alpha$  contour after  $0.69585\mu\text{sec}$   
(Model I).

Time = 0.73808 $\mu$ sec.

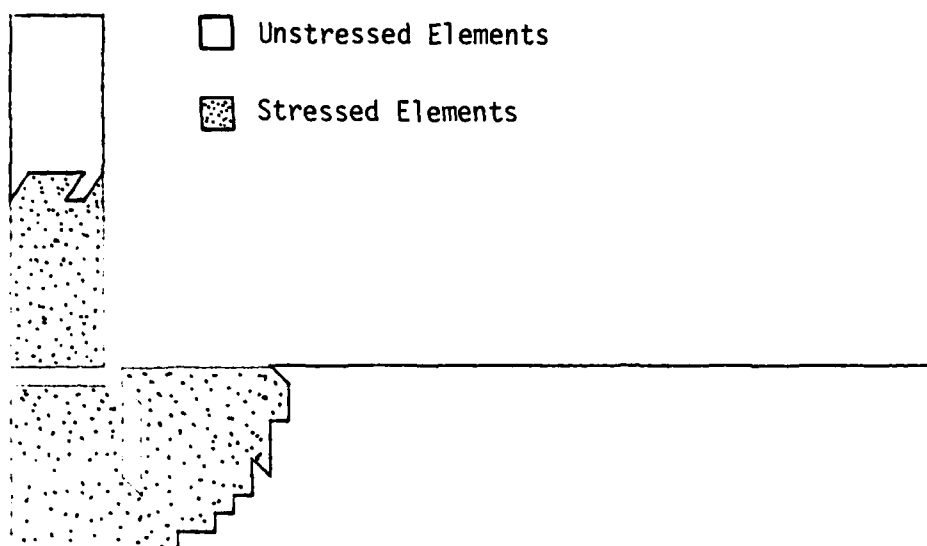


Figure 31. Projectile-target damage pattern after 0.73808 $\mu$ sec (Model I).

Orientation of Damage Plane at  
 $t = 0.73808\mu\text{sec}$ .

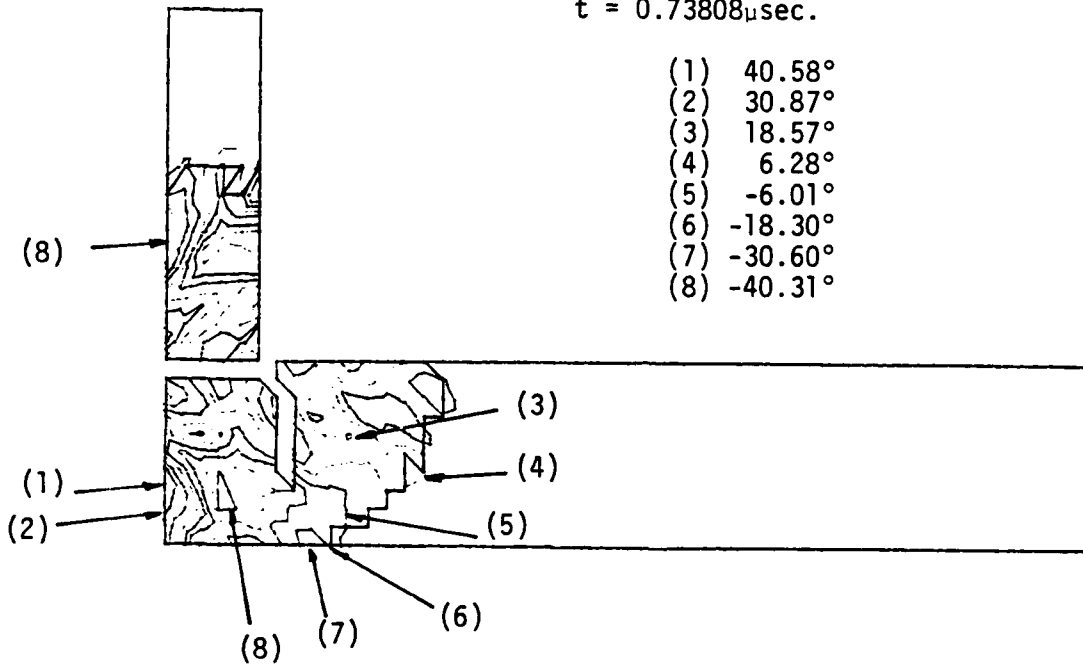


Figure 32. Constant  $\alpha$  contour after  $0.73808\mu\text{sec}$   
(Model I).

Time = 0.86418 $\mu$ sec.

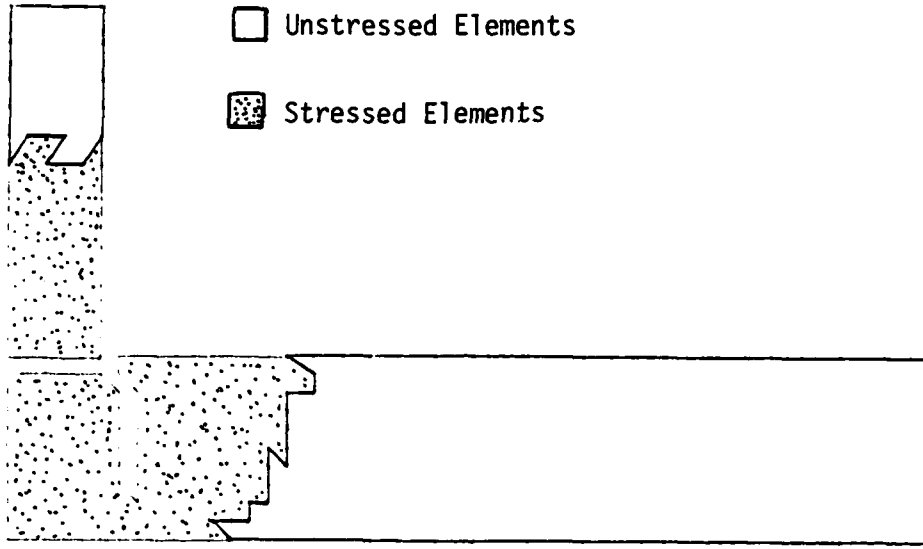


Figure 33. Projectile-target damage pattern after 0.86418 $\mu$ sec (Model I).

Orientation of Damage Plane at  
 $t = 0.86412 \mu\text{sec}$ .

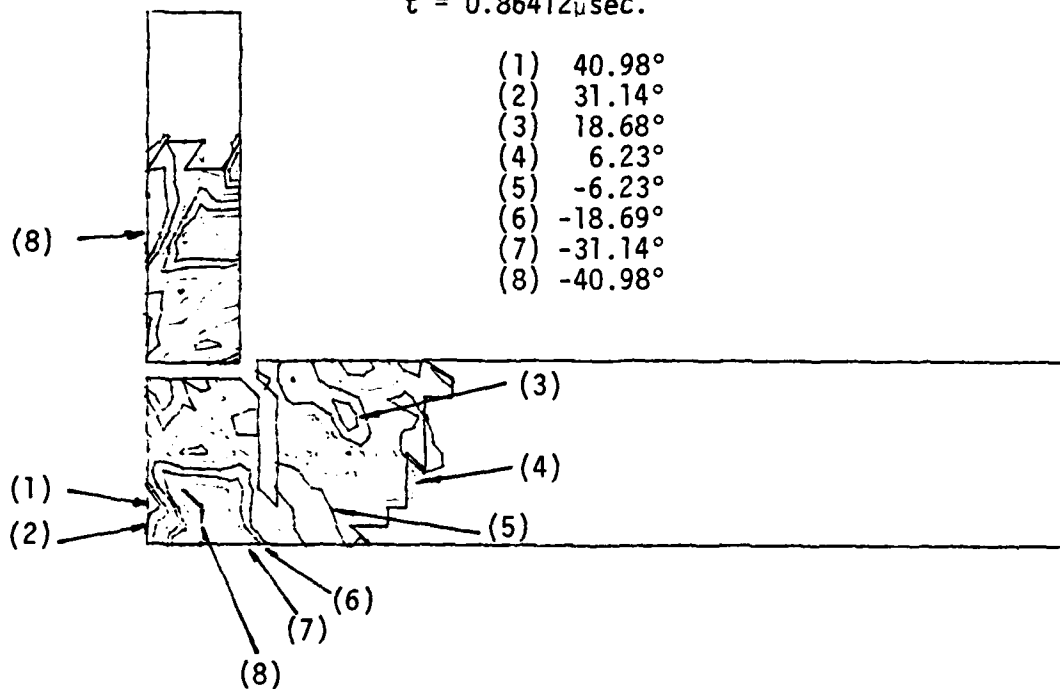


Figure 34. Constant  $\alpha$  contours after  $0.86412 \mu\text{sec}$   
(Model I).

Time: 0.94774 $\mu$ sec.

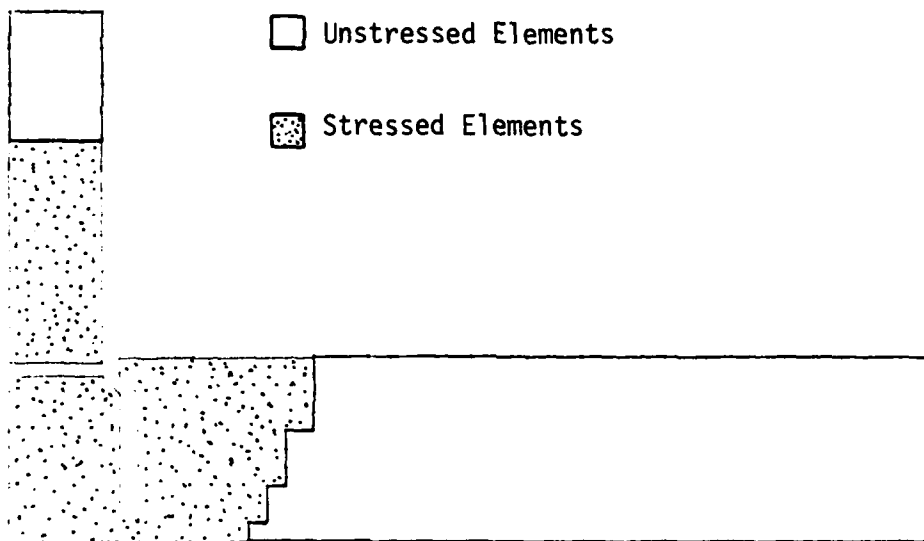


Figure 35. Projectile-target damage pattern after 0.94774 $\mu$ sec (Model I).

indicates the tendency of spalling as the waves are reflected from the back side. Refer to Figure 36. The finite element mesh size, however, is not sufficiently refined to predict the details of the local failure mode. Complete perforation is completed when the last three elements, No. 501, 538 and 537 failed and the plug is dislocated from the target as shown in Figure 37. Orientation of the damage planes corresponding to complete perforation are given in Figure 38.

In this example of a blunt projectile impacting a relatively hard target made of 4340 steel with a Rockwell hardness number of 52 and low fracture toughness, the conditions for plugging failure are met very soon after impact. The flow of material in the radial direction is minimal and the fracture behavior is very brittle. This can be seen from the sequence of diagrams summarized in Figures 39(a) to 39(j) inclusive showing the initiation and completion of the plugging process. This involved nine time steps from  $t = 0.4432\mu\text{sec}$ ,  $t = 1.0723\mu\text{sec}$ , that cover the period of approximately one-half of a micro second. The predicted events involve several idealizations that can be easily improved in future calculations. The most noticeable inaccuracy lies in the size of the triangular elements that resulted in unusually wide fracture path being equal to one tenth of the projectile diameter. This also led to the overly exaggerated straight-line shaped plug. A refinement of the element meshes along the prospective path of plugging would lead to a more realistic prediction of plug profile and minimize abrupt change in fracture path as indicated by the missing corner in Figure 39(j). The relatively low fracture toughness of the material data in Model I also contributes to the brittle-like failure pattern. These shortcomings, however, are considered to be of minor importance in contrast to

Orientations of Damage Plane at  
 $t = 0.94774 \mu\text{sec}$

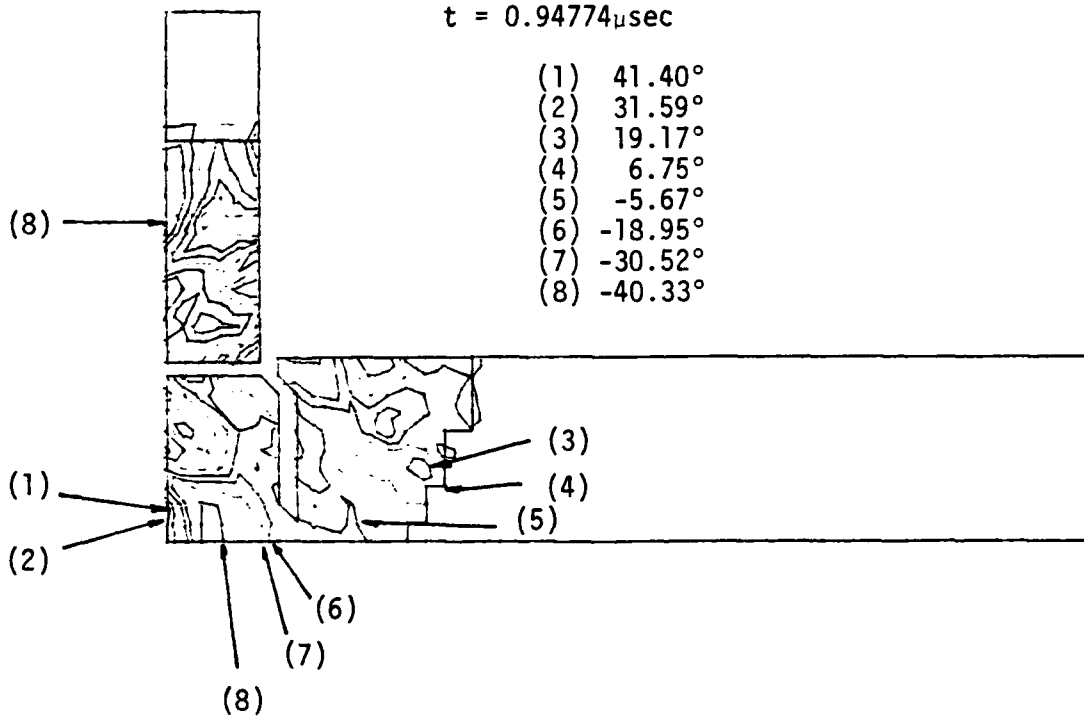


Figure 36. Constant  $\alpha$  contour after  $0.94774 \mu\text{sec}$   
 (Model I).

Time = 1.07226 $\mu$ sec.

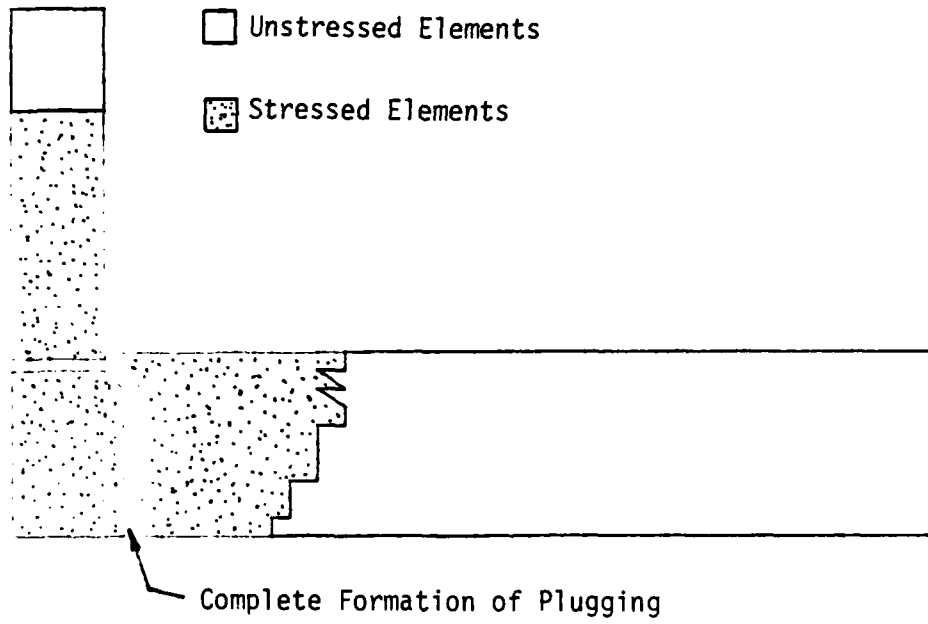


Figure 37. Projectile-target damage pattern after 1.07226 $\mu$ sec (Model I).

Orientation of Damage Plane at  
 $t = 1.07226\mu\text{sec}$ .

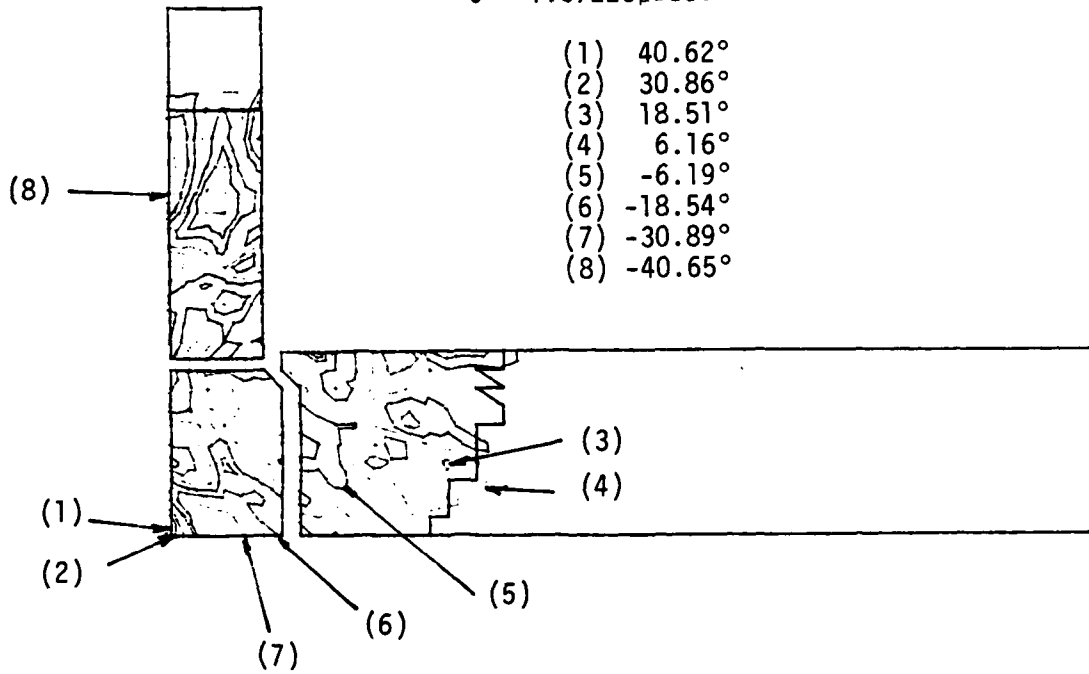
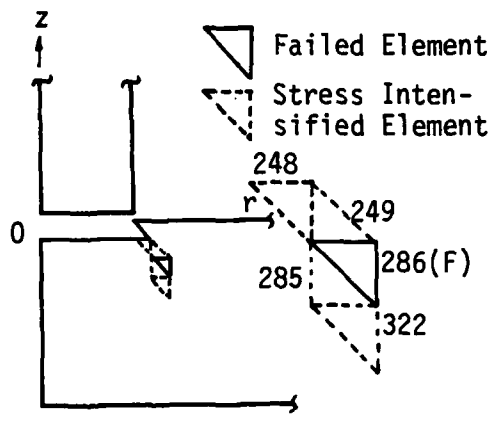
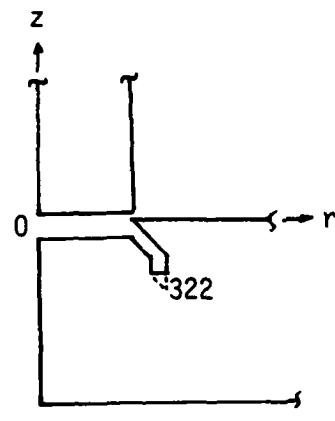


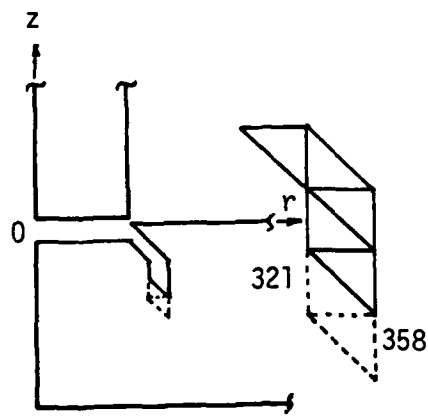
Figure 38. Constant  $\alpha$  contours after  $1.07226\mu\text{sec}$   
(Model I).



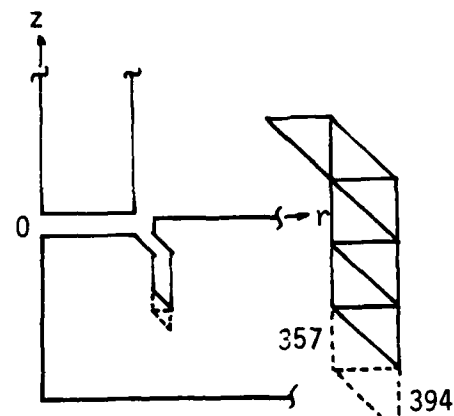
(a)  $t = 0.4432 \mu\text{sec}$



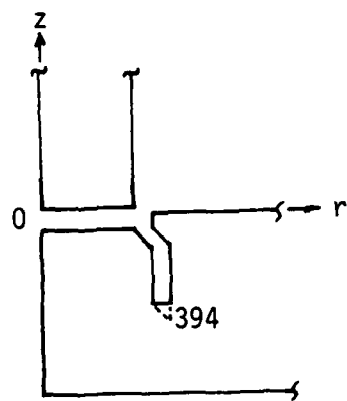
(b)  $t = 0.4855 \mu\text{sec}$



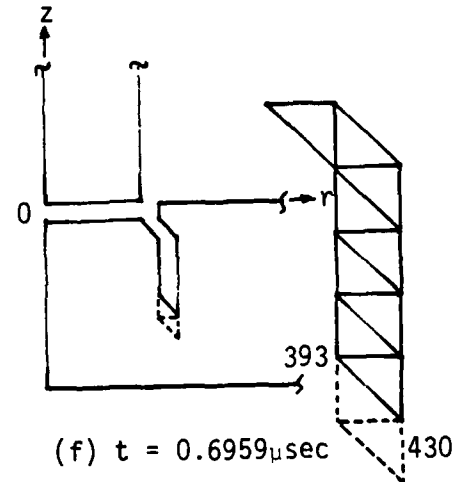
(c)  $t = 0.5273 \mu\text{sec}$



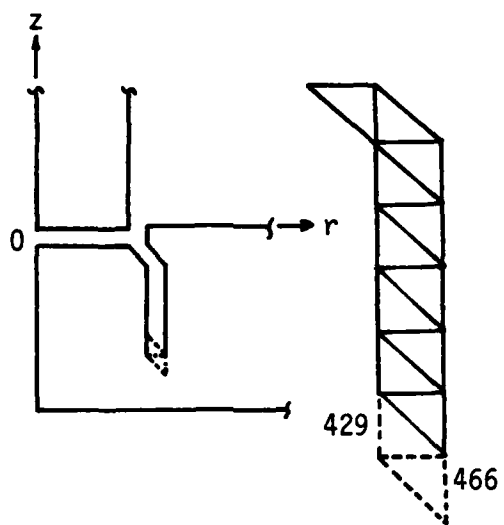
(d)  $t = 0.5693 \mu\text{sec}$



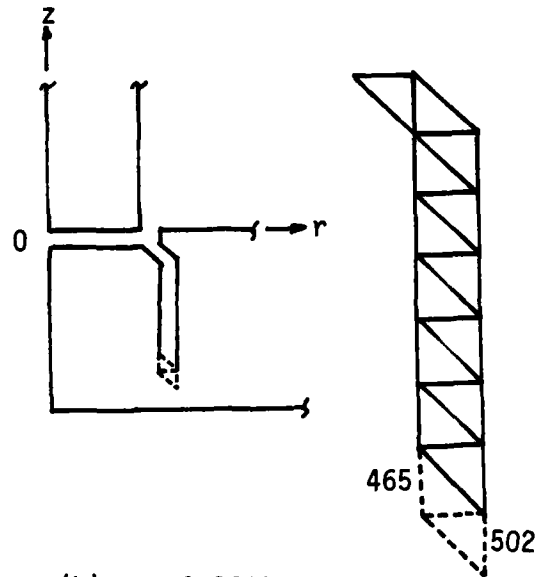
(e)  $t = 0.6114 \mu\text{sec}$



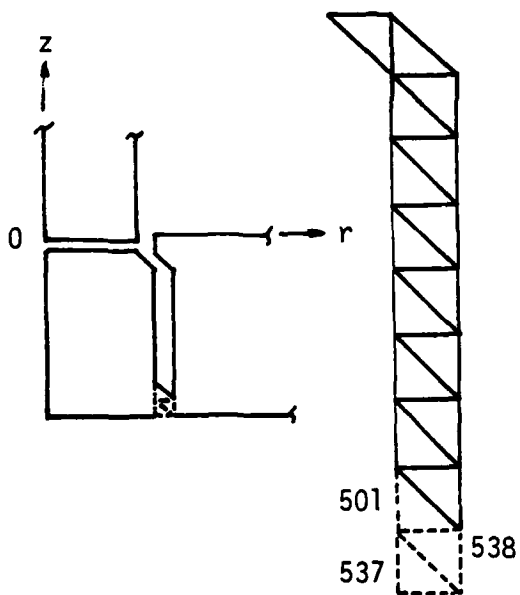
(f)  $t = 0.6959 \mu\text{sec}$



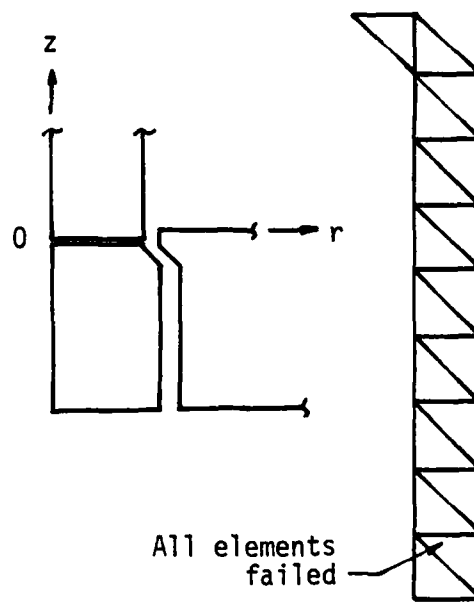
(g)  $t = 0.7381 \mu\text{sec}$



(h)  $t = 0.8642 \mu\text{sec}$



(i)  $t = 0.94774 \mu\text{sec}$



(j)  $t = 1.0723 \mu\text{sec}$

Figure 39. The sequence of plug formation (Model I).

the major improvements achieved in the ADED Code which can consistently incorporate uniaxial strain rate data to material elements in the projectile and target without making ad hoc assumptions. Moreover, many of the drawbacks in the classical theory of plasticity that are inherently embedded in all previous computer codes are overcome in the present damage model based on the theory of strain energy density.

Further insight into the process of penetration mechanics can be gained by studying the stress and strain time history. Referring to those elements near the region where contacts were made at initial impact, Tables 10 to 13 summarize the numerical data for  $\sigma_z$ ,  $\sigma_r$ ,  $\sigma_\theta$  and  $\tau_{rz}$  in a series of time steps from 0.0050 $\mu$ sec to 0.4855 $\mu$ sec. The data are also displayed graphically in Figures 40 to 43 inclusive. It is immediately noticeable that the axial stress component  $\sigma_z$  for those elements referred to in Figure 40 is compressive up to failure. The time sequence of failure for elements 160, 151, 210, 211 and 248 is clearly indicated. The corner element No. 160 on the projectile failed first followed by element No. 151 at the center. Failure of elements No. 210 and 211 in the target occurred next with element No. 248 lacking far behind as it is further away from the contact surface. The amplitudes of the radial stress component  $\sigma_r$  in Figure 41 are much lower than those in the axial direction. Both elements No. 211 and 248 in the projectile experienced tension before failure as the nearby material is heavily compressed in the direction of the projectile motion. The circumferential expansion of the projectile and target is evidenced by the variations of the stress component  $\sigma_\theta$  with time as displayed in Figure 42. Shown in Figure 43 are the time histories of the shear stress component  $\tau_{rz}$  in elements near the contact surface.

Table 10. Axial Stress  $\sigma_z$  in ksi for Elements  
Near Contact (Model I)

Time ( $\mu$ sec)	Element No.					
	160	151	152	210	211	248
0.0050	-140.2	-90.8	-90.8	-41.6	-41.6	-
0.0105	-294.8	-190.9	-190.8	-87.4	-87.4	-0.0004
0.0166	-464.9	-301.1	-300.8	-138.0	-138.0	-0.0021
0.0232	-651.2	-422.1	-421.4	-193.8	-193.8	-0.0075
0.0305	<u>-854.2</u>	-755.4	-719.9	-255.4	-255.5	-0.0224
0.0331	(failed)	<u>-786.6</u>	-750.9	-277.3	-277.5	-0.0248
0.0464		(failed)	<u>-926.7</u>	-381.0	-381.3	-0.0605
0.0611			(failed)	-481.2	-741.1	-0.213
0.0772				<u>-563.4</u>	-844.6	-1.450
0.0949				(failed)	<u>-847.5</u>	-4.151
0.1144					(failed)	-8.103
0.1358						-14.260
0.1594						-24.000
0.1853						-38.930
0.2138						-60.400
0.2452						-88.390
0.2798						-120.15
0.3177						-149.31
0.3595						-167.10
0.4015						-168.20
0.4435						-158.00
0.4855						<u>-277.80</u>
						(failed)

Table 11. Radial Stress  $\sigma_r$  in ksi for Elements  
Near Contact (Model I)

Time ( $\mu$ sec)	Element No.					
	160	151	152	210	211	248
0.0050	-18.3	-11.8	-11.8	-5.4	-5.4	-
0.0105	-38.4	-24.9	-24.9	-11.4	-11.4	-0.0027
0.0166	-60.4	-39.3	-39.3	-17.8	-18.0	-0.0125
0.0232	-84.4	-55.2	-55.2	-24.7	-25.3	-0.0364
0.0305	<u>-110.2</u>	-127.9	94.0	-32.1	-33.4	-0.0852
0.0331	(failed)	<u>105.0</u>	71.1	-34.7	-36.3	-0.102
0.0464		(failed)	<u>-15.7</u>	-47.6	-49.6	-0.113
0.0611			(failed)	-61.2	197.8	-0.732
0.0772				<u>-74.6</u>	204.4	-3.044
0.0949				(failed)	<u>129.9</u>	-9.937
0.1144					(failed)	-14.97
0.1358						-17.55
0.1594						-17.27
0.1853						-14.09
0.2138						-8.31
0.2452						-0.413
0.2798						-0.927
0.3177						-2.064
0.3595						-3.290
0.4015						-4.137
0.4435						-4.051
0.4855						<u>-5.390</u>
						(failed)

Table 12. Circumferential Stress  $\sigma_{\theta}$  in ksi for  
Elements Near Contact (Model I)

Time ( $\mu$ sec)	Element No.					
	160	151	152	210	211	248
0.0050	0.0	0.0	0.0	0.0	0.0	-
0.0105	0.0	-0.014	-0.019	0.004	0.006	0.0033
0.0166	0.0	-0.067	-0.088	0.021	0.028	0.0154
0.0232	0.0	-0.193	-0.254	0.060	0.081	0.0446
0.0305	<u>0.015</u>	-0.447	-0.590	0.139	0.187	0.1036
0.0331	(failed)	<u>-0.530</u>	-0.698	0.165	0.222	0.1226
0.0464		(failed)	<u>-0.545</u>	0.257	0.447	0.3262
0.0611			(failed)	0.269	0.745	0.7134
0.0772				<u>0.341</u>	1.160	1.427
0.0949				(failed)	<u>1.743</u>	2.401
0.1144					(failed)	3.651
0.1358						5.228
0.1594						7.154
0.1853						9.399
0.2138						11.84
0.2452						14.24
0.2798						16.28
0.3177						17.60
0.3595						18.00
0.4015						17.61
0.4435						16.76
0.4855						<u>310.00</u> (failed)

Table 13. Shear Stress in  $\tau_{rz}$  ksi for  
Elements Near Contact (Model I)

Time ( $\mu$ sec)	Element No.					
	160	151	152	210	211	248
0.0050	21.4	0.0	0.0	21.3	0	-
0.0105	45.0	0.021	0.004	44.7	0.043	0.0493
0.0166	70.8	0.099	0.016	70.4	0.199	0.2285
0.0232	99.0	0.287	0.048	98.3	0.579	0.6630
0.0305	<u>129.5</u>	1.223	0.188	128.7	1.345	1.541
0.0331	(failed)	<u>1.352</u>	0.208	139.5	1.596	1.823
0.0464		(failed)	<u>0.230</u>	196.0	3.787	5.255
0.0611			(failed)	260.2	16.580	12.00
0.0772				333.8	27.310	23.81
0.0949					<u>36.950</u>	39.85
0.1144					(failed)	56.35
0.1358						71.92
0.1594						84.44
0.1853						91.09
0.2138						88.72
0.2452						74.64
0.2798						47.94
0.3177						10.72
0.3595						-31.64
0.4015						-69.06
0.4435						-98.59
0.4855						<u>-23.86</u> (failed)

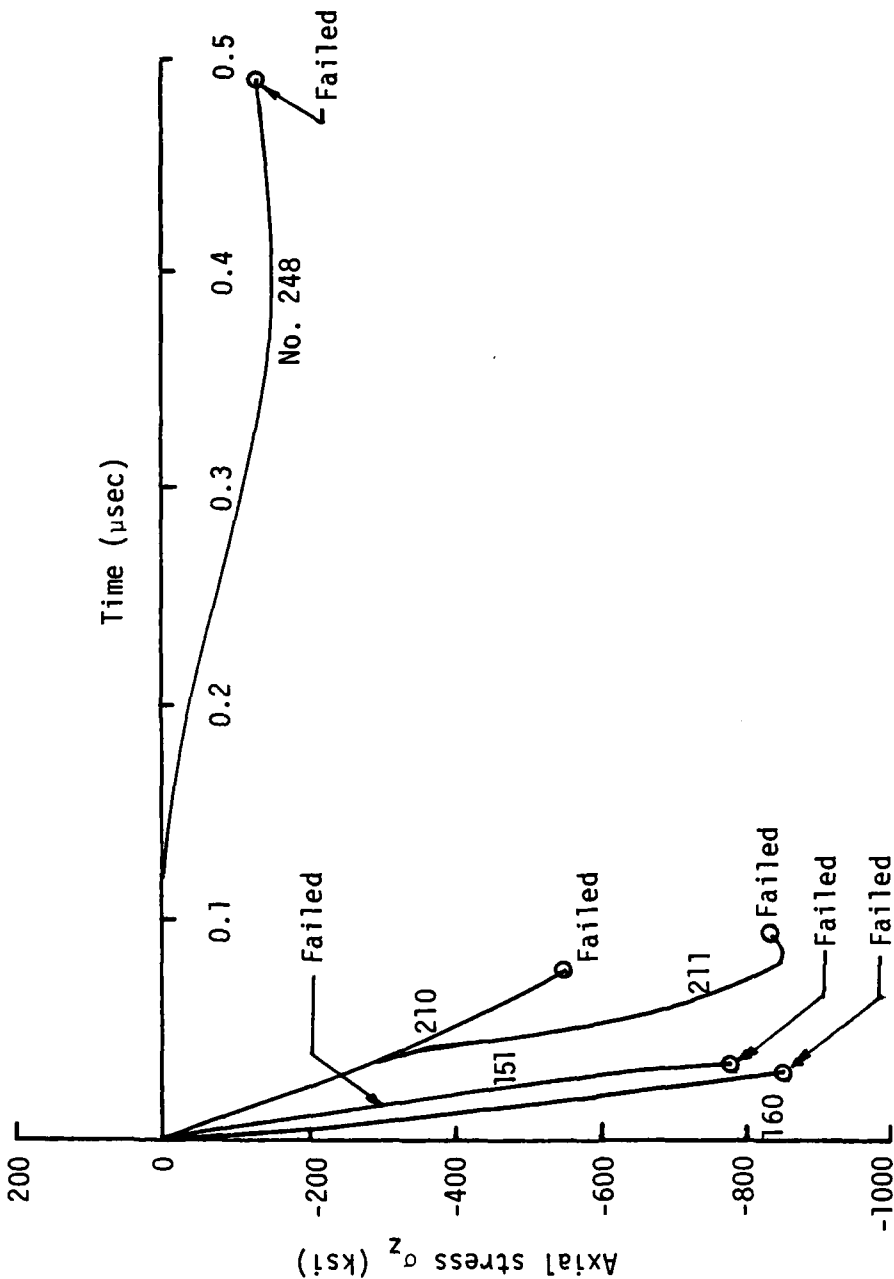


Figure 40. Variation of axial stress with time in elements No. 151, 160, 210, 211 and 248 for Model I.

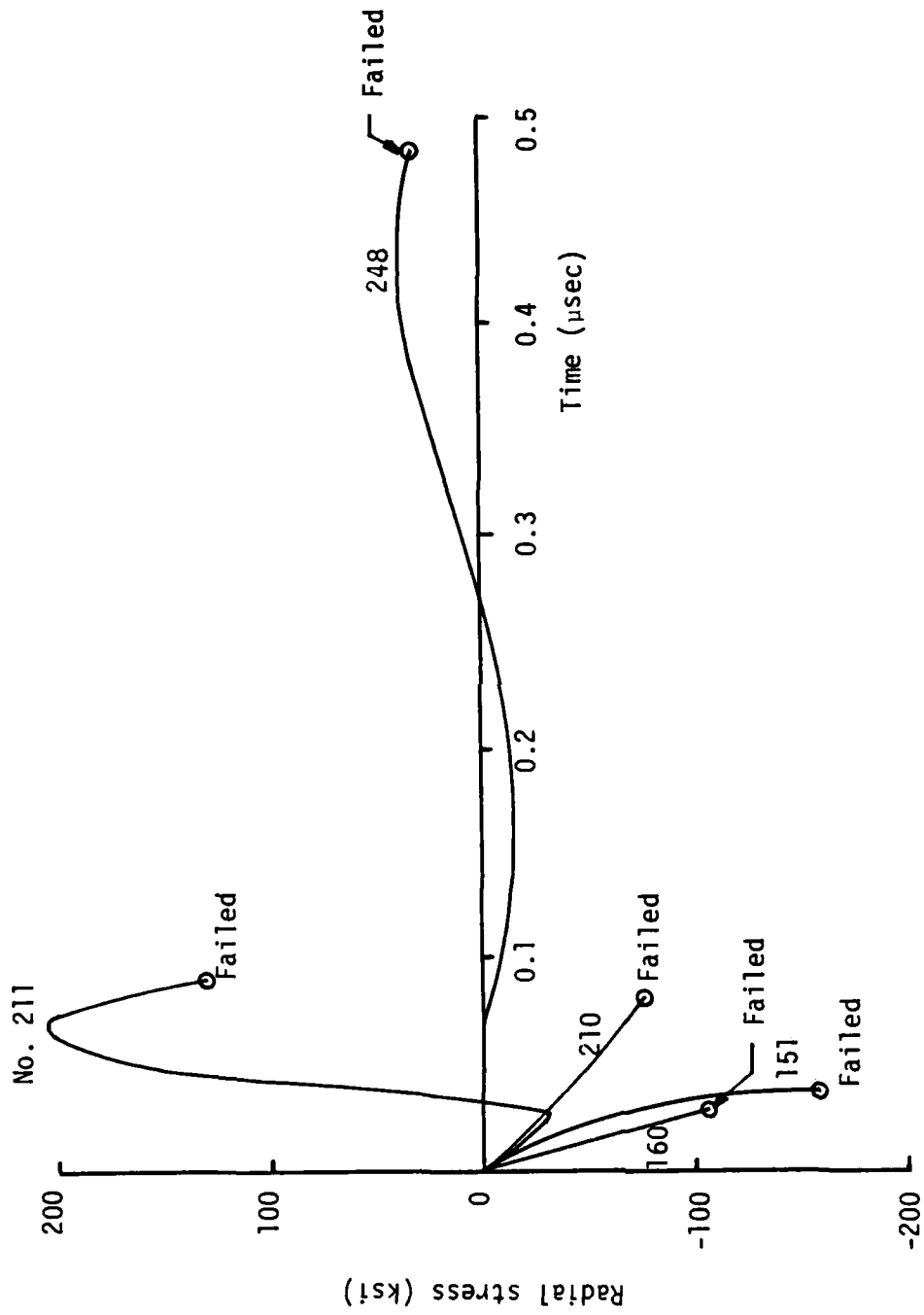


Figure 41. Variation of radial stress with time in elements No. 151, 160, 210, 211 and 248 for Model I.

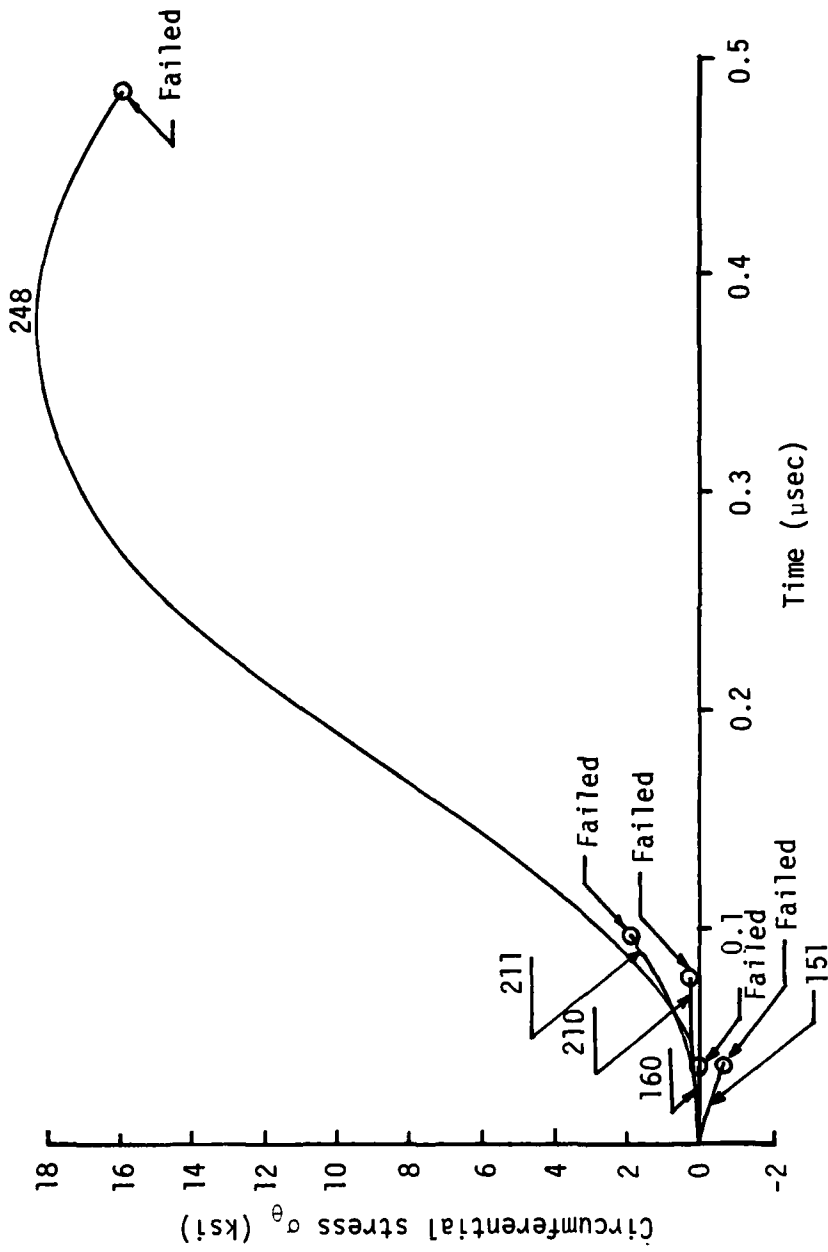


Figure 42. Variation of circumferential stress with time in elements No. 151, 160, 210, 211 and 248 for Model I.

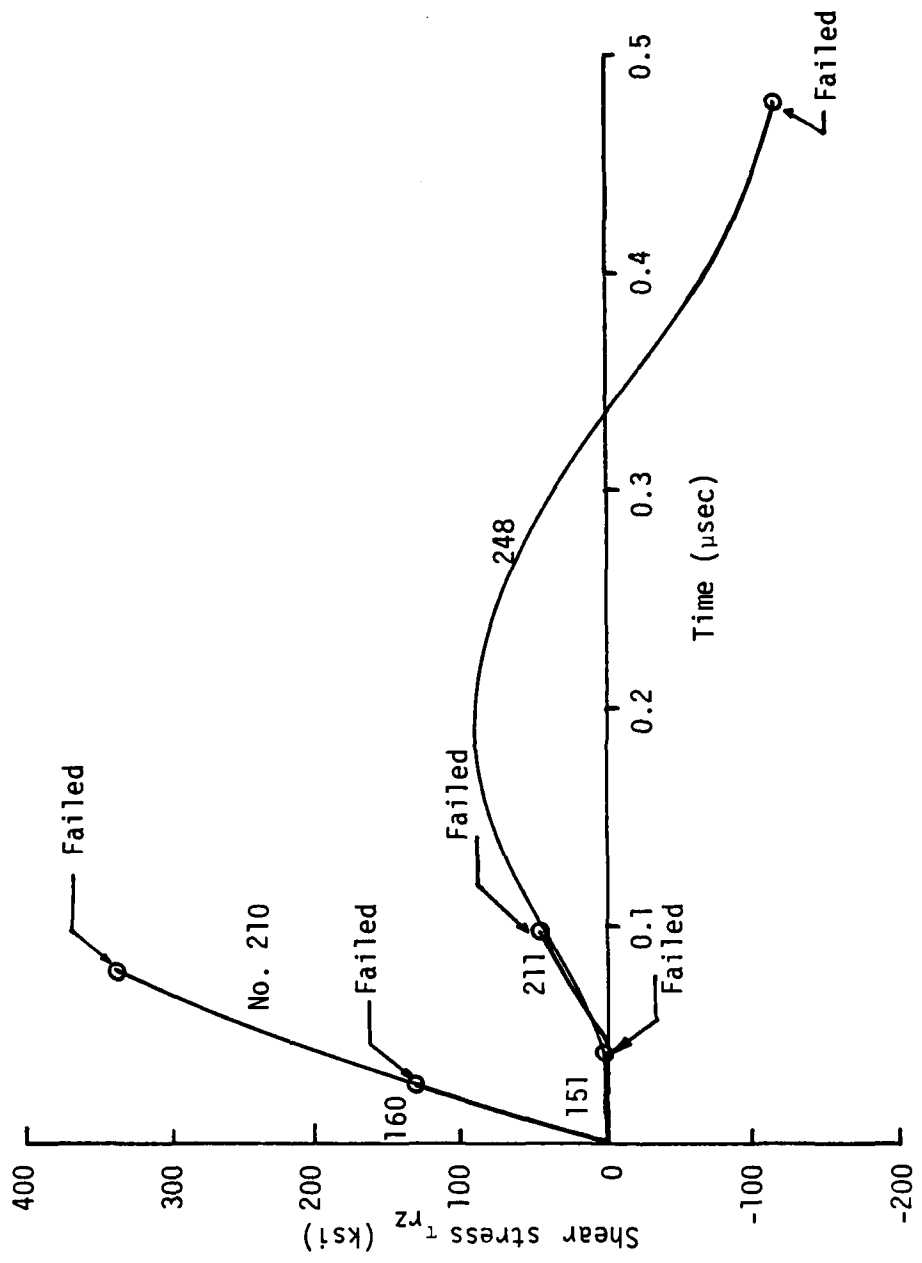


Figure 43. Variations of shear stress with time in elements No. 151, 160, 210, 211 and 248 for Model I.

Tables 14 to 17 inclusive outlines the strain rates in the axial, radial and circumferential direction. First of all, strain rates in the axial direction can vary by several orders of magnitude from  $10^6 \text{ sec}^{-1}$  in element No. 160 to  $10 \text{ sec}^{-1}$  in element No. 248. This wide range of strain rates was covered by the data bank in Figure 10. As it is to be expected, the strain rates did not vary as much in the radial and circumferential directions. They varied mostly from  $10^{-1} \text{ sec}^{-1}$  to  $10^4 \text{ sec}^{-1}$  except for the shear strain component in element No. 160 that reached  $10^5 \text{ sec}^{-1}$ . In retrospect, it is essential to have a theory such as the one proposed in this work that can adjust for the changes in strain rates from element to element.

*Model II.* Consider now the same 4340 steel with high fracture toughness at the same rates from  $10^{-4} \text{ sec}^{-1}$  to  $10^6 \text{ sec}^{-1}$  as shown in Figure 44. The areas under the true stress and true strain curves have increased as compared to those in Figure 10 for Model I. The relation between the yield strength and critical strain energy density is given in Figure 45 such that high  $\sigma_y$  corresponds to low  $(dW/dV)_c$  and vice versa. This trade-off property is typical of many of the engineering metal alloys. The ADED Code will be employed to analyze the damage and failure pattern of the projectile and target by holding all other variables constant other than the uniaxial data as mentioned earlier.

With the tougher material, more time is needed to damage and/or fail the target. Larger time steps will be taken. Moreover, more energy will be dissipated by permanent deformation. Without going into the details of the results for the initial time steps, Figure 46 displays the damage pattern at  $t = 0.2287 \mu\text{sec}$ . The corner element No. 160 is broken and several of the elements in contact have been damaged and they are shaded. The permanently indented surface of the target at contact becomes more noticeable in Figures 47 and 48 corresponding to  $t = 0.3643 \mu\text{sec}$  and

Table 14. Axial Strain Rate  $\dot{\epsilon}_z$  ( $\times 10^5 \text{sec}^{-1}$ )  
for Elements Near Contact (Model I)

Time ( $\mu\text{sec}$ )	Element No.					
	160	151	152	210	211	248
0.0050	-10.56	-6.84	-6.84	-3.14	-3.14	-
0.0105	-10.60	-6.86	-6.85	-3.14	-3.14	$1.97 \times 10^{-6}$
0.0166	-10.60	-6.86	-6.85	-3.15	-3.15	$-2.65 \times 10^{-5}$
0.0232	-10.55	-6.85	-6.83	-3.16	-3.16	$-1.33 \times 10^{-4}$
0.0305	<u>-10.45</u>	-6.82	-6.78	-3.18	-3.18	$-4.45 \times 10^{-4}$
0.0331	(failed)	<u>-6.84</u>	-6.79	-3.18	-3.18	$-3.47 \times 10^{-4}$
0.0464		(failed)	<u>-6.58</u>	-2.94	-2.94	$-1.84 \times 10^{-3}$
0.0611			(failed)	-2.58	-2.58	$-6.11 \times 10^{-3}$
0.0772				<u>-1.92</u>	-1.92	$-1.77 \times 10^{-2}$
0.0949				(failed)	<u>-1.32</u>	$-3.90 \times 10^{-2}$
0.1144					(failed)	$-6.48 \times 10^{-2}$
0.1358						$-1.04 \times 10^{-1}$
0.1594						$-1.59 \times 10^{-1}$
0.1853						$-2.27 \times 10^{-1}$
0.2138						$-2.99 \times 10^{-1}$
0.2452						$-3.54 \times 10^{-1}$
0.2798						$-3.67 \times 10^{-1}$
0.3177						$-3.09 \times 10^{-1}$
0.3595						$-1.78 \times 10^{-1}$
0.4015						$-1.98 \times 10^{-2}$
0.4435						$9.40 \times 10^{-2}$
0.4855						<u><math>1.90 \times 10^{-1}</math></u> (failed)

Table 15. Radial Strain Rate  $\dot{\epsilon}_r$  ( $\times 10^2 \text{sec}^{-1}$ )  
for Elements Near Contact (Model I)

Time ( $\mu\text{sec}$ )	Element No.					
	160	151	152	210	211	248
0.0050	0.0	0.0	0.0	0.0	0.0	-
0.0105	2.84	-0.87	-1.43	2.82	-0.18	-0.18
0.0166	9.39	-2.88	-4.71	9.30	-0.61	-0.61
0.0232	20.66	-6.33	-10.35	20.37	-1.34	-1.34
0.0305	<u>37.76</u>	-11.59	-10.95	37.07	-2.46	-2.46
0.0331	(failed)	<u>-11.42</u>	-18.09	36.75	-2.46	-2.46
0.0464		(failed)	<u>2.25</u>	16.98	6.36	6.33
0.0611			(failed)	-14.63	16.89	16.74
0.0772				<u>-63.43</u>	-85.42	937.3
0.0949				(failed)	<u>-140.30</u>	-141.5
0.1144					(failed)	-889.3
0.1358						-316.9
0.1594						251.4
0.1853						75.81
0.2138						115.3
0.2452						141.0
0.2798					-	153.4
0.3177						153.2
0.3595						133.8
0.4015						78.57
0.4435						-19.94
0.4855						<u>-146.7</u> (failed)

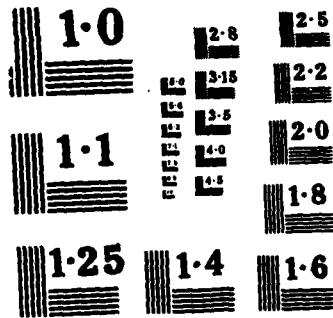
Table 16. Circumferential Strain Rate  $\dot{\epsilon}_\theta$  ( $\times 10^2 \text{sec}^{-1}$ )  
for Elements Near Contact (Model I)

Time ( $\mu\text{sec}$ )	Element No.					
	160	151	152	210	211	248
0.0050	0.0	0.0	0.0	0.0	0.0	-
0.0105	0.03	-0.87	-1.15	0.03	0.4	0.20
0.0166	0.10	-2.88	-3.80	0.90	1.20	0.66
0.0232	0.21	-6.33	-8.34	1.97	2.64	1.46
0.0305	<u>0.38</u>	-11.59	-15.27	3.61	4.84	2.69
0.0331	(failed)	<u>-11.42</u>	-15.05	3.57	4.78	2.65
0.0464		(failed)	<u>-3.85</u>	2.29	5.65	5.10
0.0611			(failed)	0.28	6.79	8.82
0.0772				<u>1.49</u>	8.59	14.77
0.0949				(failed)	<u>10.97</u>	18.34
0.1144					(failed)	21.38
0.1358						24.51
0.1594						27.23
0.1853						28.85
0.2138						28.51
0.2452						25.51
0.2798						19.63
0.3177						11.60
0.3595						3.22
0.4015						-3.06
0.4435						-6.77
0.4855						<u>-10.01</u>
						(failed)

Table 17. Shear Strain Rate  $\dot{\epsilon}_{rz}$  ( $\times 10^3 \text{sec}^{-1}$ )  
for Elements Near Contact (Model I)

Time ( $\mu\text{sec}$ )	Element No.					
	160	151	152	210	211	248
0.0050	185.4	0.0	0.0	184.7	0.0	-
0.0105	185.7	1.68	0.03	184.5	0.34	0.39
0.0166	185.2	0.57	0.09	183.7	1.12	1.28
0.0232	183.5	1.23	0.20	182.1	2.47	2.83
0.0305	<u>180.3</u>	2.25	0.38	179.4	4.54	5.20
0.0331	(failed)	<u>2.23</u>	0.37	179.6	4.48	5.12
0.0464		(failed)	<u>0.16</u>	184.1	7.13	11.17
0.0611			(failed)	190.0	10.71	19.97
0.0772				<u>198.1</u>	14.22	23.81
0.0949				(failed)	<u>18.48</u>	39.23
0.1144					(failed)	36.69
0.1358						31.47
0.1594						23.00
0.1853						11.11
0.2138						-3.60
0.2452						-19.44
0.2798						-33.52
0.3177						-42.47
0.3595						-43.94
0.4015						-38.60
0.4435						-30.46
0.4855						<u>-21.38</u> (failed)





NATIONAL BUREAU OF STANDARDS  
MICROCOPY RESOLUTION TEST CHART

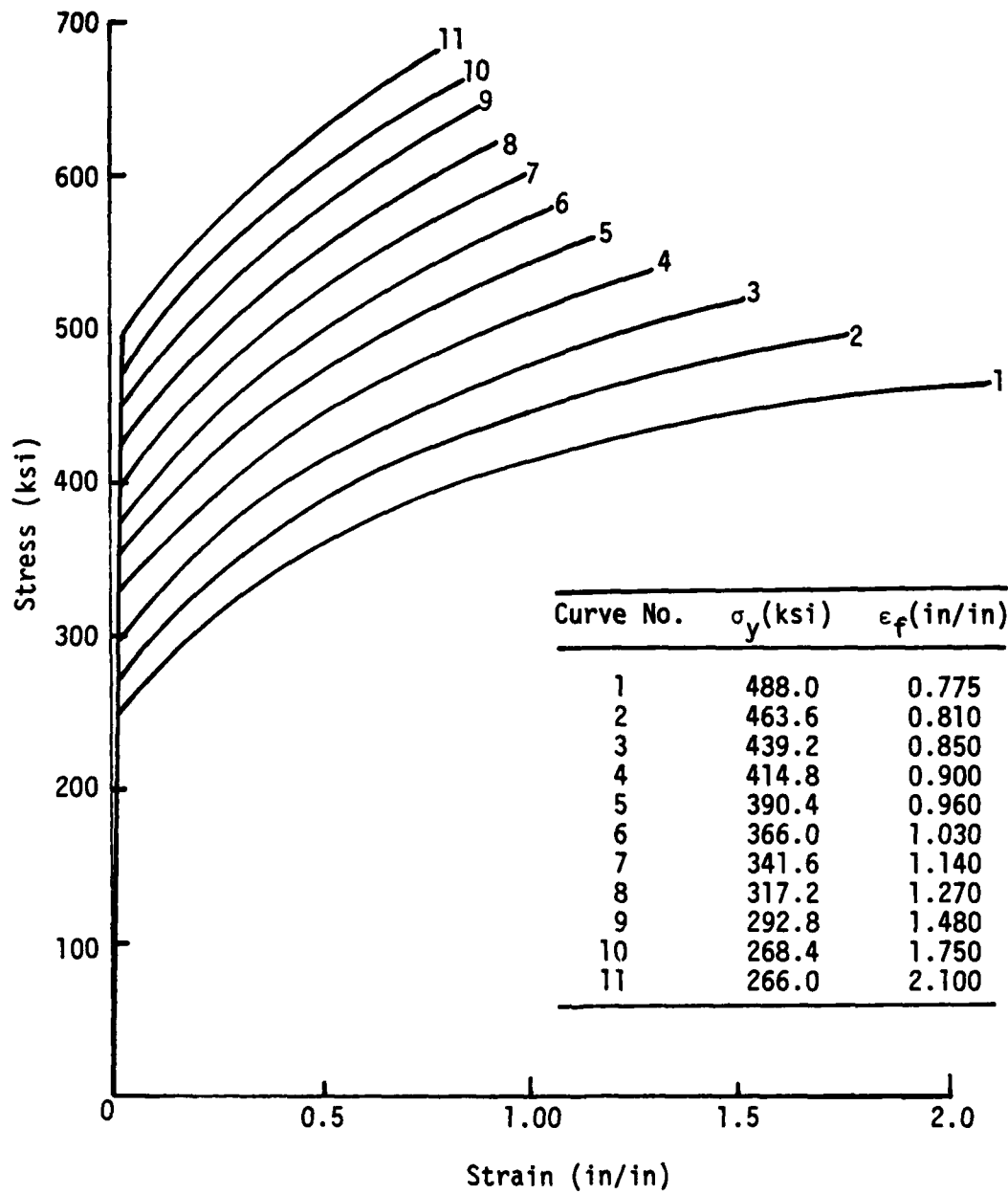


Figure 44. True stress and true strain curve in ADED data bank for Model II.

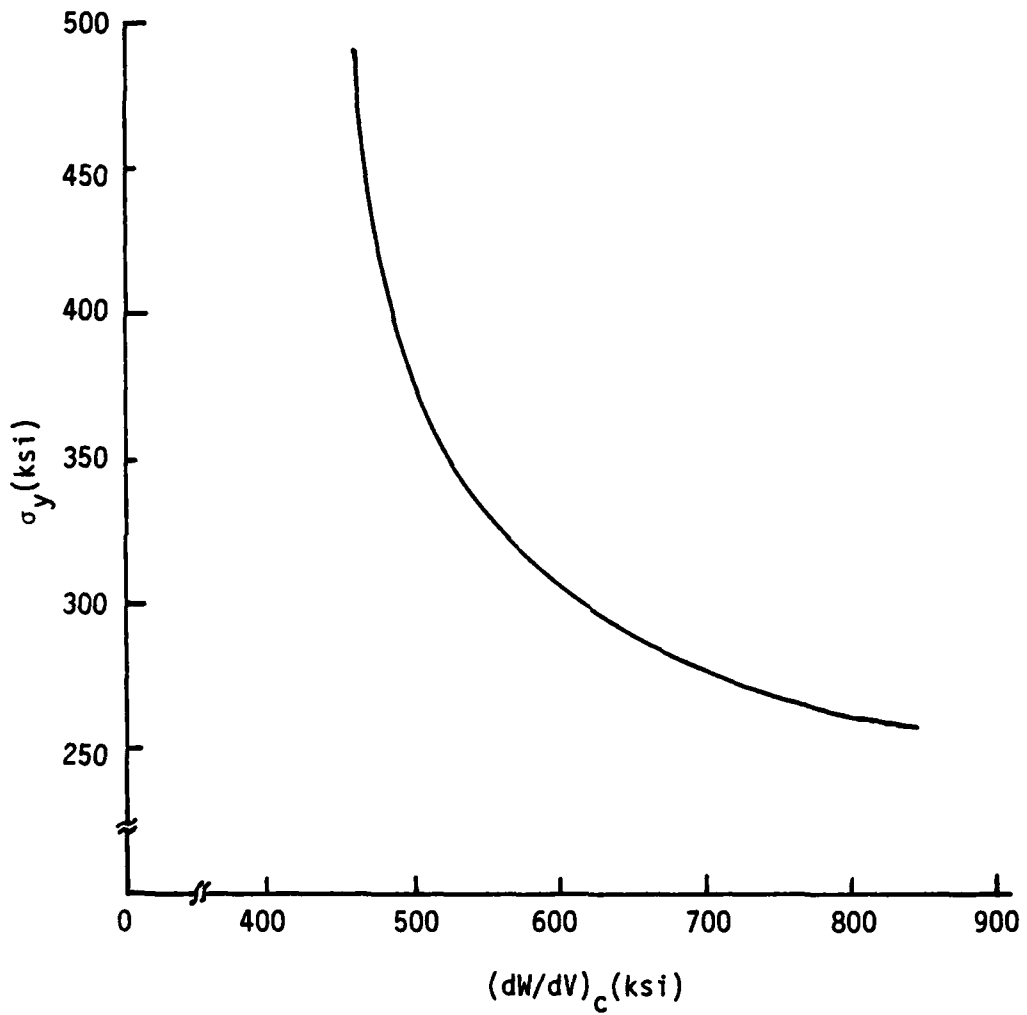


Figure 45. Relation between yield strength and critical strain energy density function for hardened 4340 steel (Model II).

Time: 0.2287 $\mu$ sec.

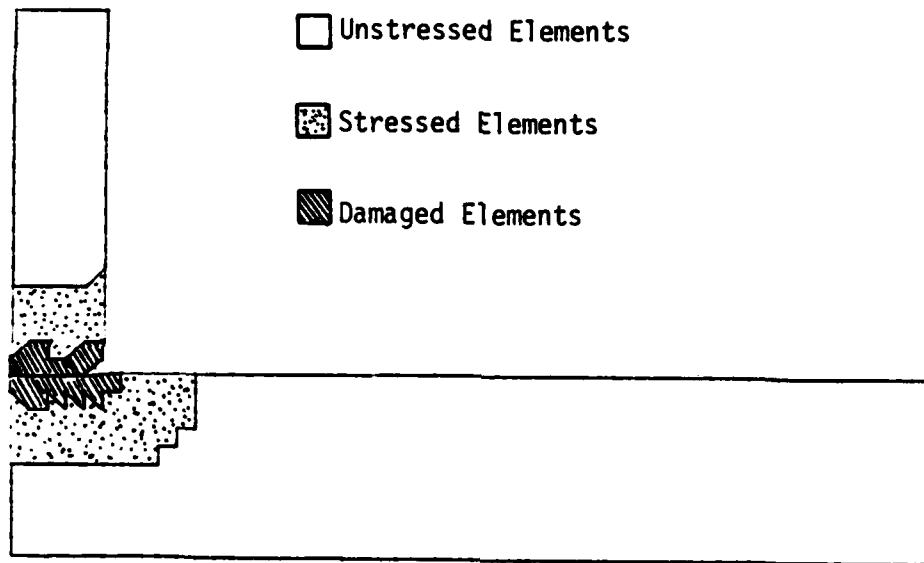


Figure 46. Projectile-target damage pattern after 0.2287 $\mu$ sec (Model II).

Time: 0.3643 $\mu$ sec.

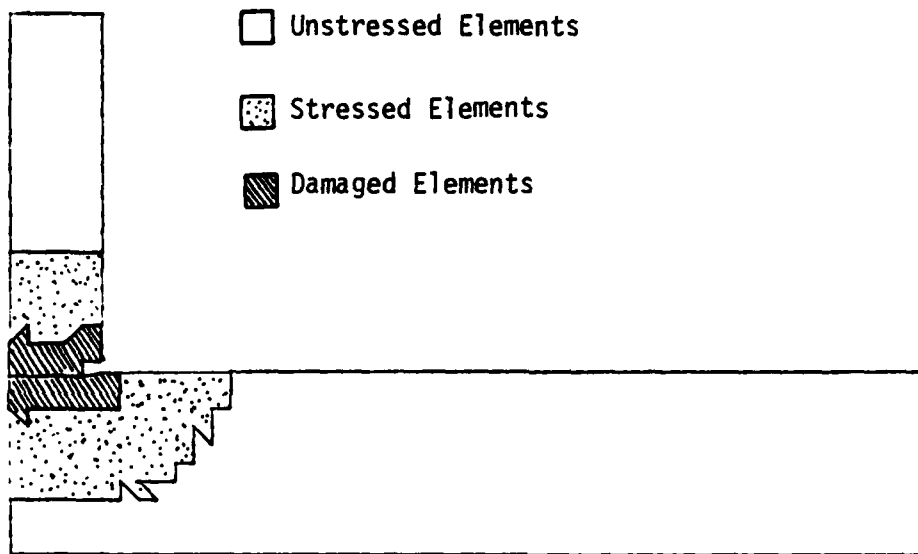


Figure 47. Projectile-target damage pattern after 0.3643 $\mu$ sec (Model II).

Time: 0.4075 $\mu$ sec.

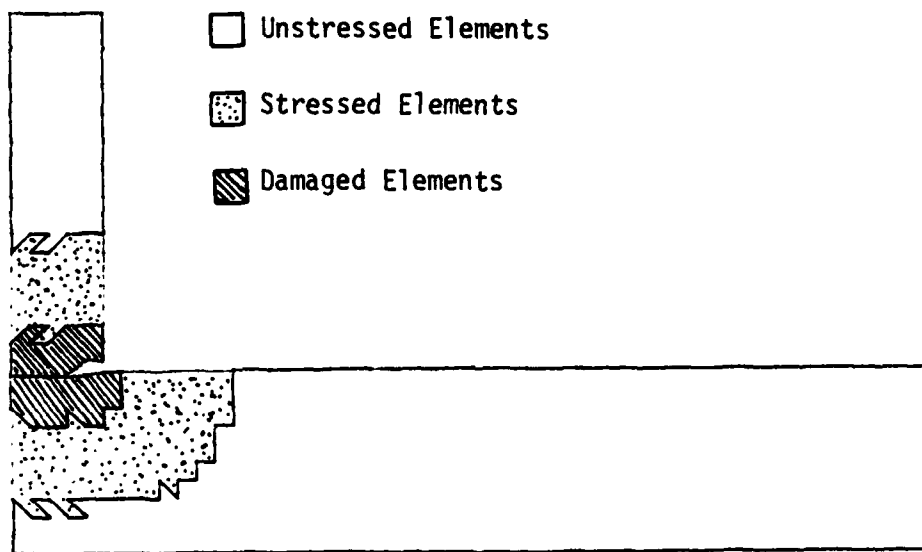


Figure 48. Projectile-target damage pattern after 0.4075 $\mu$ sec (Model II).

0.4075 $\mu$ sec. Elements No. 159 and 158 of the projectile are fractured. This phenomenon has been observed experimentally for targets made of hard material. The damage zone is seen to increase as the waves propagate. Figure 49 shows that the remaining elements in the first layer of the projectile are all broken except for element No. 154 acting as a debris or fragment<sup>\*</sup>. The debris disappears in Figure 50 at  $t = 0.4953\mu$ sec on account of the idealized assumption in this preliminary work to neglect the influence of the failed elements. As the damage zone increases with the propagation of waves, plug initiation is seen to occur at element No. 282 in Figure 51 when  $t = 0.5345\mu$ sec. Referring to Figure 13, the three elements that have common sides to element No. 282 are elements No. 245, 281 and 283. At failure, the rate of change of volume with surface area, i.e.,  $dV/dA$  in element No. 282 became exceedingly high with a value of 105.83 in in comparison with 2.508 in, 2.566 in and 2.559 in for elements No. 245, 281 and 283. The strain energy density function  $dW/dV$  in elements No. 245 and 281 are, respectively, 20,977 psi and 11,268 psi both of which are higher than the value of  $dW/dV = 8,826$  psi in the failed element No. 282. This exhibits the nature of failure at high strain rates where the area under the stress and strain curve alone cannot fully describe the event of dynamic failure<sup>\*\*</sup>. The constant  $\alpha$  contours at plug initiation are displayed in Figure 52. The two curves with  $\alpha = -18.82^\circ$  and  $-31.49^\circ$  are directed almost vertically from element No. 282. This is indicative of the direction of plugging that is headed normal to

---

\* In fact, each element will fail at a different time and can be analyzed as such if refinements in time steps are made. The influence of the fragments can also be treated without difficulty. This will be discussed in more detail subsequently.

\*\* In contrast,  $dV/dA$  does not change appreciably in creep loading and damage can be more accurately monitored by dissipation due to  $dW/dV$  alone. It becomes obvious that there prevails many situations where both  $dV/dA$  and  $dW/dV$  can play equally important roles as in regions near the tip of a moving crack with moderate speed.

Time: 0.4516 $\mu$ sec.

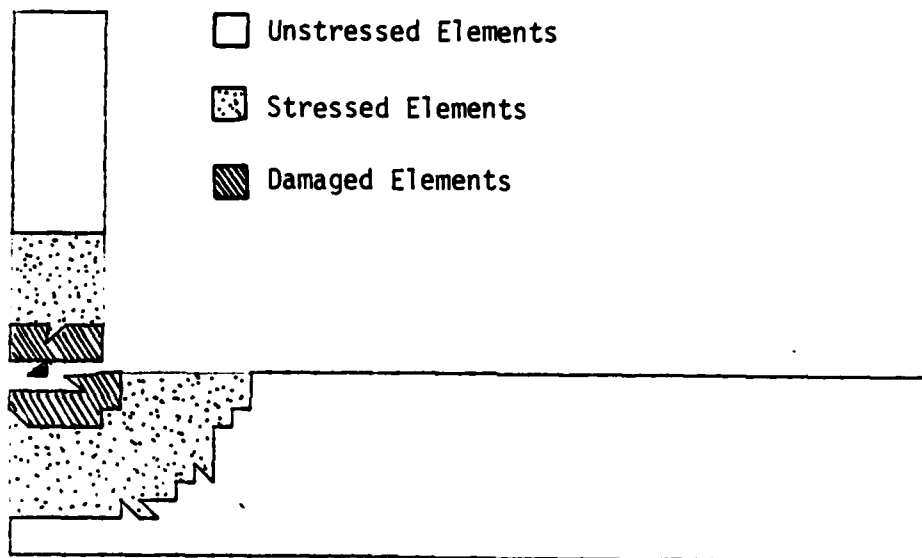


Figure 49. Projectile-target damage pattern after 0.4516 $\mu$ sec (Model II).

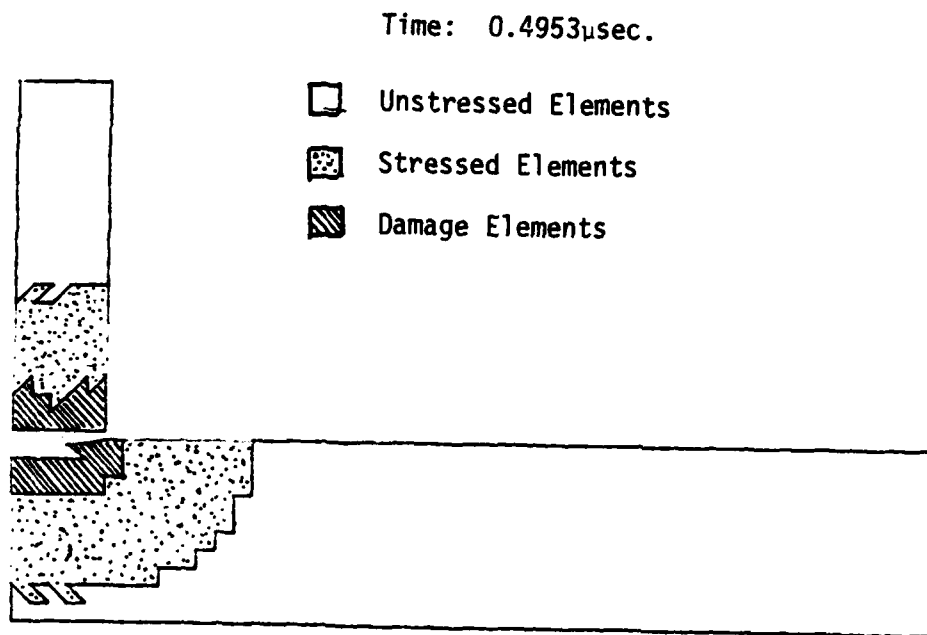


Figure 50. Projectile-target damage pattern after 0.4953 $\mu$ sec (Model II).

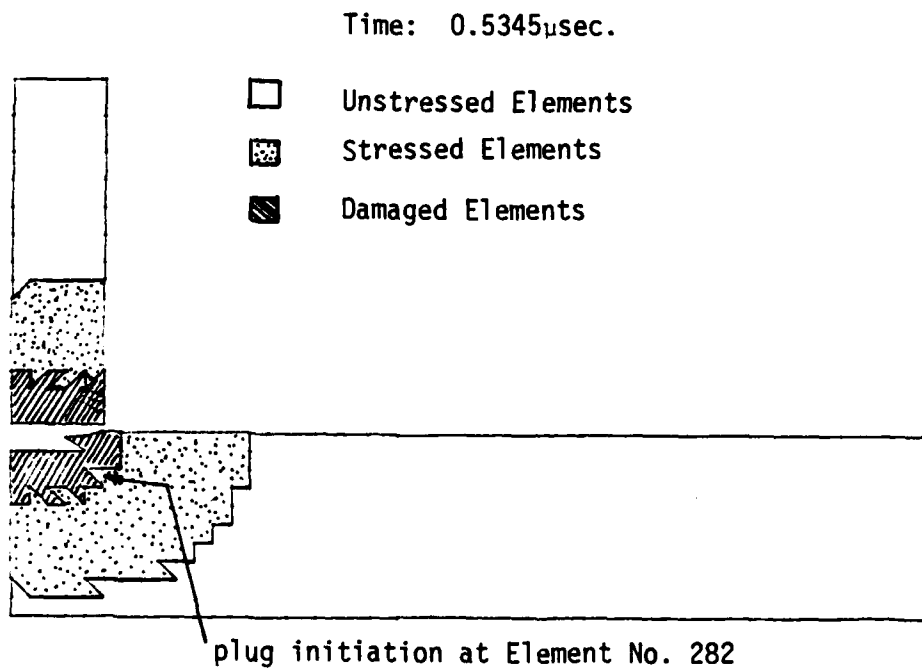


Figure 51. Projectile-target damage pattern after 0.5345 $\mu$ sec (Model II).

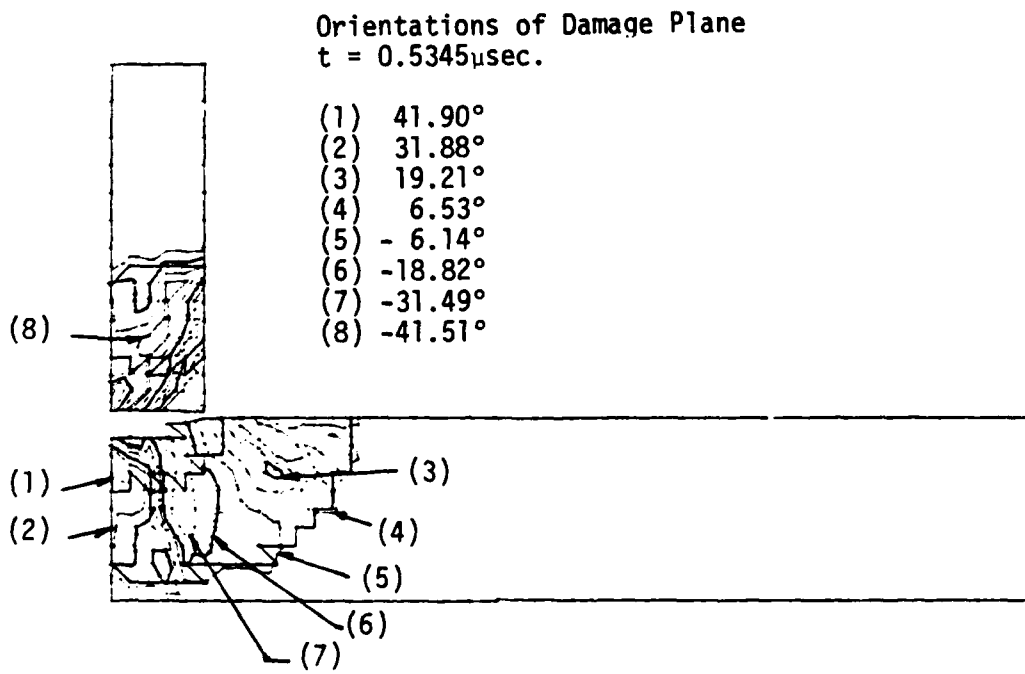


Figure 52. Constant  $\alpha$  contours after  $0.5345\mu\text{sec}$  (Model II).

the target surface. It should be reiterated that the global fracture path in the damage theory is assumed to follow the direction of constant  $\alpha$  line and not  $\alpha$  itself which has been emphasized in the discussion of results for Model I.

Two distinct features of the results for Model II are observed. First, plug initiated directly under the corner of the projectile which is closer to experimental observation when compared with Model I in Figure 19 that occurred further away in the radial direction. Materials near contact are severely damaged before failure. This did not occur in Model I as the fracture toughness of the material were too low that led to predominantly brittle fracture. The detail features of plugging in Model II can still be improved by reducing the finite element mesh size and the inclusion of failed elements in the calculation. Refer to the results in Tables 18 and 19 for some typical values of  $\alpha$  and  $dV/dA$  in those elements near the contact surface for Model II. Table 20 summarizes the data of the equivalent uniaxial stress and strain curve for elements No. 160, 151 and 210 on the damaged plane, the direction of which is given in Table 18. Unlike the results in Figure 17 for Model I, the curves in Figure 53 are all nonlinear as energies are dissipated in addition to those to cause fracture or failure. Unloading has also occurred in element No. 210. This is shown in Figure 53.

The failure of the internal element No. 282 creates a small crack and intensifies the stress state in its neighboring elements No. 245, 246, 281 and 318. A magnification factor<sup>\*</sup> of 20 is employed as explained in Model I. This leads to

---

\*The procedure will be automated in the future ADED Code where the nodes of the triangular elements can be shifted to simulate a  $1/r$  singular field for the strain energy density function  $dW/dV$  where  $r$  is a radial distance. This character being independent of the constitutive relations of the material is, in general, valid for simulating the effect of a localized defect with its major axis differing by an order of magnitude in relation to its minor axis. This, however, will require the use of isoparametric elements instead of the constant stress elements.

Table 18. Angle  $\alpha$  for Elements Near Contact in Model II

Time ( $\mu$ sec)	Element No.						
	160	151	156	210	211	246	248
0.0200	-35.33	-45.00	-45.00	-20.16	-45.00	-	-
0.0420	-35.45	-44.88	-44.99	-20.65	-44.48	-20.91	0.68
0.0928	-35.46	-44.46	-44.96	-20.34	-42.32	-24.53	1.21
0.1543	-35.03	-44.09	-44.90	-16.83	-37.39	-30.02	- 0.75
0.2287	<u>-34.24</u>	-43.90	-44.84	-11.32	-29.60	-32.18	- 2.89
0.2716	(failed)	-43.89	-44.77	- 7.20	-24.82	-31.59	- 3.72
0.3187		-43.98	-44.75	- 2.73	-13.90	-28.95	- 3.49
0.3643		-44.07	-44.66	0.74	-37.99	-24.29	- 1.90
0.4075		-44.15	-44.55	2.98	-23.13	-18.37	0.79
0.4516		<u>-44.22</u>	<u>-44.47</u>	4.08	-16.03	-11.07	3.22
0.4953		(failed)	(failed)	4.28	- 8.90	- 3.77	4.33
0.5345				3.99	- 2.66	1.37	4.04
0.5745				3.29	4.17	<u>5.03</u>	- 1.83
0.6185				<u>2.15</u>	14.57	(failed)	-18.66
				(failed)			

Table 19. Rate of Change of Volume with Surface Area  $dV/dA$  (in)  
for Elements Near Contact (Model II)

Time ( $\mu$ sec)	Element No.					
	160	151	156	210	211	248
0.02	2.431	2.828	2.828	2.131	2.828	
0.042	2.455	2.820	2.827	2.139	2.806	0.003
0.0928	2.457	2.781	2.824	2.142	2.715	3.185
0.1543	2.451	2.759	2.822	2.129	2.639	2.923
0.2287	<u>2.419</u>	2.714	2.808	2.076	2.371	2.354
0.2716	(failed)	2.729	2.799	2.037	2.281	2.293
0.3188		2.730	2.794	1.951	2.172	2.246
0.3643		2.733	2.787	1.387	2.685	2.250
0.4075		2.737	2.779	0.745	2.015	2.306
0.4516		<u>2.742</u>	<u>2.773</u>	1.342	4.206	2.561
		(failed)	(failed)			

Table 20. Equivalent Uniaxial Stress and Strain in Elements  
Near Contact on Damaged Plane for Model II

Time ( $\mu$ sec)	Element No.					
	160		151		210	
	$\epsilon = \epsilon_{\xi} = \epsilon_{\eta}$ ( $\mu$ in/in)	$\sigma = \sigma_{\xi} = \sigma_{\eta}$ ksi	$\epsilon = \epsilon_{\xi} = \epsilon_{\eta}$ ( $\mu$ in/in)	$\sigma = \sigma_{\xi} = \sigma_{\eta}$ ksi	$\epsilon = \epsilon_{\xi} = \epsilon_{\eta}$ ( $\mu$ in/in)	$\sigma = \sigma_{\xi} = \sigma_{\eta}$ ksi
0.0200	- 10,730	-322.0	- 6,913	-207.4	- 3,149	- 94.5
0.0420	- 22,220	-491.0	- 14,460	-433.9	- 6,611	-198.3
0.0928	- 47,370	-502.2	- 30,930	-471.0	-13,320	-399.7
0.1543	- 77,950	-514.2	- 48,840	-478.7	-15,920	-439.9
0.2287	<u>-108,900</u>	<u>-528.7</u>	- 68,070	-486.3	-13,940	-380.4
0.2716	(failed)		- 78,490	-490.1	-10,260	-270.2
0.3188			- 89,630	-494.2	- 6,146	-146.7
0.3643			-100,100	-522.2	- 2,930	- 50.2
0.4075			-110,000	-525.6	- 1,089	5.0
0.4516			<u>-118,700</u>	<u>-528.6</u>	- 1,614	- 10.7
			(failed)			

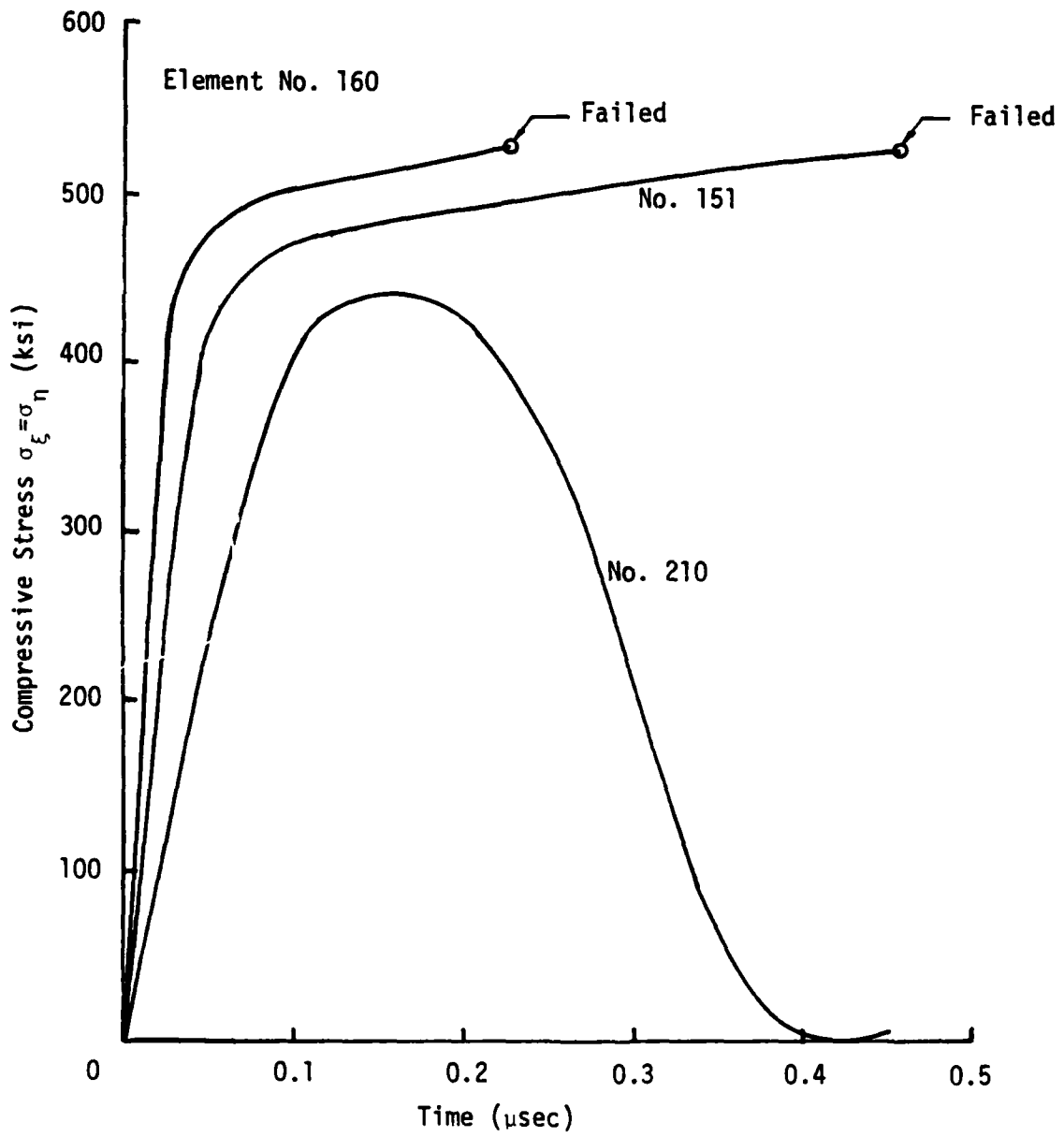


Figure 53. Equivalent uniaxial stress and strain for elements near contact (Model II).

the failure pattern in Figure 54 at  $t = 0.5977\mu\text{sec}$  where fracture is extending in both the upward and downward direction. Elements No. 245, 246, 281 and 318 are now all failed. The waves have propagated to the back side of the target plate and spread radially. Following the constant  $\alpha$  contour in Figure 55, elements No. 209, 210, 317 and 354 are stress intensified while plugging continues. Figure 56 shows the resulting fracture path where plugging has extended through the front surface where elements No. 209 and 210 failed at  $t = 0.6500\mu\text{sec}$ . At this time, element No. 208 is still intact but is on the verge of being failed. The damage zone has spread to the mid-thickness except for element No. 347 as indicated in Figure 56. The corresponding constant  $\alpha$  contours are given in Figure 57 from which elements No. 353 and 390 are seen to be situated along the path of prospective plugging. At  $t = 0.6900\mu\text{sec}$ , plugging has penetrated more than one half of the target thickness as elements No. 317 and 354 fail. A cylindrically-shaped plug is formed as shown in Figure 58 where elements No. 208 and 381 are about to fail. The fracture path is directed along the constant  $\alpha$  contour No. (7) in Figure 59. Elements No. 353 and 390 are thus intensified. As the fracture path continues to extend by breaking elements No. 389 and 426 as shown in Figure 60 at  $t = 0.7340\mu\text{sec}$ , more elements are damaged. The reorientation of the damage plane is displayed in Figure 61. Again, contour No. (7) with  $\alpha = -31.16^\circ$  is directed almost normal to the target surface. This angle did not differ appreciably from that of contour No. (7) in Figure 59. Elements No. 425 and 462 are next intensified and fractured as time increases to  $0.8942\mu\text{sec}$ , Figure 62. Failure also occurred in element No. 242 at the top of the plug. The constant  $\alpha$  contours ahead of the fracture path in Figure 63 are now slightly slanted in line with elements No. 461 and 498. It is interesting to note that as compressive waves are reflected from the backside elements No. 453, 456, 457 and 460 leading ahead are first damaged while elements No. 418, 419, 422 and 423 further back are still undamaged,

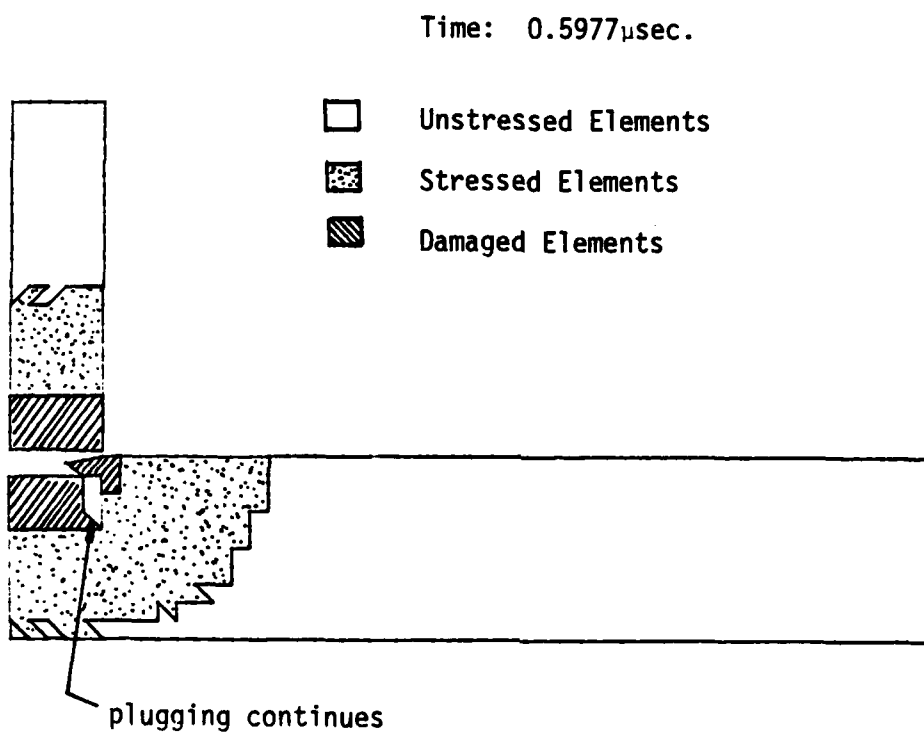


Figure 54. Projectile-target damage pattern after 0.5977 $\mu$ sec (Model II).

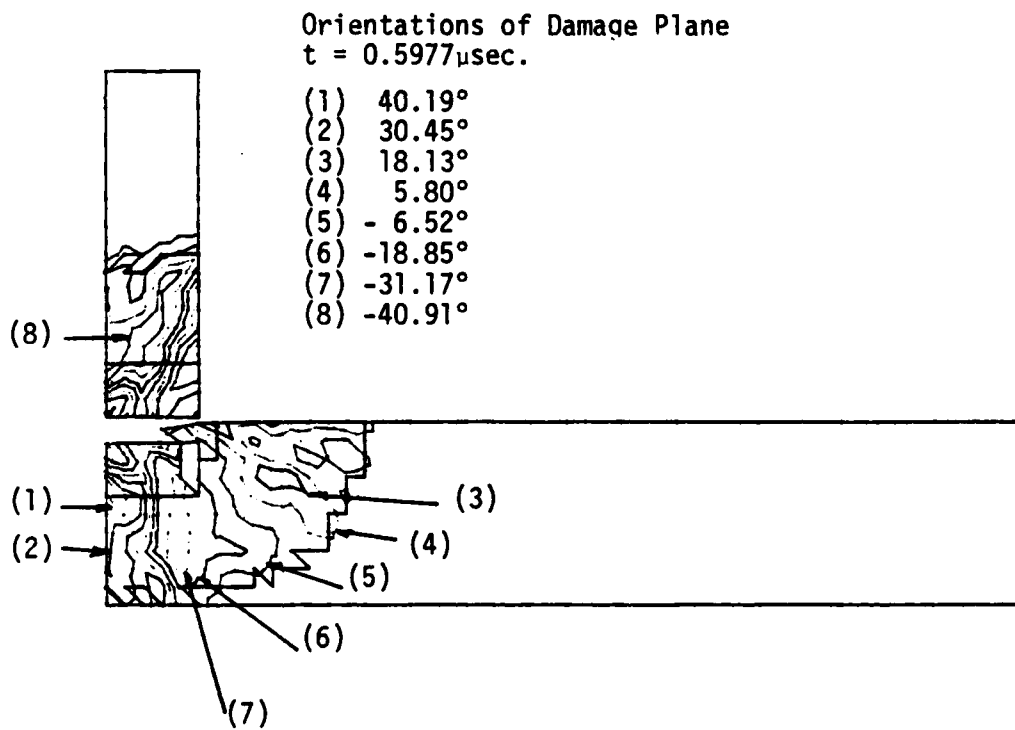


Figure 55. Constant  $\alpha$  contours after  $0.5977\mu\text{sec}$  (Model II).

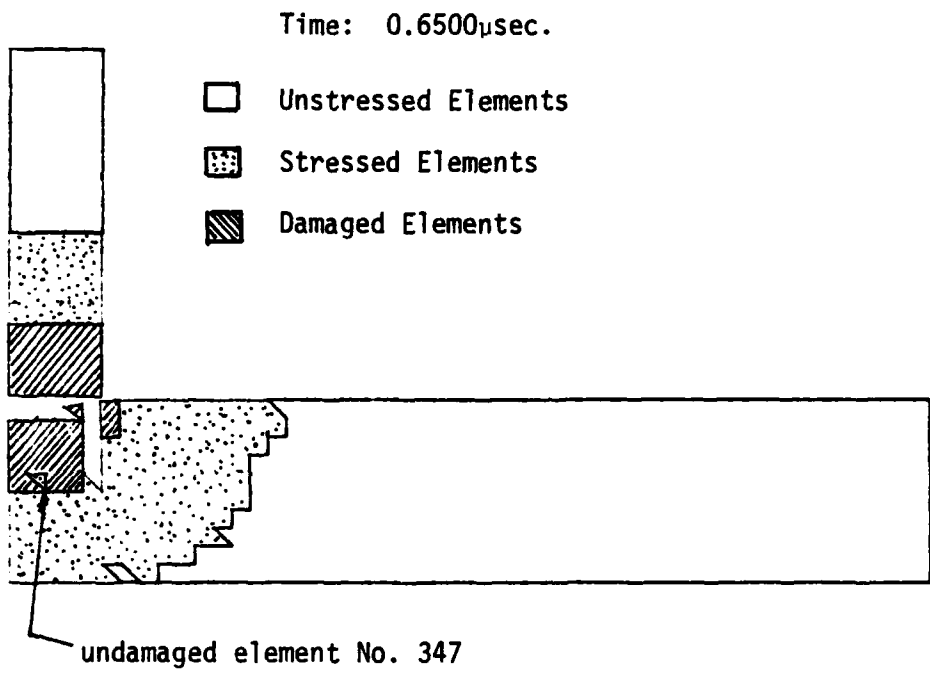


Figure 56. Projectile-target damage pattern after 0.6500 $\mu$ sec (Model II).

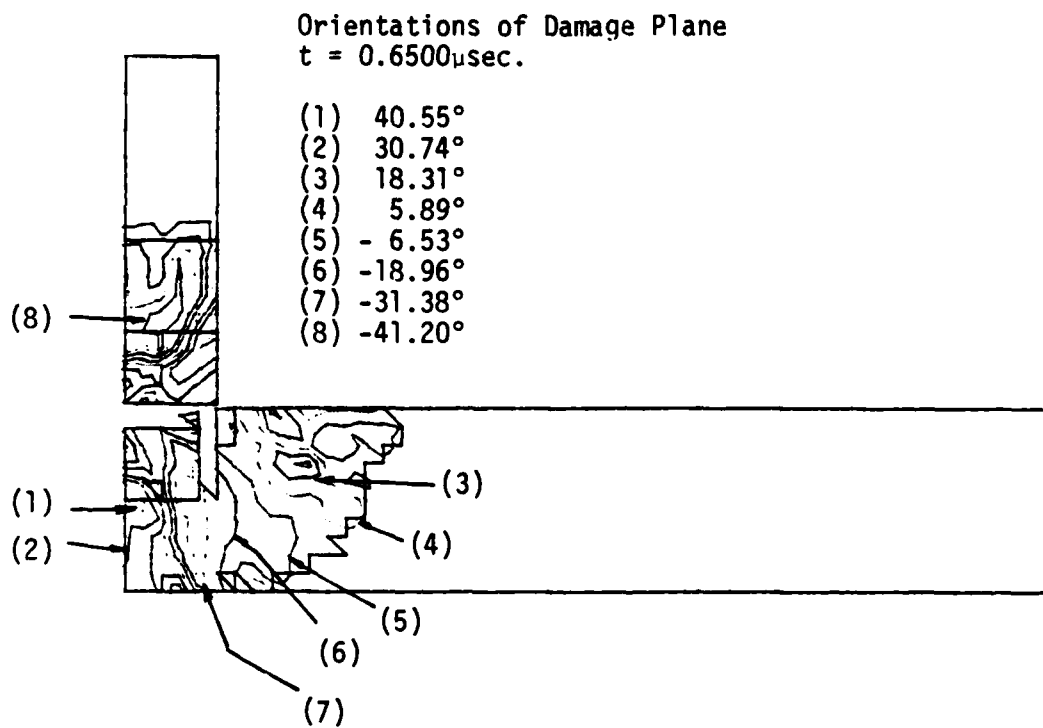


Figure 57. Constant  $\alpha$  contours after  $0.6500\mu\text{sec}$  (Model II).

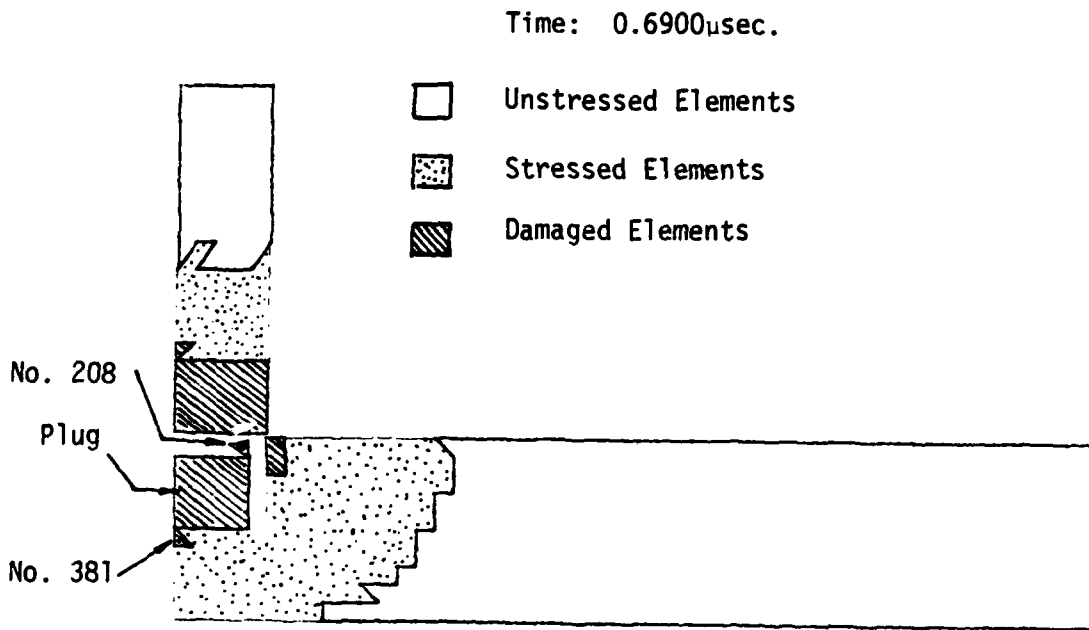


Figure 58. Projectile-target damage pattern after 0.6900 $\mu$ sec (Model II).

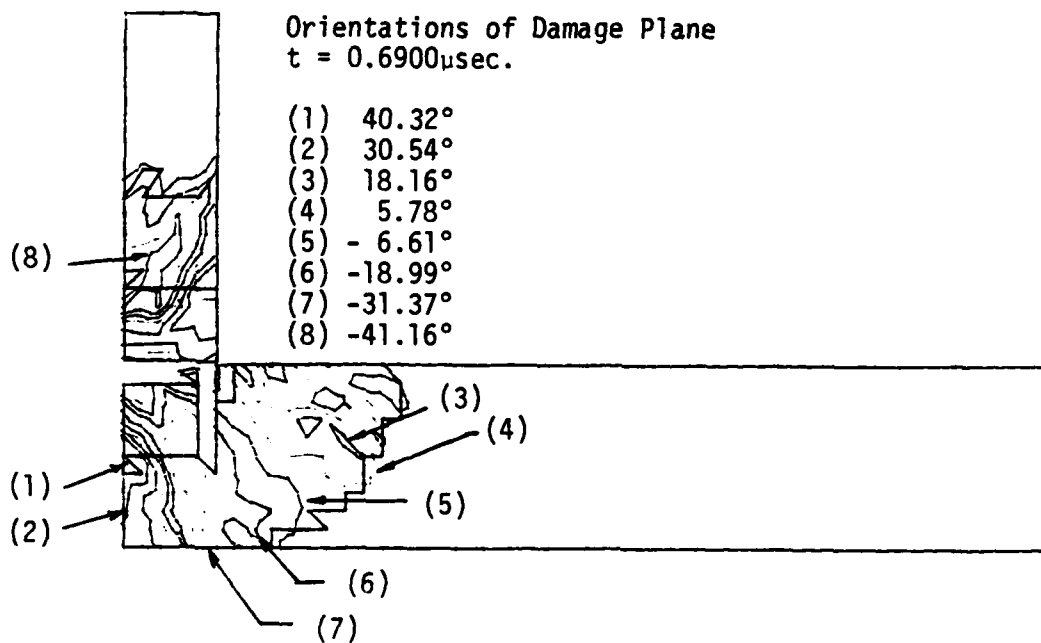


Figure 59. Constant  $\alpha$  contour after  $0.6900\mu\text{sec}$  (Model II).

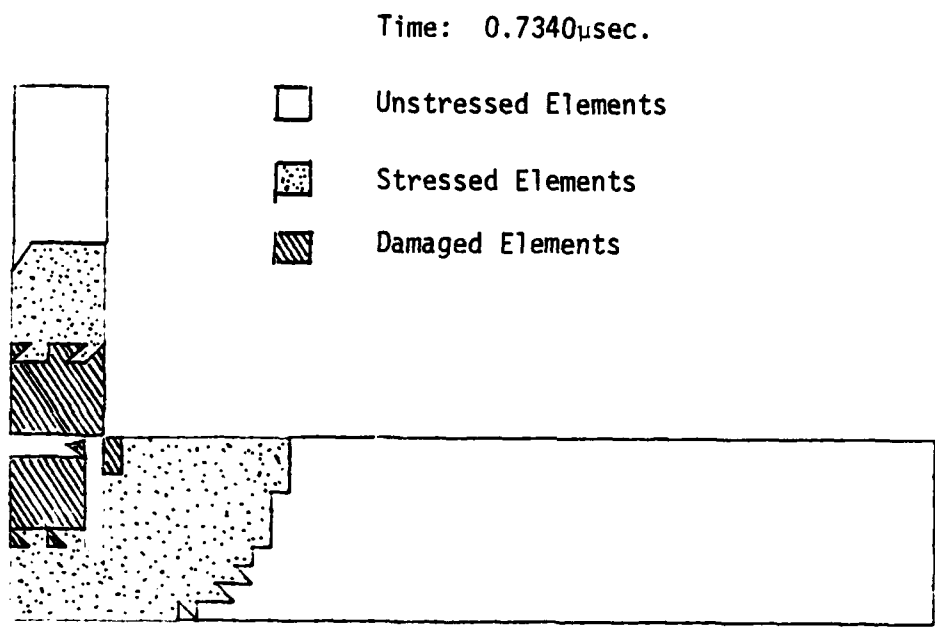


Figure 60. Projectile-target damage pattern after 0.7340 $\mu$ sec (Model II).

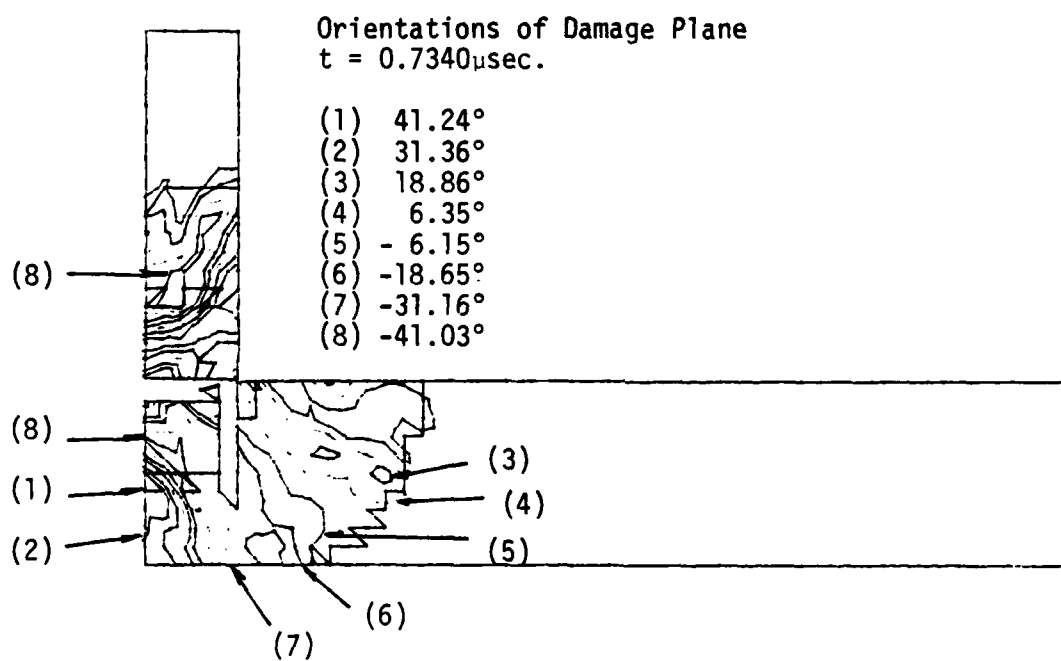


Figure 61. Constant  $\alpha$  contour after  $0.7340\mu\text{sec}$  (Model II).

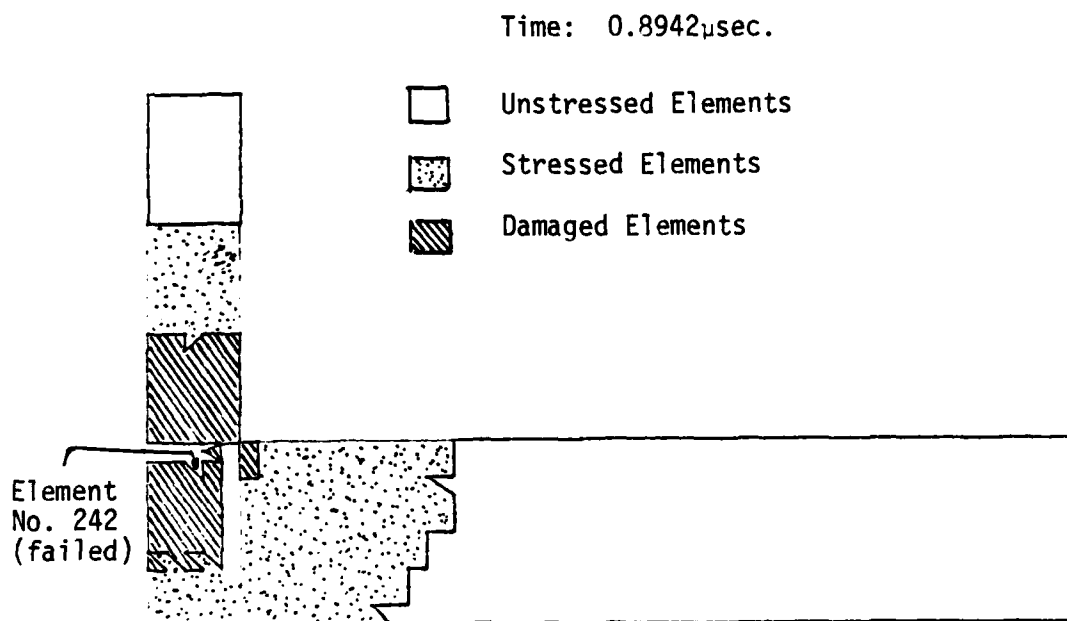


Figure 62. Projectile-target damage pattern after 0.8942 $\mu$ sec (Model II).

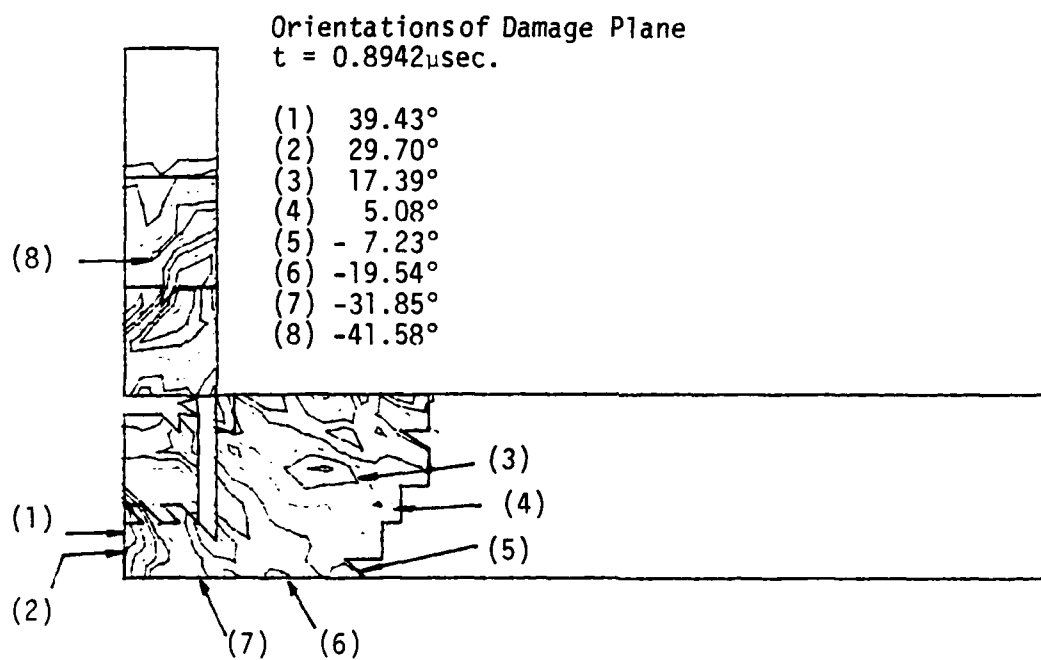


Figure 63. Constant  $\alpha$  contours after  $0.8942 \mu\text{sec}$  (Model II).

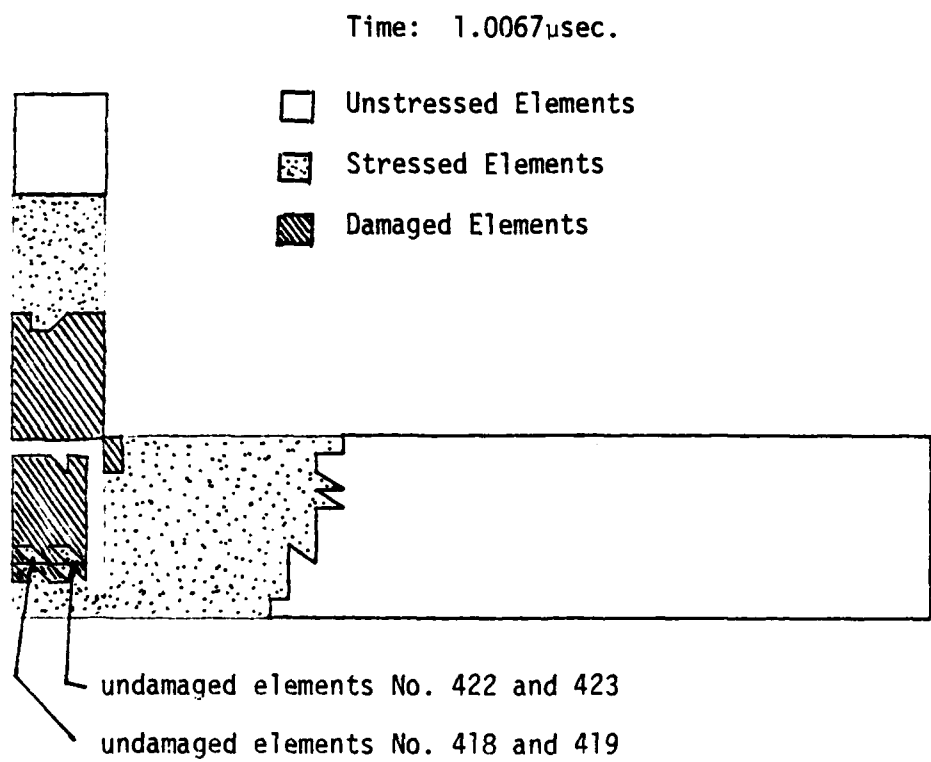


Figure 64. Projectile-target damage pattern after 1.0067 $\mu$ sec (Model II).

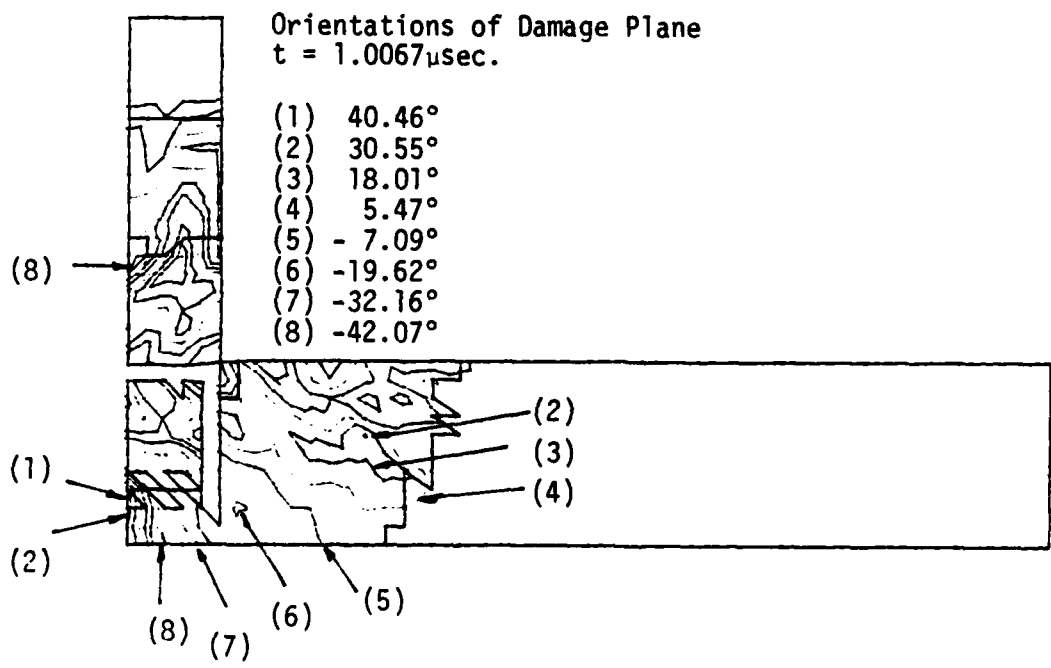


Figure 65. Constant  $\alpha$  contours after  $1.0067 \mu\text{sec}$  (Model II).

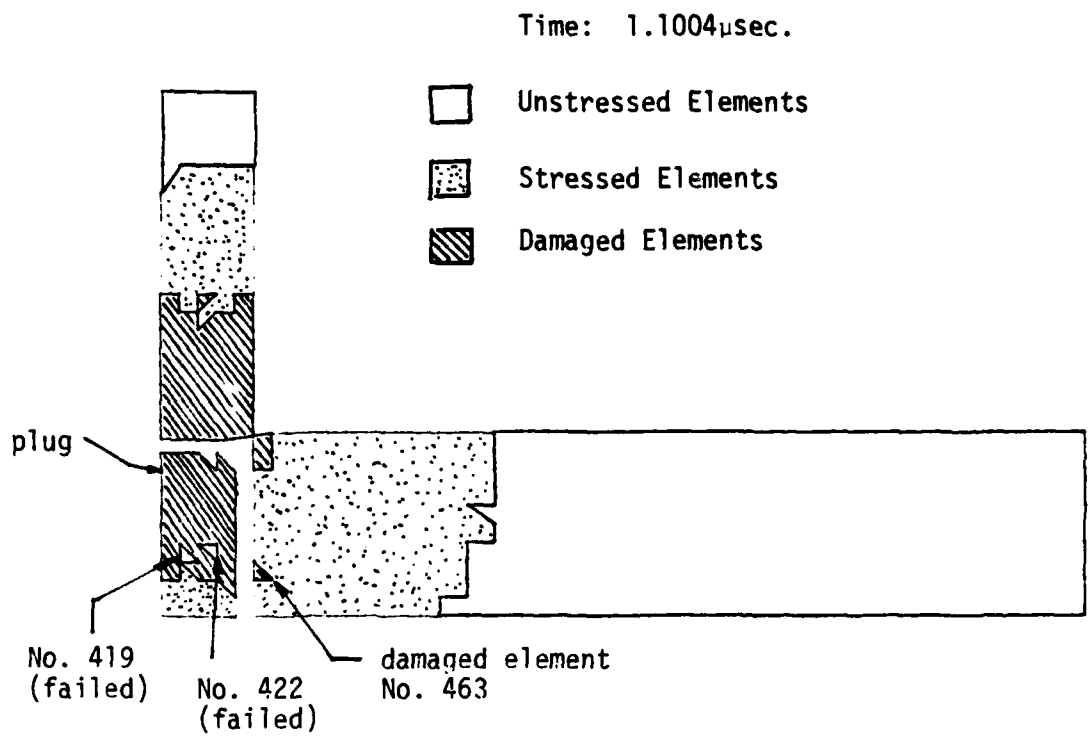


Figure 66. Projectile-target damage pattern after 1.1004 $\mu$ sec (Model II).

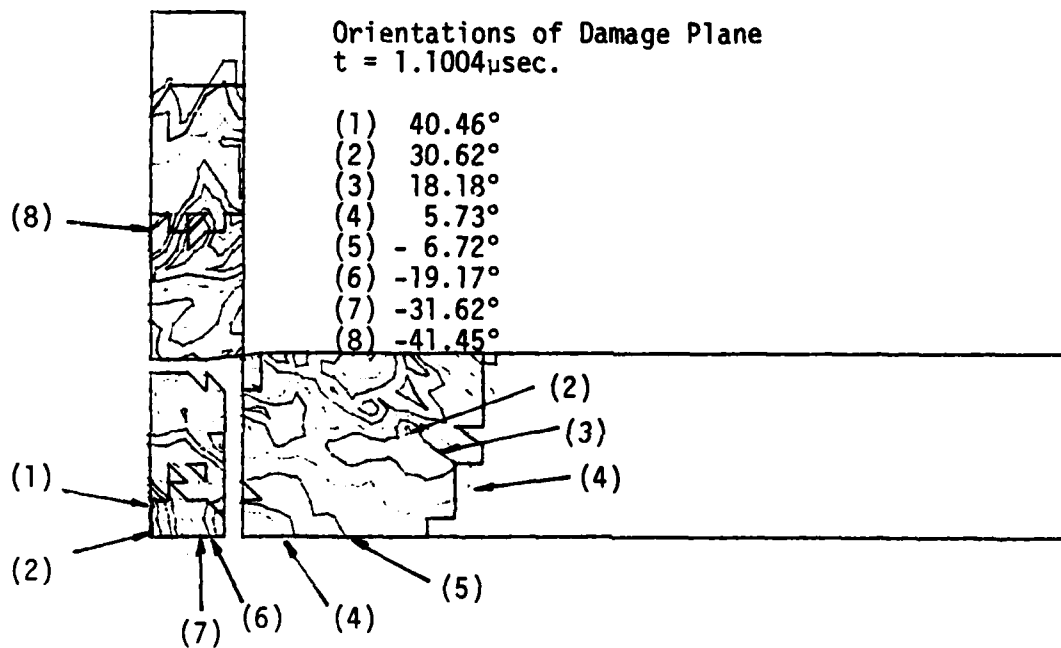


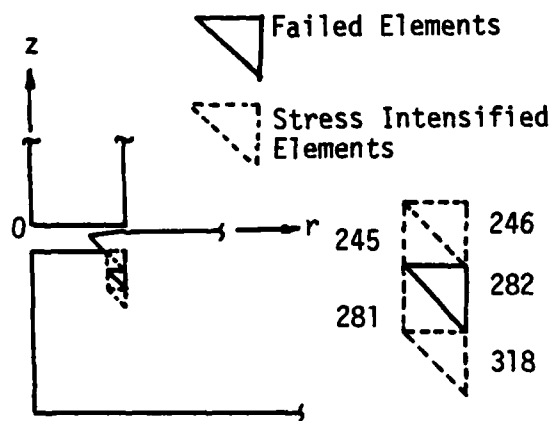
Figure 67. Constant  $\alpha$  contours after  $1.1004 \mu\text{sec}$  (Model II).

Figure 64. This exhibits the tendency of spallation. At this time, the majority of the constant  $\alpha$  contours in Figure 65 are aligned almost normal to the plate surface. The final stage of plugging is completed when elements No. 497, 534 and 533 fail at  $t = 1.1004\mu\text{sec}$ . Figure 66 shows that element No. 463 next to the fracture path is also damaged. The plug is dislocated from the target and is damaged both externally and internally. The failure of elements No. 419 and 422 inside the plug suggests fragmentation as the plug leaves the target with the exit velocity. Figure 67 summarizes the orientations of the residual damage planes in both the projectile, target and plug.

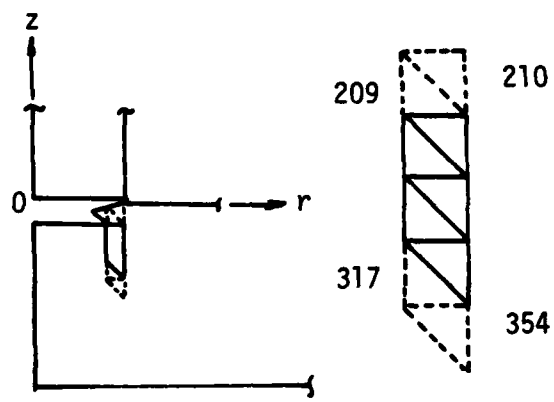
The sequence of events starting from plug initiation to dislocation is shown in eight (8) time steps as outlined in Figures 68(a) to 68(h). For the tougher material used in Model II, plug initiation started at a later time with  $t = 0.5345\mu\text{sec}$  as compared with  $t = 0.4432\mu\text{sec}$  for Model I in Figure 39(a). Moreover, the location was moved to an element directly under the corner of the projectile rather than at an outward radial distance. There were also significant differences in the damage and failure patterns of the projectile-target system prior to plug initiation. A glance at Figures 68 reveals that the plug experienced more damage in Model II. As a consequence, more time was also required for full perforation. Since both Model I and II contain several idealized assumptions, the results must be interpreted accordingly. Aside from the coarseness of the finite element mesh size, damping force\* were not included in the present analysis. This done purposely in order not to cloud the findings with any arbitrariness and/or artificial effects. It can be accounted for in future analyses where damping de-

---

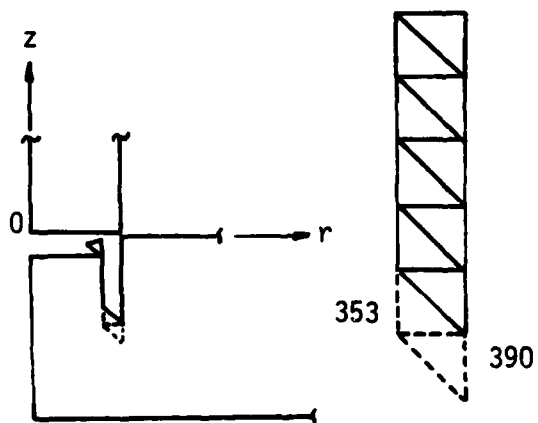
\*This is usually added into the computer scheme by introducing the so-called "artificial viscosity", a quantity that is not known and assumed arbitrarily.



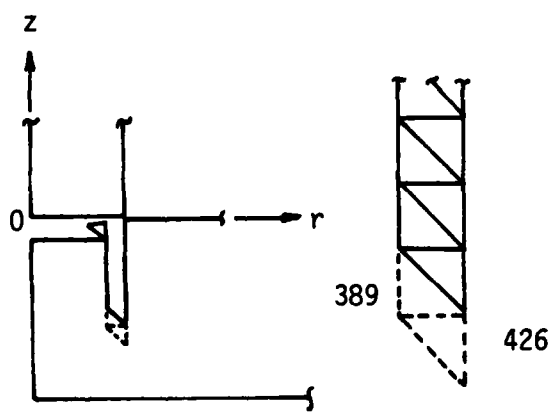
(a)  $t = 0.5345 \mu\text{sec}$



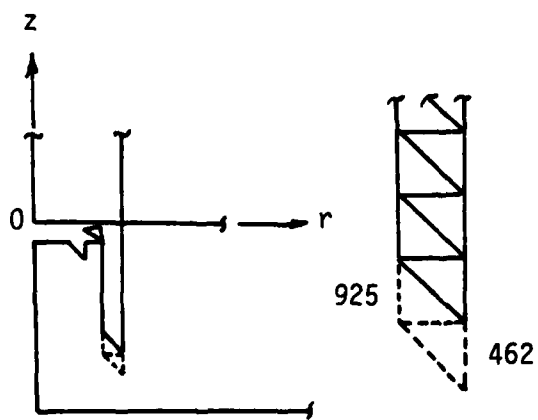
(b)  $t = 0.5977 \mu\text{sec}$



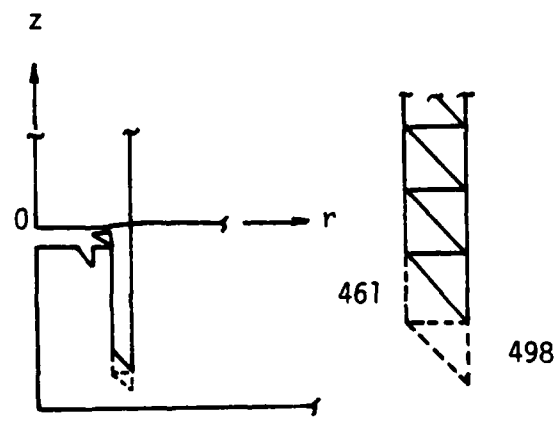
(c)  $t = 0.6500 \mu\text{sec}$



(d)  $t = 0.6900 \mu\text{sec}$



(e)  $t = 0.7340 \mu\text{sec}$



(f)  $t = 0.8942 \mu\text{sec}$

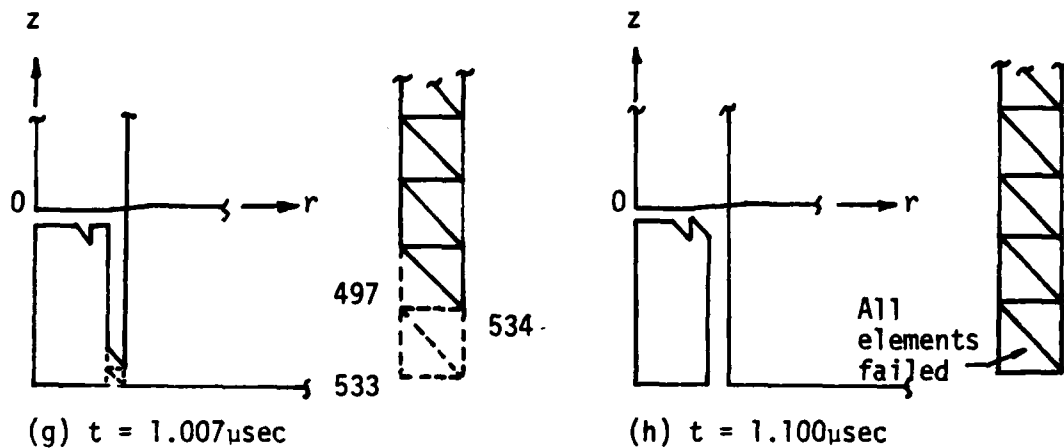


Figure 68. Sequence of plug formation.

depends on load history and varies nonhomogeneously in the system. The projectile velocity obviously becomes unrealistically high when this factor is ignored. Nevertheless, what has been achieved for the first time is an analytical demonstration of how uniaxial data affect the failure modes arising from projectile penetrations.

Summarized in Tables 21 to 24 are the time dependent stress components  $\sigma_z$ ,  $\sigma_r$ ,  $\sigma_\theta$  and  $\tau_{rz}$  for elements No. 151, 156, 160, 210, 211 and 248. These locations are chosen to illustrate the different degree of stress levels prior to failure. The corner element No. 160 of the projectile is most severely loaded at initial impact. This is seen in Figure 69 where the curve corresponds to the axial stress  $\sigma_z$  in element No. 160 which dropped sharply as it is intensified in compression. It then levels off before failure. Elements No. 151 and 156 that also come into contact with the target behaved in a similar fashion but failed at a later time. For those elements No. 210, 211 and 248 in the target, the axial stress  $\sigma_z$  attains an oscillatory character as they are damaged. The component  $\sigma_r$  in these same elements also varied appreciably with time and is shown in Figure 70. The trend, however,

Table 21. Axial Stress  $\sigma_z$  in ksi for Elements  
Near Contact (Model II)

Time ( $\mu$ sec)	Element No.					
	160	151	156	210	211	248
0.0200	-569.6	-366.9	-366.9	-167.2	-167.2	-
0.0420	-841.2	-753.2	-732.2	-353.2	-353.6	- 0.03
0.0928	-850.9	-814.6	-777.1	-634.7	-751.4	- 3.11
0.1543	-870.5	-827.6	-789.3	-643.0	-808.9	- 27.08
0.2287	<u>-892.8</u>	-840.5	-820.2	-527.7	-636.6	-121.66
0.2716	(failed)	-847.2	-826.9	-373.1	-558.2	-198.82
0.3188		-835.5	-853.0	-196.1	-371.3	-264.92
0.3643		-866.2	-860.1	- 51.6	-125.2	-268.66
0.4075		-890.9	-867.0	36.7	201.7	-204.02
0.4516		<u>-896.2</u>	<u>-875.4</u>	42.0	264.6	-104.7
		(failed)	(failed)			

Table 22. Radial Stress  $\sigma_r$  in ksi for Elements  
Near Contact (Model II)

Time ( $\mu$ sec)	Element No.					
	160	151	156	210	211	248
0.0200	0	0	0	0	0	-
0.0420	-151.1	-114.6	-130.6	- 43.5	- 46.3	- 0.18
0.0928	-153.5	-120.7	-164.0	-164.8	- 73.4	- 6.91
0.1543	-157.9	-129.7	-165.5	-236.7	-120.3	- 20.19
0.2287	<u>-164.5</u>	-132.0	-148.2	-233.0	- 51.5	- 70.00
0.2716	(failed)	-133.1	-148.8	-167.4	- 31.4	-138.08
0.3188		-152.8	-130.8	- 97.3	-166.9	-235.35
0.3643		-178.2	-131.5	- 48.8	-249.9	-286.53
0.4075		-160.4	-132.1	- 31.6	-326.9	-270.12
0.4516		<u>-161.0</u>	<u>-133.1</u>	- 63.4	-175.4	-173.71
		(failed)	(failed)			

Table 23. Circumferential Stress  $\sigma_{\theta}$  in ksi for  
Elements Near Contact (Model II)

Time ( $\mu$ sec)	Element No.					
	160	151	156	210	211	248
0.0200	0	0	0	0	0	-
0.0420	0.03	- 0.92	- 0.21	0.29	0.39	0.21
0.0928	0.51	- 13.27	- 2.72	2.93	3.94	2.71
0.1543	1.00	- 42.65	- 9.65	8.03	13.24	10.48
0.2287	<u>-2.07</u>	- 81.64	-23.66	11.73	25.89	19.72
0.2716	(failed)	-100.91	-34.33	9.46	28.66	34.42
0.3188		-122.70	-47.53	1.53	25.46	44.45
0.3643		-143.73	-61.36	-12.59	16.65	52.68
0.4075		-158.83	-75.33	-33.26	2.48	57.27
0.4516		<u>-158.97</u>	<u>-86.83</u>	-58.37	-16.13	55.33
		(failed)	(failed)			

Table 24. Shear Stress in  $\tau_{rz}$  ksi for  
Elements Near Contact (Model II)

Time ( $\mu$ sec)	Element No.					
	160	151	156	210	211	248
0.0200	87.0	0	0	85.7	0	-
0.0420	117.7	1.34	0.09	176.3	2.8	3.2
0.0928	120.3	6.87	0.01	271.3	32.4	40.2
0.1543	129.1	12.70	- 0.05	300.7	95.8	151.4
0.2287	<u>143.4</u>	15.82	0.69	335.9	170.5	298.5
0.2716	(failed)	15.46	1.44	354.2	210.2	336.6
0.3188		13.21	2.95	367.8	135.4	319.2
0.3643		11.39	4.80	373.5	- 19.5	303.7
0.4075		9.11	5.81	374.0	-235.1	305.6
0.4516		<u>5.42</u>	<u>10.65</u>	373.4	-289.2	265.9
		(failed)	(failed)			

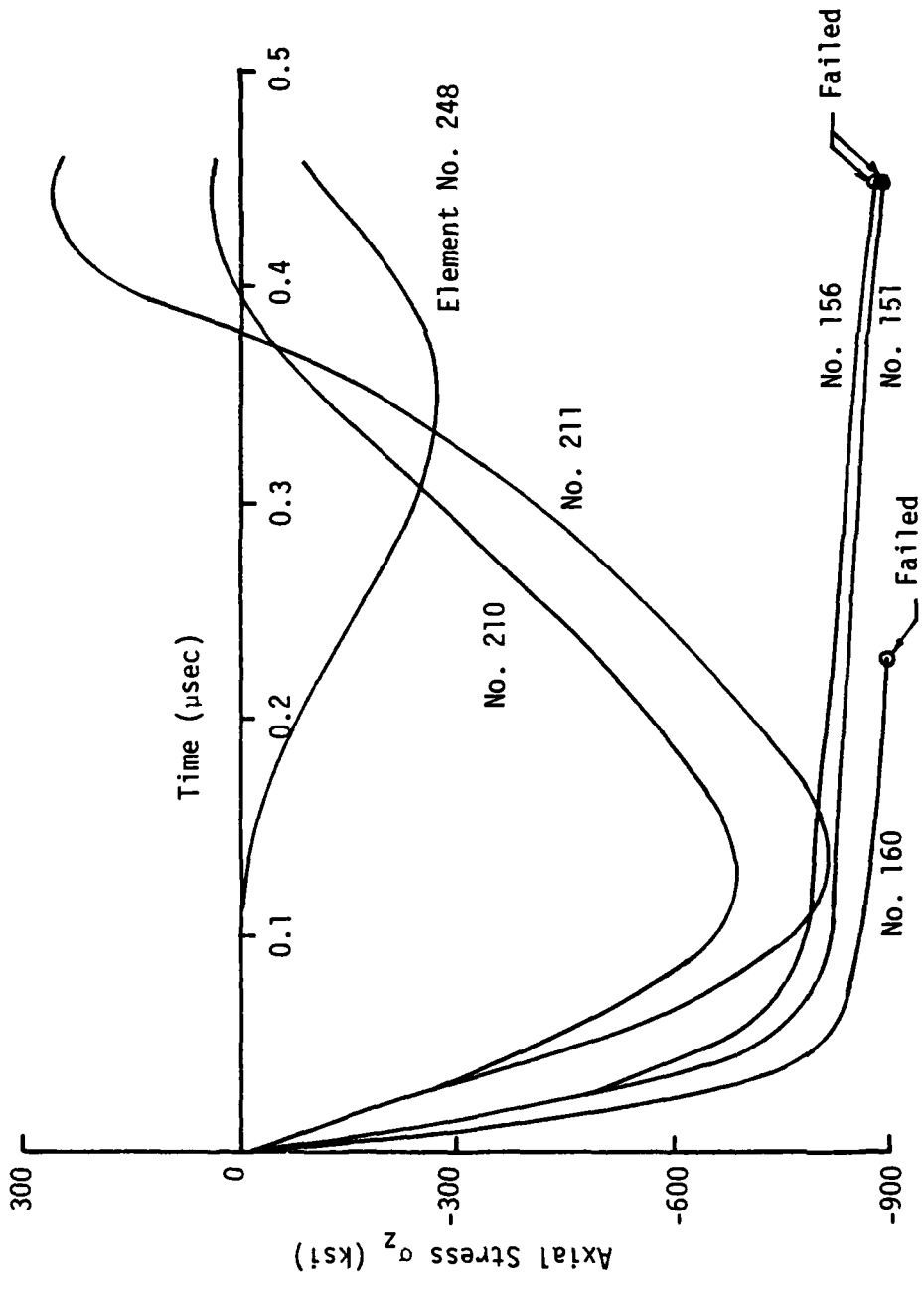


Figure 69. Variations of axial stress with time in elements No. 161, 156, 160, 210, 211 and 248 for Model II.

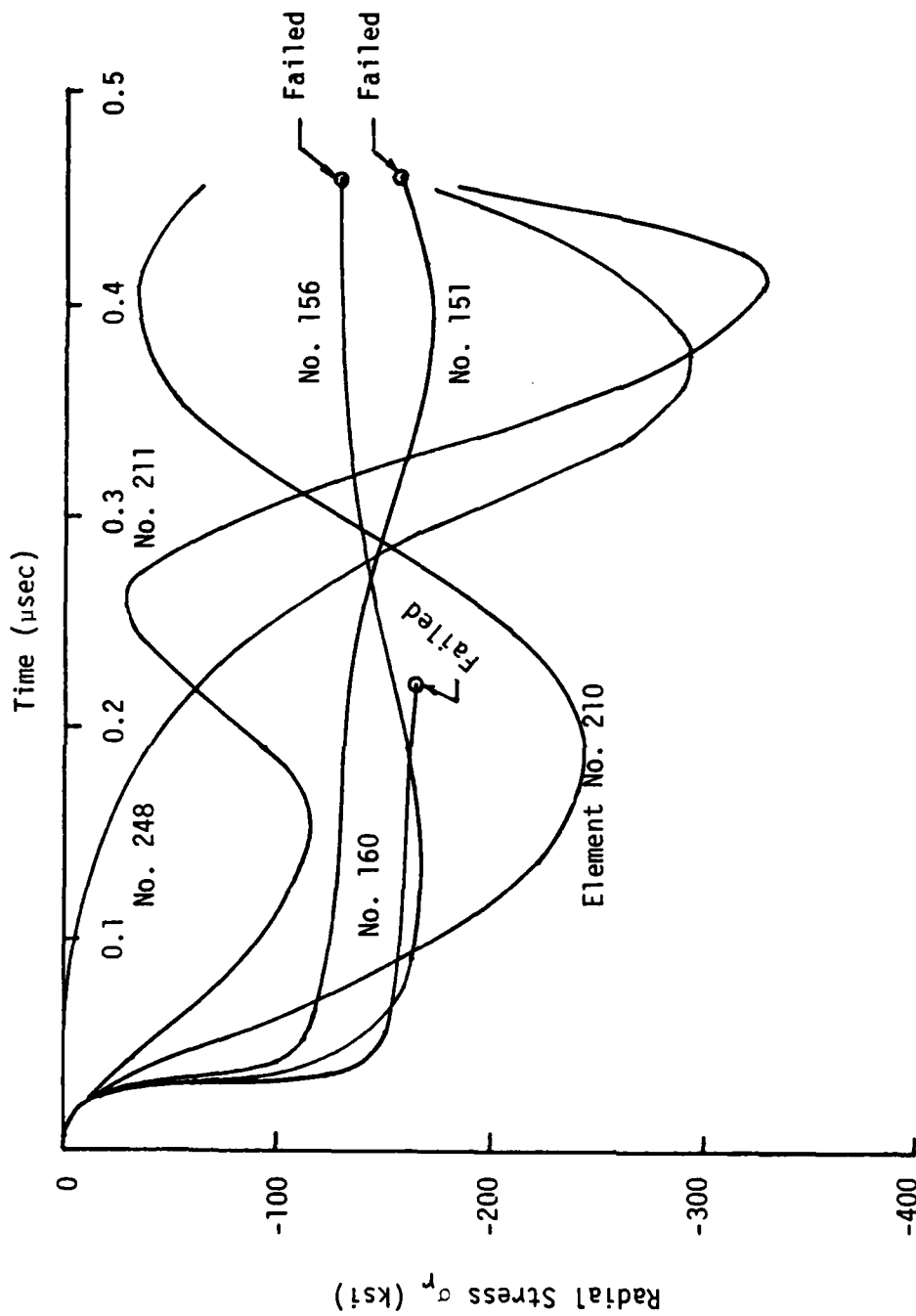


Figure 70. Variations of radial stress with time in elements No. 161, 156, 160, 210, 211 and 248 for Model II.

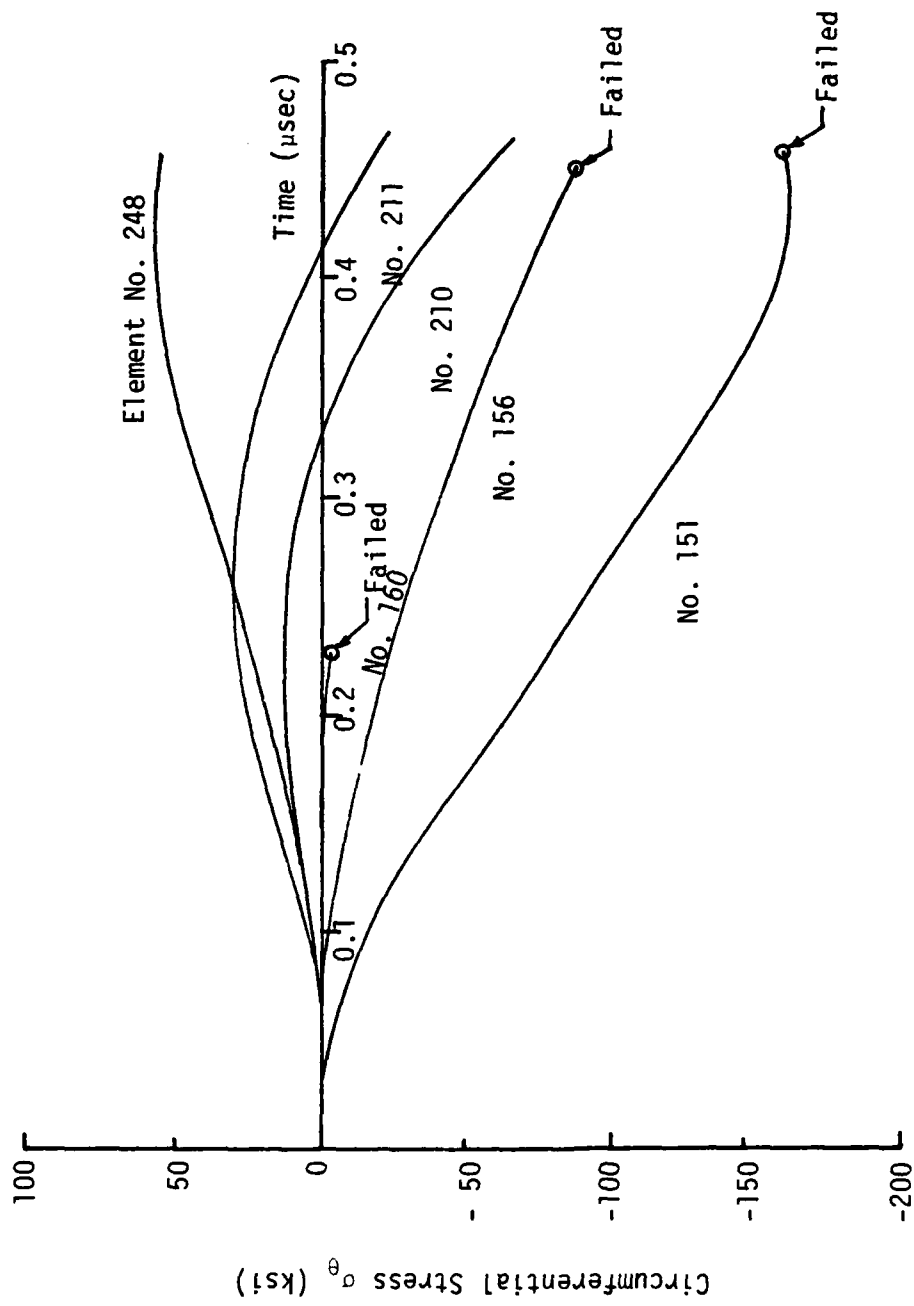


Figure 71. Variations of circumferential stress with time in elements No. 161, 156, 160, 210, 211 and 248 for Model II.

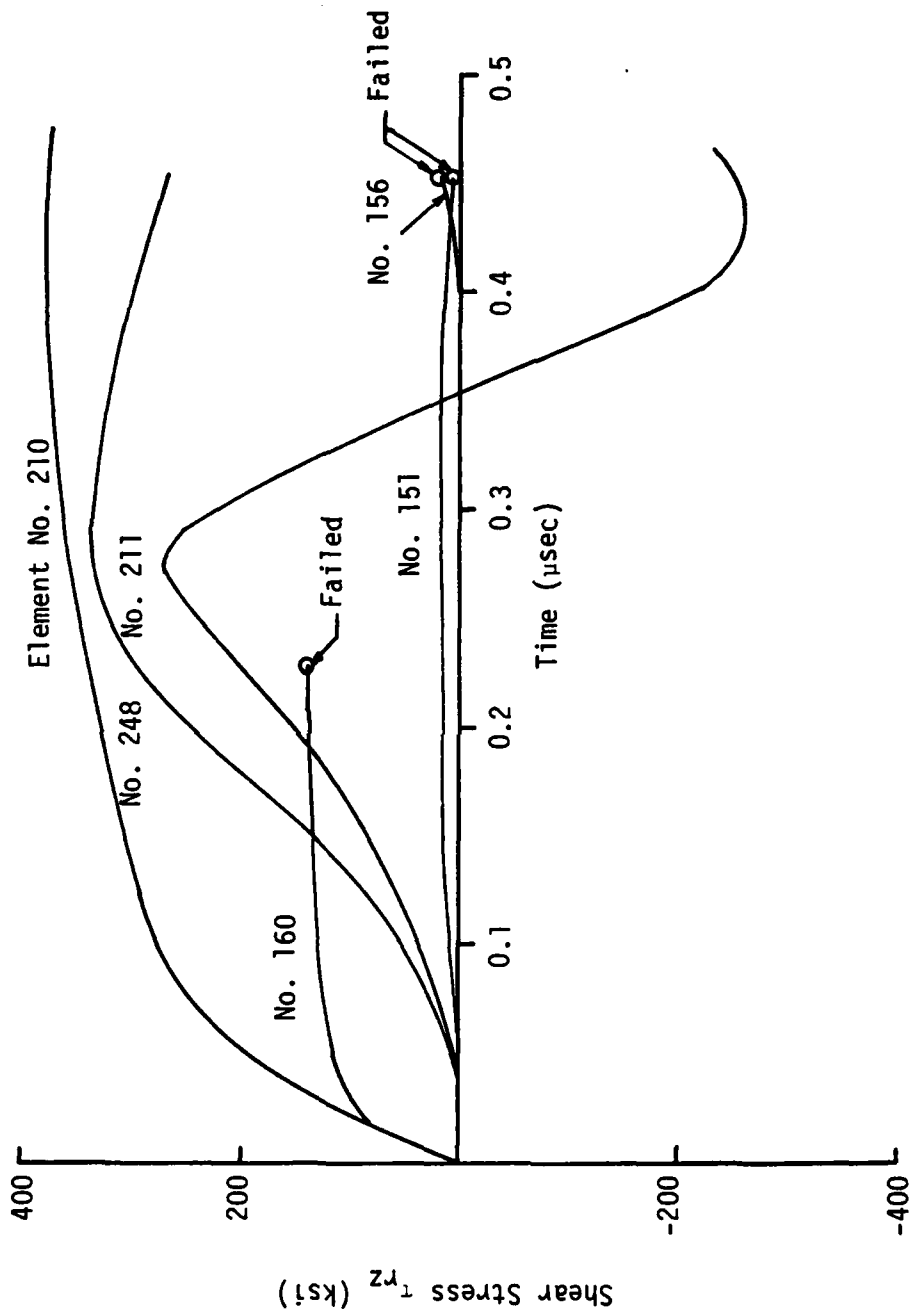


Figure 72. Variations of shear stress with time in elements No. 161, 156, 160, 210, 211 and 248 for Model II.

is similar to  $\sigma_z$  except for the curves corresponding to elements No. 151 and 156. They oscillated slightly with time. As a result of axisymmetry, the change in the circumferential direction is expected to be relatively small. Figure 71 shows that  $\sigma_\theta$  varied only slightly with time. Similar results for the shear stress component  $\tau_{rz}$  is given in Figure 72.

The nonuniform strain rates at the different locations can be evidenced from the data in Tables 25 to 28 for the  $\dot{\epsilon}_z$ ,  $\dot{\epsilon}_r$ ,  $\dot{\epsilon}_\theta$  and  $\dot{\epsilon}_{rz}$ . They vary from  $10^6 \text{ sec}^{-1}$  to  $10^2 \text{ sec}^{-1}$  and change from one location to another. It is clearly seen that the strain rate variations in element No. 160 are the largest as it fails first. The changes in element No. 248 that are further away from the initial impact are not as appreciable.

#### NONHOMOGENEOUS ENERGY DENSITY DISSIPATION RATE

It cannot be overemphasized that the failure behavior of all materials are intimately associated with the rates at which energy is dissipated per unit volume or unit area. For problems that involve a wide range of time scale, both quantities  $dV/dA$  and  $dW/dV$  can be equally important. Plug initiation was found to occur at locations of very high  $dV/dA$  whereas  $dW/dV$  was relatively low comparing with those in the neighboring elements. This is indicative of the rate effect being proportional to the slope of the uniaxial stress and strain curve that is related to  $dV/dA$ . When the loading rates are very low such as those experienced in creep deformation, changes in  $dV/dA$  are small and the rates of energy dissipation are governed mostly by  $dW/dV$ . In general, the corollary of the strain energy density theory [4] as stated by equation (3) provides a more consistent treatment since no a priori assumption is made on the form or nature of the constitutive relations. This is why conceptual difficulties often arise when applying the  $dW/dV$  criterion

Table 25. Axial Strain Rate  $\dot{\epsilon}_z$  ( $\times 10^3 \text{ sec}^{-1}$ )  
for Elements Near Contact (Model II)

Time ( $\mu\text{sec}$ )	Element No.			
	160	151	210	248
0.0200	-1,073.2	-691.2	-314.9	-
0.0420	-1,049.4	-684.9	-319.3	- 0.01
0.0928	- 994.6	-623.9	-248.1	- 2.72
0.1543	-1,037.8	-548.2	- 65.0	-19.0
0.2287	<u>-1,170.5</u>	-489.3	76.4	-54.0
0.2716	(failed)	-471.1	171.4	-61.6
0.3188		-457.0	223.7	-44.1
0.3643		-444.6	234.5	44.5
0.4075		-421.7	190.2	51.8
0.4516		<u>-397.0</u>	88.9	75.6
		(failed)		

Table 26. Radial Strain Rate  $\dot{\epsilon}_r$  ( $\times 10^3 \text{ sec}^{-1}$ )  
for Elements Near Contact (Model II)

Time ( $\mu\text{sec}$ )	Element No.			
	160	151	210	248
0.0200	0	0	0	-
0.0420	4.68	- 1.40	4.56	- 0.31
0.0928	12.83	-10.35	12.75	- 8.38
0.1543	32.14	-17.06	32.77	- 4.94
0.2287	<u>29.22</u>	-17.04	37.40	-27.65
0.2716	(failed)	-14.98	- 0.15	-51.33
0.3188		-15.40	- 49.01	-71.36
0.3643		-15.37	- 93.48	-44.63
0.4075		-11.04	-113.10	7.49
0.4516		<u>- 0.11</u>	-108.93	72.77
		(failed)		

Table 27. Circumferential Strain Rate  $\dot{\epsilon}_\theta$  ( $\times 10^3 \text{ sec}^{-1}$ )  
for Elements Near Contact (Model II)

Time ( $\mu\text{sec}$ )	Element No.			
	160	151	210	248
0.0200	0	0	0	-
0.0420	0.042	- 1.395	0.439	0.322
0.0928	0.357	-10.350	2.192	2.197
0.1543	0.160	-17.060	2.782	4.847
0.2287	<u>-2.088</u>	-17.040	1.128	6.933
0.2716	(failed)	-14.980	- 1.762	7.359
0.3188		-15.400	- 5.608	7.089
0.3643		-15.370	-10.320	6.011
0.4075		-11.040	-15.110	3.359
0.4516		<u>- 0.106</u> (failed)	-19.040	-1.471

Table 28. Shear Strain Rate  $\dot{\epsilon}_{rz}$  ( $\times 10^3 \text{ sec}^{-1}$ )  
for Elements Near Contact (Model II)

Time ( $\mu\text{sec}$ )	Element No.			
	160	151	210	248
0.0200	188.4	0	185.6	-
0.0420	180.2	2.75	178.6	6.2
0.0928	176.9	13.34	166.2	42.0
0.1543	214.4	19.02	181.9	88.4
0.2287	<u>280.8</u>	15.22	179.5	78.2
0.2716	(failed)	7.78	188.6	44.6
0.3188		1.25	186.4	4.3
0.3643		- 3.38	192.4	-14.7
0.4075		-11.96	148.5	-24.9
0.4516		<u>-21.38</u>	114.4	-39.1
		(failed)		

in conjunction with the theory of plasticity. The yield condition of von Mises considers only the distortional component of  $dW/dV$  while the relative maximum of  $dW/dV$  that is assumed to coincide with locations of excessive distortion also includes the dilatational component of  $dW/dV$ . Such a conflict will always prevail if the failure or damage criterion is not inherently embedded in the stress\* or strain analysis.

To illustrate the nonhomogeneous character of  $dW/dV$  and  $dW/dA$ , elements No. 15, 152, 160, 210, 211 and 248 are selected with their variations as a function of time given in Tables 29 and 30 for Model I. Because of the brittle-like failure behavior, most of the energies are dissipated in terms of failure by fracture. Displayed in Figures 73 and 74 are respectively the time dependent character of  $dW/dV$  and  $dW/dA$ . The curves for elements No. 151, 156, 160, 210 and 211 all rise very sharply up to the point of failure except for element No. 248 that follows a much more gradual change. Since both the variations of  $dW/dV$  and  $dW/dA$  with time are very similar, the influence of  $dV/dA$  is seen to be small. Significant change in  $dV/dA$  occurred only at plug initiation.

Tables 31 to 33 outline the results on energy density as a function of time for Model II. Again, the difference between  $dW/dV$  and  $dW/dA$  shown in Figures 75 and 76 is small as  $dV/dA$  in general remained fairly constant except at the time of plug initiation. The curves for elements No. 151, 156 and 160 in Figures 75 and 76 increased monotonically with time while those for elements No. 211 and 248 achieved oscillation. This is because both  $dW/dV$  and  $dW/dA$  contain both elastic and dissipated energy. The elastic portion can increase or decrease with time depending on wave propagation. The dissipated portion of  $dW/dV$  or  $(dW/dV)_p$ , however, must al-

\* Stress analysis is a misnomer in the strain energy density theory because the method determines the stress distribution via the quantity  $dV/dA$  and uniaxial data.

Table 29. Strain Energy Density Function  $dW/dV$   
in psi for Elements Near Contact  
(Model I)

Time ( $\mu$ sec)	Element No.					
	160	151	152 to 156	210	211	248
0.0050	390	155	155	52	33	-
0.0105	1,725	686	686	231	144	0
0.0166	4,289	1,708	1,705	573	359	0
0.0232	8,415	3,357	3,346	1,127	708	0
0.0305	<u>14,470</u>	6,297	6,177	1,946	1,230	0.1
0.0331	(failed)	<u>7,600</u>	7,414	2,291	1,451	0.1
0.0464		(failed)	<u>14,760</u>	4,400	2,340	1.2
0.0611			(failed)	7,295	4,861	6.3
0.0772				<u>10,810</u>	7,294	24.8
0.0949				(failed)	<u>9,247</u>	70.9
0.1144					(failed)	142.8
0.1358						233.2
0.1594						324.5
0.1853						391.2
0.2138						412.1
0.2452						394.4
0.2798						387.9
0.3177						460.0
0.3595						632.2
0.4015						821.5
0.4435						<u>967.6</u> (failed)

Table 30. Strain Energy Per Unit Area  $dW/dA$  in  
lb/in for Elements Near Contact  
(Model I)

Time ( $\mu$ sec)	Element No.					
	160	151	152 to 156	210	211	248
0.0050	956	439	439	111	92	-
0.0105	4,299	1,940	1,940	492	407	0
0.0166	10,520	4,827	4,821	1,223	1,014	0
0.0232	20,640	9,483	9,458	2,403	1,996	0
0.0305	<u>35,520</u>	17,770	17,450	4,156	3,461	0
0.0331	(failed)	<u>21,450</u>	20,940	4,895	4,079	0
0.0464		(failed)	<u>41,710</u>	9,382	7,671	1.3
0.0611			(failed)	15,480	13,530	7.9
0.0772				<u>22,760</u>	20,150	92.8
0.0949				(failed)	<u>25,280</u>	178.7
0.1144					(failed)	351.8
0.1358						580.5
0.1594						821.4
0.1853						999.4
0.2138						1,051.7
0.2452						1,010.6
0.2798						1,049.1
0.3177						1,460.6
0.3595						1,854.5
0.4015						2,224.9
0.4435						<u>2,514.7</u>
						(failed)

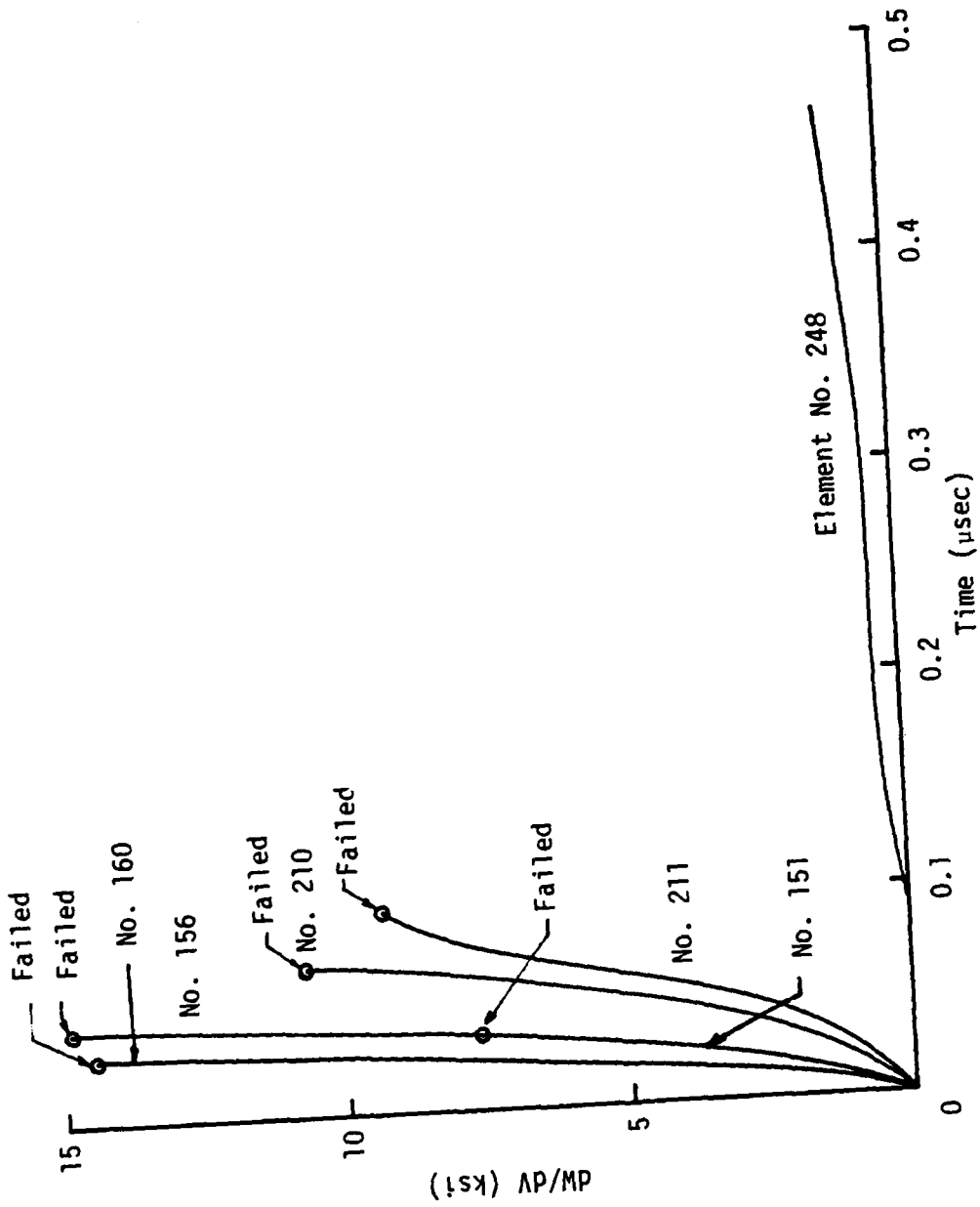


Figure 73. Variations of strain energy density function  $dW/dV$  with time for elements in Model I.

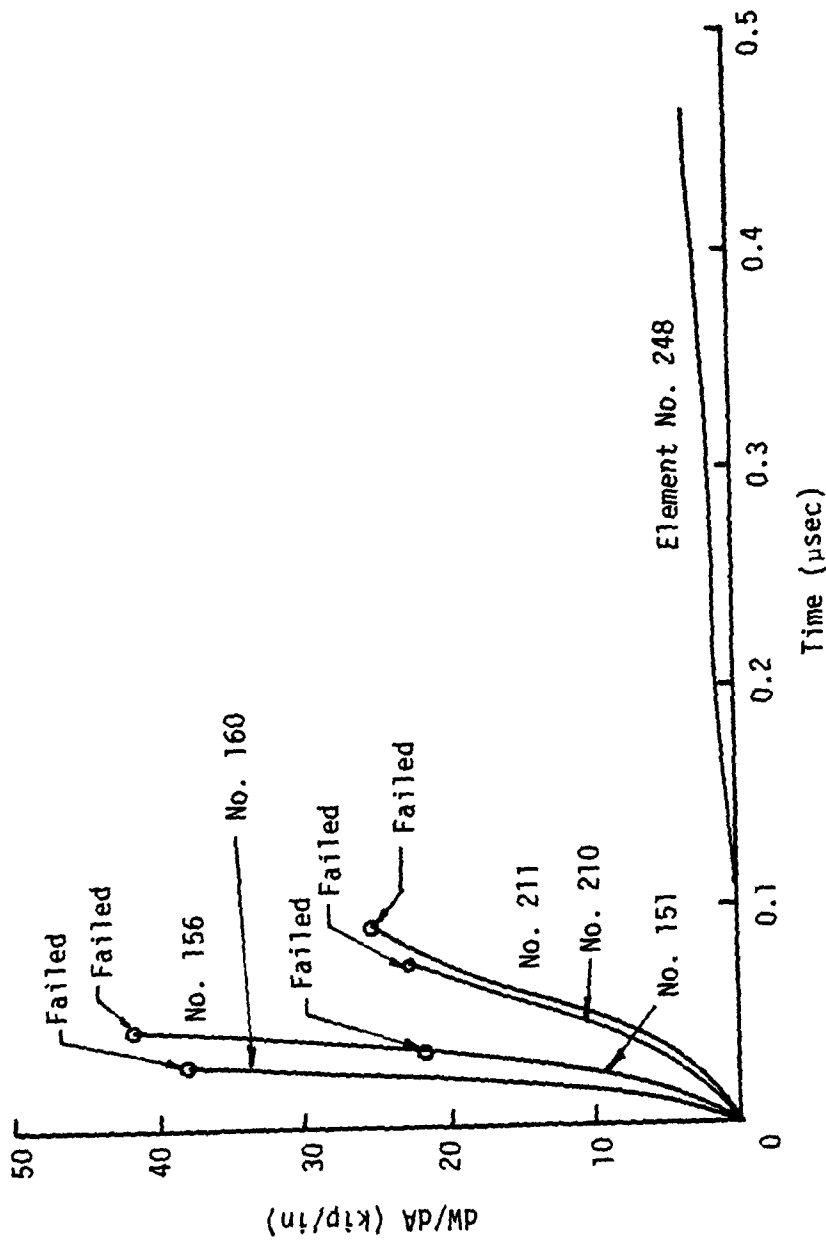


Figure 74. Variations of energy density per unit area  $dW/dA$  with time for elements in Model I.

Table 31. Strain Energy Density Function  $dW/dV$   
in psi for Elements Near Contact  
(Model II)

Time ( $\mu$ sec)	Element No.					
	160	151	156	210	211	248
0.0200	6.4	2.5	2.5	0.84	0.53	-
0.0420	23.4	11.0	10.7	3.70	2.36	-0
0.0928	68.2	36.9	34.6	15.06	10.74	0.07
0.1543	125.2	65.7	60.1	25.44	16.60	1.01
0.2287	<u>204.5</u>	97.0	88.5	31.25	15.16	4.21
0.2716	(failed)	114.2	105.2	33.52	10.75	6.08
0.3188		132.5	124.5	37.17	5.14	7.34
0.3643		150.0	144.0	42.66	2.48	7.41
0.4075		167.0	163.8	47.88	3.83	6.07
0.4516		<u>182.6</u>	<u>189.2</u>	52.06	5.32	3.86
		(failed)	(failed)			

Table 32. Strain Energy Per Unit Area  $dW/dA$   
in kip/in for Elements Near Contact  
(Model II)

Time ( $\mu$ sec)	Element No.					
	160	151	156	210	211	248
0.0200	15.8	7.2	7.2	1.80	1.49	-
0.0420	57.5	31.0	30.4	7.9	6.6	-0
0.0928	167.6	102.7	97.8	32.3	29.2	0.2
0.1543	305.8	180.0	169.3	53.7	42.2	2.8
0.2287	<u>494.7</u>	263.3	248.6	64.9	36.0	9.9
0.2716	(failed)	309.7	294.7	68.9	24.8	13.7
0.3188		359.7	347.5	74.9	11.3	16.3
0.3643		407.8	400.3	76.8	6.4	16.6
0.4075		455.9	454.4	44.0	8.6	14.1
0.4516		<u>501.8</u>	<u>521.2</u>	60.3	16.1	10.3
		(failed)	(failed)			

Table 33. Dissipated Strain Energy Density Function  $(dW/dV)_p$   
in ksi for Elements Near Contact (Model II)

Time ( $\mu$ sec)	Element No.					
	160	151	156	210	211	248
0.0200	0	0	0	0	0	-
0.0420	11.5	0.4	0.8	0	0	0
0.0928	55.7	24.9	23.6	4.20	2.108	0
0.1543	111.9	53.2	48.7	13.31	3.195	0
0.2287	<u>190.3</u>	84.0	78.0	20.62	4.811	0
0.2716	(failed)	100.9	94.1	25.23	4.811	0.176
0.3188		117.1	115.1	30.56	4.811	0.776
0.3643		137.2	134.3	36.63	4.811	0.776
0.4075		156.6	153.9	41.86	4.811	0.776
0.4516		<u>172.0</u>	<u>178.9</u>	45.95	4.811	0.776
		(failed)	(failed)			

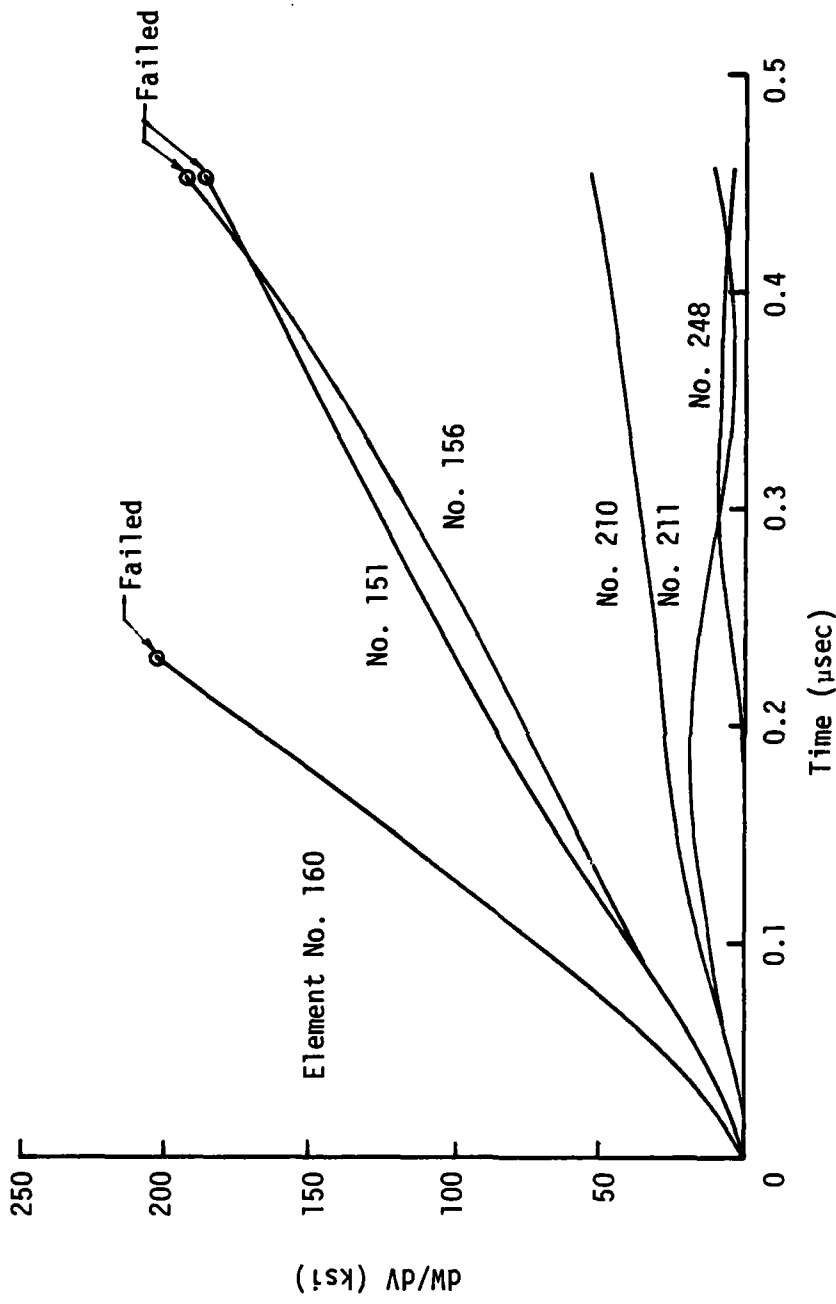


Figure 75. Variations of strain energy density function with time for elements in Model II.

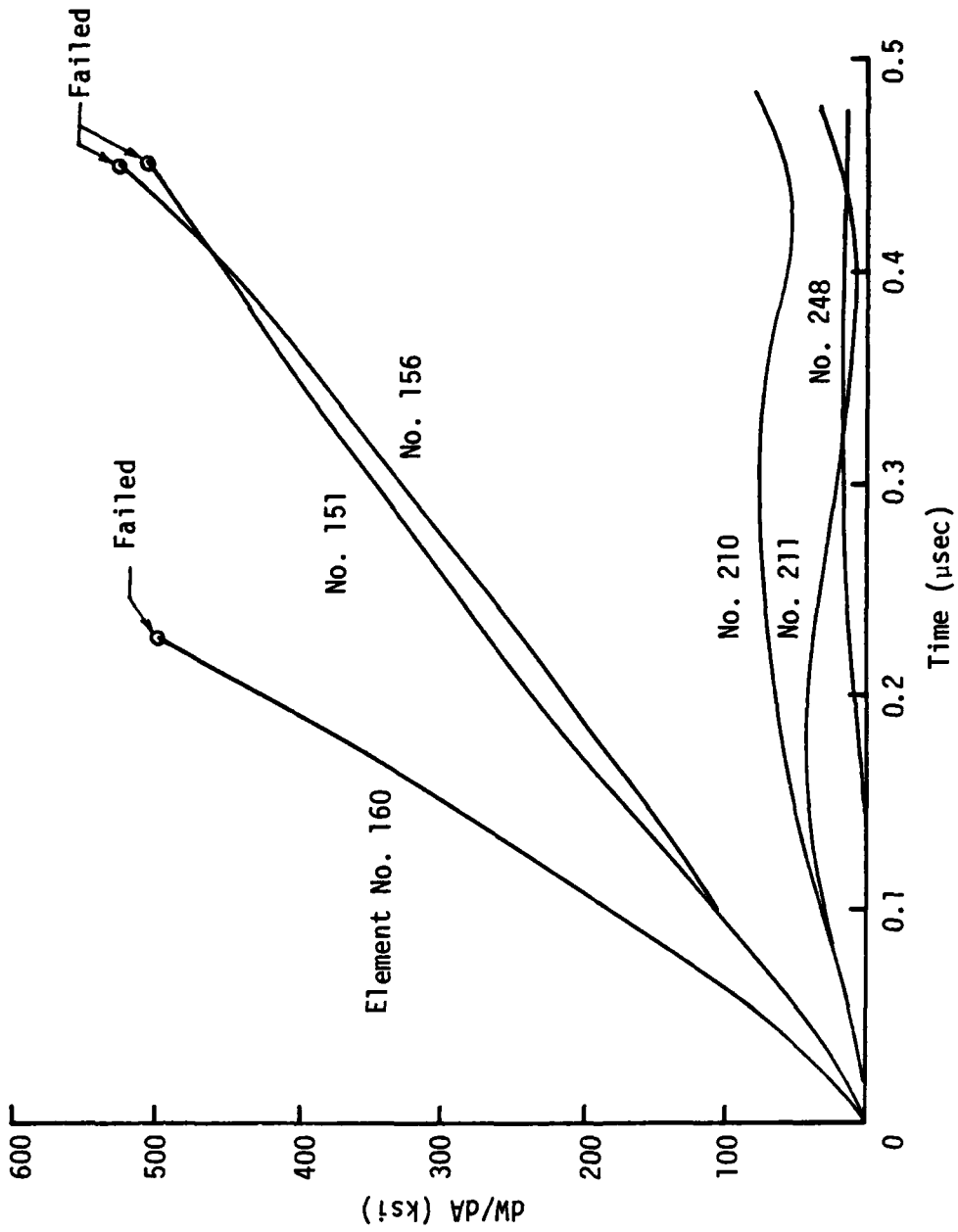


Figure 76. Variations of strain energy density per unit area with time for elements in Model II.

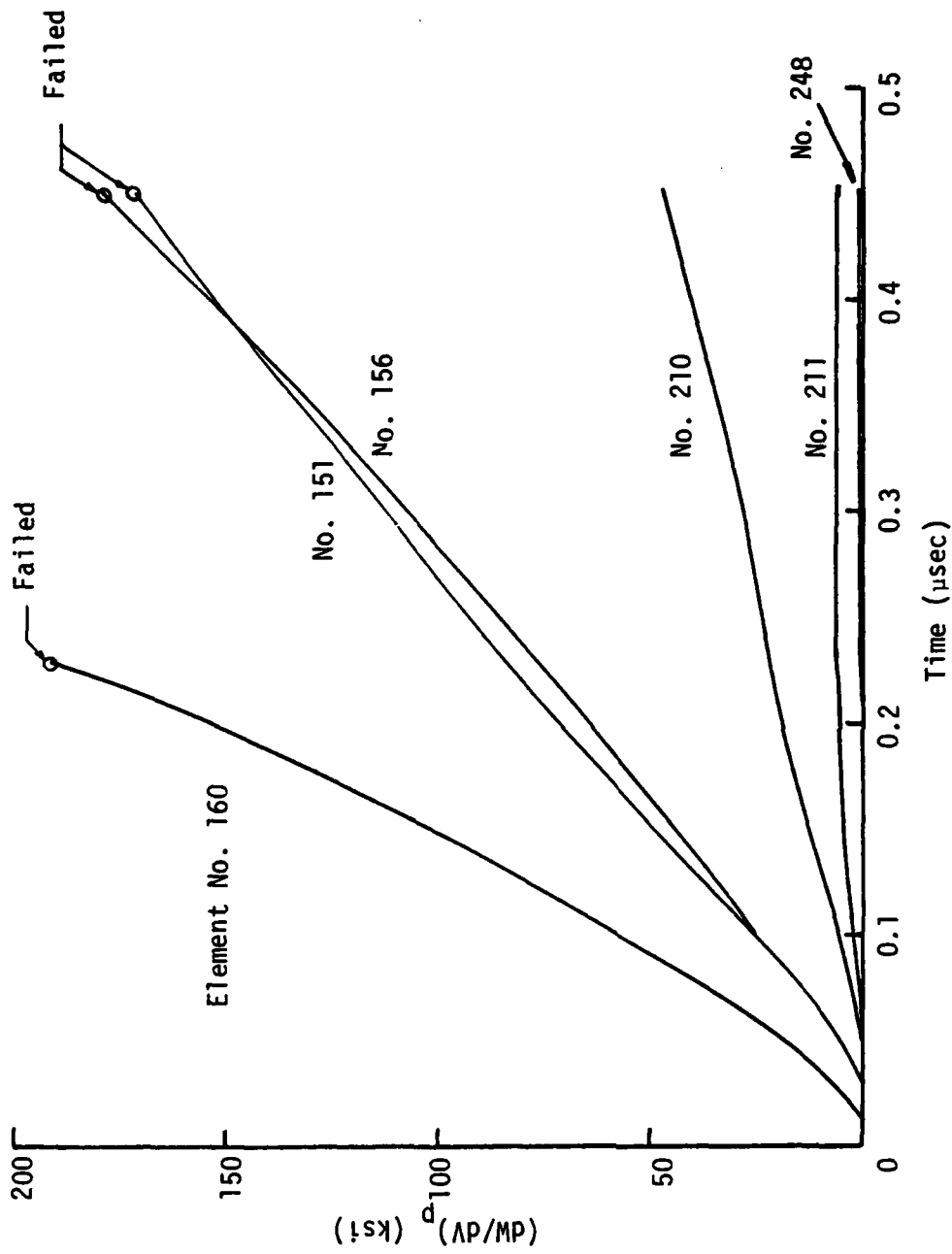


Figure 77. Variations of dissipated energy density per unit volume with time for elements in Model II.

ways rise monotonically. This is shown in Figure 77 where the slope of the curves gives an indication of the severity of damage. Element No. 160 has the largest slope in the  $(dW/dV)_p$  versus time plot and fails first. These curves yield information on the rate at which energy is dissipated as a function of time.

## REMARKS ON REFINEMENT OF ADED CODE

As mentioned throughout this report, this work on the development of ADED is considered to be preliminary. The emphases have been placed on applying the basic concept of the strain energy density theory [4] for predicting projectile penetration damage from uniaxial data alone. This required a change in one of the fundamental approaches of continuum mechanics; that is, the constitutive relations for the material elements will no longer be assumed as known but will be derived for each element and time step. Such a feature is necessary for describing the nonhomogeneous rates of deformation in penetration mechanics. Although there remains a number of refinements that should be incorporated into ADED, they are, however manageable and not regarded as overwhelming. A description of these refinements will be given.

The most serious drawbacks in many of the presently developed computer codes on penetration mechanics are inherent in the use of the classical theory of plasticity together with arbitrarily assumed failure criteria that can lead to inconsistencies and contradictions. Compatibility between failure and/or damage criterion and stress analysis is necessary for making reliable predictions. This has been accomplished through equations (3), (42) and (44) by assuming that the energy dissipated per unit area in a given time interval can be uniquely identified with the state of material damage. The predicted results on plugging for Model I and II are obviously idealized because of the simplifying assumptions which can be overcome without difficulties.

*Energy Dissipation Rates.* The ADED Code can easily accommodate higher rates of energy dissipation that can no longer be adequately described by the area under

the uniaxial stress and strain curves via  $dW/dV$ . Information on pressure  $P$  versus volume  $V$  can be used instead. A more suitable quantity is the internal energy density, say  $U$ . The Mie-Grüneisen equation of state is a case in point:

$$P = (a_1\mu + a_2\mu^2 + a_3\mu^3)\left(1 - \frac{\Gamma\mu}{2}\right) + \Gamma U(1+\mu) \quad (47)$$

in which  $\mu = V_0/V - 1$ ,  $a_i$  ( $i = 1,2,3$ ) are material-dependent coefficients and  $\Gamma$  is the Grüneisen coefficient.

Predictions on the appearance of shear band [10] during plugging can also be made by generalizing equation (3) into the form

$$\left(\frac{\partial U}{\partial A}\right)_T = \left(\frac{\partial V}{\partial A}\right)_T \left(\frac{\partial U}{\partial V}\right)_T \quad (48)$$

at a given temperature. A much more refined finite element mesh is needed for this purpose. Equation (48) can be uniquely identified with the energy dissipation rates at which phase transformation of the metal takes place.

*Finite Element Size.* The size of the finite elements in the prospective region of failure and/or damage can be refined so that more realistic shape of the plug can be predicted. This can be easily done in future calculations.

*Fragmentations.* Those elements that have failed as a result of impact between the projectile and target can remain as individual particles in the subsequent calculations. The sliding surface technique can be applied such that each of the fragments can transmit momentum and energy while displacement and stress continuity will no longer be required. In this way, they continue to contribute in the damage process.

*Fracture Initiation.* As internal elements are fractured, voids or small cracks are created causing local stress or energy intensification. This can be handled automatically by using the isoparametric nodes. The mid-nodes in a triangular element may be shifted to one-quarter of the distance from the point where the  $1/r$  character is desired in the strain energy density field where  $r$  is a radial distance. This simulates the character of an internal flaw regardless of the material behavior\*. This invariant character of the strain energy density function makes the failure analysis consistent through the loading history.

*Nonhomogeneous Damping.* The predicted projectile velocities are unrealistically high for both Model I and II. This is because no artificial viscosity has been introduced that prevails in all other computer codes. It is felt that such a factor will not be constant and should not be incorporated arbitrarily. It can vary from location to location for each time step depending on the rate of energy dissipation which is highly *nonhomogeneous*. The quantity  $(dW/dV)_p$  in equation (42) can be calculated to define an effective damping force  $F_p$  that depends on the space variables and time. This effect when included into ADED will lower the projectile velocity in a cumulative fashion.

*Time Increment or Step.* The selection of time increment or step in the numerical computation is essential and is intimately associated with the element size and location. These variables must be compatible with the rates at which energy is being nonuniformly dissipated while the material is damaged and/or failed. The fluctuation of the strain energy density function yields information on how the time and space variables should be scaled.

---

\*The singular character of the stress depends on the constitutive relations and would not be a suitable choice in this approach where the stress behavior changes from element to element for every time step.

*Three-Dimensions.* It is obvious that the  $(dW/dA)_i$  concept expressed by equation (3) can be easily extended to problems of oblique impact where no symmetry prevails. The determination of the damage plane for an homogeneous and isotropic material would then involve equating  $(dV/dA)_\xi$ ,  $(dV/dA)_\eta$  and  $(dV/dA)_\zeta$  in the three orthogonal directions  $\xi$ ,  $\eta$  and  $\zeta$ . The finite element grid pattern would be considerably more complicated but the basic procedure remains unchanged.

Many of the aforementioned refinements are already being incorporated into ADED [16]. In principle, the method applies equally well for describing the irreversible behavior of material in the solid, liquid or gaseous state. It is the versatility and generality of the strain energy density concept that makes the theory attractable.

## REFERENCES

- [1] L. J. Hageman and J. M. Walsh, "HELP, A Multi-Material Eulerian Program for Compressible Fluid and Elastic-Plastic Flow in Two Space Dimensions and Time", Systems, Science and Software Report 3SR-350, BRL Report BRL-CR-39 (1971).
- [2] G. R. Johnson, "Analysis of Elastic Plastic Impact Invoking Severe Distortion", J. of Appl. Mech. Vol. 98, pp. 439-444 (1976).
- [3] M. L. Wilkins, R. E. Blum, E. Cronshagen and P. Grantham, "A Method for Computer Simulation of Problems in Solid Mechanics and Gas Dynamics in Three Dimensions and Time", Lawrence Livermore Laboratory, Report UCRL-51574 Rev. 1 (1975).
- [4] G. C. Sih, "The Strain Energy Density Concept and Criterion", Special Issue in Fracture Mechanics Dedicated to G. R. Irwin, edited by A. K. Rao, J. of Indian Society of Aeronautical Engineering (in Press).
- [5] K. C. Dao and D. A. Shockey, "A Ref. Method for Measuring Shear Band Temperature", J. Appl. Phys., Vol. 50, No. 12, pp. 8244-6 (1979).
- [6] G. L. Moss, "Shear Strains, Strain Rates and Temperature Damages in Adiabatic Shear Bands", Ballistic Research Laboratory, Aberdeen Proving Ground, Maryland, ARBRL-TR-02242 (May 1980).
- [7] J. Mescall, R. Papirno and J. McLaughlin, "Stress and Deformation States Associated with Upset Tests in Metals", American Society of Testing Materials", STP808, pp. 7-27 (1983).

- [8] R. Papirno, J. Mescall and A. Hansen, "Fracture in Axial Compression Tests of Cylinders", American Society of Testing Materials", STP808, pp. 40-63 (1983).
- [9] J. Mescall and R. Papirno, "Spallation in Cylinder-Plate Impact", Experimental Mechanics, Vol. 14, pp. 257-266 (1974).
- [10] J. G. Michopoulos, G. C. Sih, S. C. Chou, and J. F. Dignam, "Energy Dissipation in Highly Compressed Cylindrical Bar Specimens", J. of Theoretical and Appl. Frac. Mech., Vol. 2, No. 2 (in Press).
- [11] Mechanics of Fracture, Introductory Chapters, Vol. I to Vol. VII, edited by G. C. Sih, Martinus Nijhoff Publishing, The Hague (1972-1982).
- [12] G. C. Sih, "Mechanics of Crack Growth: Geometrical Size Effect in Fracture", Fracture Mechanics in Engineering Application, edited by G. C. Sih and S. R. Valluri, Sijthoff and Noordhoff International Publishers, The Netherlands, pp. 3-29 (1979).
- [13] G. C. Sih, "The State of Affairs Near the Crack Tip", Modeling Problems in Crack Tip Mechanics, edited by J. T. Pintera, Martinus Nijhoff Publishers, The Hague, pp. 65-90 (1984).
- [14] G. C. Sih and D. Y. Tzou, "Nonhomogeneous Energy Dissipation Ahead of Slowly Growing Crack", Institute of Fracture and Solid Mechanics, IFSM-84-126, (November 1984).
- [15] G. R. Johnson, "EPIC-2, A Computer Program for Elastic-Plastic Impact Computations in 2 Dimensions Plus Spin", ARBRL-CR-00373 (June 1978).

[16] G. C. Sih and D. H. Song, "Manual of Axisymmetric Dynamic Energy Density Computer Program", AMMRC Technical Report No. 84 (November 1984).

DISTRIBUTION LIST

No. of Copies

Office of Deputy Under Secretary of Defense  
for Research and Engineering (ET)  
ATTN: Mr. J. Persh, Staff Specialist for Materials  
and Structures (Room 3D1089) 1  
The Pentagon  
Washington, DC 20301

Office of Deputy Chief of Research Development  
and Acquisition 1  
ATTN: DAMA-CSS  
The Pentagon  
Washington, DC 20301

Commander  
U.S. Army Materiel Command  
ATTN: AMCLD, R. Vitali, Office of Laboratory Management 1  
5001 Eisenhower Avenue  
Alexandria, VA 22333

Director  
Ballistic Missile Defense Systems Command  
ATTN: BMDSC-TEN, N. J. Hurst 1  
BMDSC-HE, J. Katechis 1  
BMDSC-HNS, R. Buckelew 1  
BMDSC-AOLIB 1  
P.O. Box 1500  
Huntsville, AL 35807

Director  
Ballistic Missile Defense Advanced Technology Center  
ATTN: ATC-X, D. Russ 1  
ATC-X, Col. K. Kawano 1  
ATC-M, D. Harmon 1  
ATC-M, J. Papadopoulos 1  
ATC-M, S. Brockway 1  
P.O. Box 1500  
Huntsville, AL 35007-3801

Director  
Defense Nuclear Agency  
ATTN: SPAS, Major D. K. Apo 1  
Washington, DC 20305

Director  
Army Ballistic Research Laboratories  
ATTN: DRDAR-BLT, Dr. N. J. Huffington, Jr. 1  
DRDAR-BLT, Dr. T. W. Wright 1  
DRDAR-BLT, Dr. G. L. Moss 1  
Aberdeen Proving Ground, MD 21005

No. of Copies

Commander  
Harry Diamond Laboratories  
ATTN: DRXDO-NP, Dr. F. Wimenitz  
2800 Powder Mill Road  
Adelphi, MD 20783

1

Commander  
Air Force Materials Laboratory  
Air Force Systems Command  
ATTN: LNC/Dr. D. Schmidt  
Wright Patterson Air Force Base  
Dayton, OH 45433

1

Commander  
BMO/ABRES Office  
ATTN: BMO/MNRT, Col. R. Smith  
Norton Air Force Base, CA 92409

1

Commander  
Air Force Materials Laboratory  
ATTN: AFML/MBM, Dr. S. W. Tsai  
Wright-Patterson Air Force Base  
Dayton, OH 45433

1

Commander  
Naval Ordnance Systems Command  
ATTN: ORD-03331, Mr. M. Kinna  
Washington, DC 20360

1

Naval Postgraduate School  
ATTN: Code NC4(67WT),  
Professor E. M. Wu  
Monterey, CA 93943

1

Commander  
Naval Surface Weapons Center  
ATTN: C. Lyons  
C. Rowe  
Silver Springs, MD 20910

1

1

Lawrence Livermore Laboratory  
ATTN:  
P.O. Box 808 (L-342)  
Livermore, CA 94550

1

Sandia Laboratories  
ATTN: Dr. L. D. Bertholf  
Dr. J. Lipkin  
P.O. Box 5800  
Albuquerque, NM 87115

1

1

No. of Copies

Aerospace Corporation  
ATTN: Dr. R. Cooper  
P.O. Box 92957  
Los Angeles, CA 90009

1

AVCO Corporation  
Government Products Group  
ATTN: Dr. W. Reinecke  
P. Rolincik  
201 Lowell Street  
Wilmington, MA 01997

1  
1

ETA Corporation  
ATTN: D. L. Mykkanen  
P.O. Box 6625  
Orange, CA 92667

1

Fiber Materials, Inc.  
ATTN: M. Subilia, Jr.  
L. Landers  
R. Burns

1  
1  
1

Biddeford Industrial Park  
Biddeford, ME 04005

General Electric Company  
Advanced Materials Development Laboratory  
ATTN: K. Hall  
J. Brazel  
3198 Chestnut Street  
Philadelphia, PA 19101

1  
1

General Dynamics Corporation  
Convair Division  
ATTN: J. Hertz  
5001 Kearny Villa Road  
San Diego, CA 92138

1

General Research Corporation  
ATTN: Dr. R. Wengler  
Dr. R. Parisse  
J. Green  
5383 Hollister Avenue  
Santa Barbara, CA 93111

1  
1  
1

Kaman Sciences Corporation  
ATTN: Dr. D. Williams  
P.O. Box 7463  
Colorado Springs, CO 80933

1

No. of Copies

Ktech  
ATTN: Dr. D. Keller 1  
911 Pennsylvania Avenue, N.E.  
Albuquerque, NM 87110

Lehigh University  
Institute of Fracture and Solid Mechanics  
ATTN: Dr. George C. Sih 1  
Bldg. 39, Packard Lab  
Bethlehem, PA 18015

Los Alamos National Laboratory  
ATTN: Henry L. Horak 1  
Mail Stop C936  
Los Alamos, NM 87545

Martin Marietta Aerospace  
ATTN: V. Hewitt 1  
Frank H. Koo 1  
P.O. Box 5837  
Orlando, FL 32805

Pacifica Technology, Inc.  
ATTN: Dr. Ponsford 1  
P.O. Box 148  
Del Mar, CA 92014

Radkowski Associates  
ATTN: Dr. P. Radkowski 1  
P.O. Box 5474  
Riverside, CA 92507

Southwest Research Institute  
ATTN: A. Wenzel 1  
8500 Culebra Road  
San Antonio, TX 78206

Terra Tek, Inc.  
ATTN: Dr. A. H. Jones 1  
420 Wakara Way  
Salt Lake City, UT 84108

Defense Documentation Center  
Cameron Station, Bldg. 5  
5010 Duke Station  
Alexandria, VA 22314 1

No. of Copies

Director  
Army Materials and Mechanics Research Center  
ATTN: AMXMR-B, J. F. Dignam  
          AMXMR-B, Dr. S. C. Chou  
          AMXMR-B, L. R. Aronin  
          AMXMR-B, Dr. D. P. Dandekar  
          AMXMR-K  
          AMXMR-PL  
Watertown, MA 02172

1  
5  
1  
1  
1  
2



**END**

**FILMED**

*2-86*

**DTIC**